Master Thesis

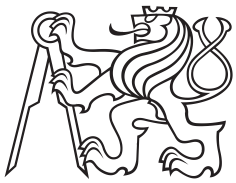

Czech Technical University in Prague

F4

Faculty of Nuclear Sciences and Physical Engineering
Department of Physics

Characterisation of heat fluxes in edge plasma of the COMPASS tokamak in H-mode discharges

Charakterizace tepelných toků v okrajovém plazmatu tokamaku COMPASS v plazmatech s módem vysokého udržení

Bc. Jan Hečko

Supervisor: Mgr. Michael Komm, Ph.D.
Supervisor–specialist: Ing. Miroslav Šos
Field of study: Physics and Thermonuclear Fusion Technology
July 2021

ČESKÉ VYSOKÉ UČENÍ TECHNICKÉ V PRAZE
FAKULTA JADERNÁ A FYZIKÁLNĚ INŽENÝRSKÁ
PRAHA 1 - STARÉ MĚSTO, BŘEHOVÁ 7 - PSČ 115 19

Katedra: fyziky *Akademický rok:* 2020/2021

ZADÁNÍ DIPLOMOVÉ PRÁCE

Student: Bc. Jan Hečko

Studijní program: Aplikace přírodních věd

Obor: Fyzika a technika termojaderné fúze

Název práce: (česky) Charakterizace tepelných toků v okrajovém plazmatu tokamaku COMPASS v plazmatech s módem vysokého udržení

Název práce: (anglicky) Characterisation of heat fluxes in edge plasma of the COMPASS tokamak in H-mode discharges

Pokyny pro vypracování:

1. V rámci existujících dat na tokamaku COMPASS vyhledat sadu výbojů s módem vysokého udržení, které jsou vhodné pro analýzu tepelných toků.
2. Provést fitování exponenciálních profilů hustoty a teploty měřených diagnostikou Thomsonova rozptylu v okrajovém plazmatu. Pokud to bude potřeba, provést korekci těchto profilů na tzv. stray-light.
3. Provést fitování profilů tepelných toků na divertoru měřených pomocí kombinovaného pole divertorových sond, popřípadně IR kamerou.
4. Porovnat tato měření mezi sebou a s existujícími modely pro škálování útlumové délky tepelného toku.
5. U vybraných výbojů provést kontrolu tzv. power balance, tedy výkonu dodaného do plazmatu versus výkonu deponovaného na stěny tokamaku a výkonu záření.

Doporučená literatura:

[1] Wesson, J.: Tokamaks, Oxford University Press, New York, USA, 2011.

[2] T. Eich: Scaling of the tokamak near the scrape-off layer H-mode power width and implications for ITER. Nuclear Fusion, 2013, 53.9: 093031.

[3] Silva, C.G.: Divertor physics studies on COMPASS-D. PhD thesis, UTL, 2000.

[4] Silvagni D. et al.: Scrape-off layer (SOL) power width scaling and correlation between SOL and pedestal gradients across L, I and H-mode plasmas at ASDEX Upgrade. Plasma Physics and Controlled Fusion, 2020, 62.4: 045015.

[5] Adamek, J. et al.: Electron temperature and heat load measurements in the COMPASS divertor using the new system of probes, Nuclear Fusion, 2017, 57.11: 116017.

Jméno a pracoviště vedoucího diplomové práce:

Mgr. Michael Komm, Ph.D., Ústav fyziky plazmatu AV ČR, v.v.i.

Jméno a pracoviště konzultanta:

Ing. Miroslav Šos, Ústav fyziky plazmatu AV ČR, v.v.i.

Datum zadání diplomové práce: 23.10.2020

Termín odevzdání diplomové práce: 03.05.2021

Doba platnosti zadání je dva roky od data zadání.

……
garant oboru

…….. ……..
vedoucí katedry *děkan*

V Praze dne 23.10.2020

Acknowledgements

I would like to extend my thanks to my supervisor Mgr. Michael Komm, Ph.D. for all his patience, helpful suggestions and frequent motivation despite the remote situation. I am glad that he was able to introduce me to the interesting topic of the SOL plasma in tokamak and its intricacies. Next, I would like to thank the COMPASS TS team, who supplied me with all the knowledge about the Thomson scattering diagnostics and the H-mode plasma, and especially to Ing. Miroslav Šos, whose notes about the thesis were always on point.

Last but not least, I would like to thank my whole family and friends for all the support during those long days of typing words into the computer.

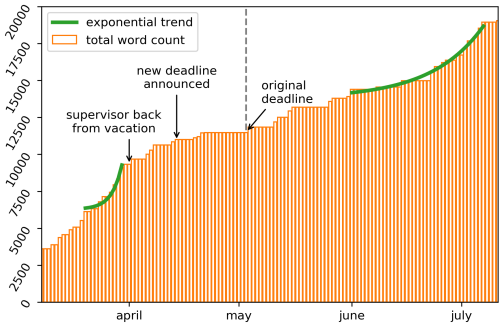

Fig.: Evolution of the thesis word count in time, March-July 2021.

Prohlášení

Prohlašuji, že jsem svou diplomovou práci vypracoval samostatně, a použil jsem pouze podklady uvedené v přiloženém seznamu.

Nemám závažný důvod proti použití tohoto školního díla ve smyslu § 60 Zákona č. 121/2000 Sb., o právu autorském, o právech souvisejících s právem autorským a o změně některých zákonů (autorský zákon).

V Praze dne .....

.....
Bc. Jan Hečko

Abstract

The research of heat fluxes in the scrape-off layer (SOL) plasma is important for prediction of material requirements for future tokamaks, including the ITER tokamak. The focus of this research is the dependence of the heat flux profile width, the decay length, on plasma and machine parameters. In the recent years, a significant disagreement between empirical scaling and results of gyrokinetic simulations was observed. The aim of this thesis was to characterize the heat fluxes in the ELMy H-mode discharges in the COMPASS tokamak and analyze the power balance. A database of 111 inter-ELM edge plasma profiles was collected and two methods were used to measure the decay length, utilizing both the Thomson scattering diagnostics in the upstream SOL and the divertor probe array in the downstream SOL. An anomaly of short decay lengths was observed in support of the recent findings from the TCV tokamak.

Keywords: power decay length, H-mode, divertor, tokamak

Supervisor:
Mgr. Michael Komm, Ph.D.
Ústav fyziky plazmatu AV ČR, v.v.i.

Abstrakt

Výzkum tepelných toků v okrajovém plazmatu je důležitý pro předpověď materiálové zátěže v budoucích fúzních zařízeních včetně tokamaku ITER. Profil tepelného toku je možné charakterizovat tzv. útlumovou délkou, jejíž závislost na parametrech plazmatu a zařízení je hlavním bodem zmíněného výzkumu. V nedávné době bylo vyvinuto několik empirických modelů zmíněné závislosti, jejichž předpovědi jsou však v rozporu s výsledky gyrokinetických simulací. Cílem této práce bylo charakterizovat tepelné toky v ELMy H-mód výbojích na tokamaku COMPASS a také zkoumat výkonovou rovnováhu. Byla sestavena databáze 111 profilů okrajového plazmatu a byly použity 2 metody měření útlumové délky za pomoci Thomsonova rozptylu a pole divertorových sond. Následně byla pozorována anomálie ve velikosti změřených délek, které byly výrazně kratší něž předpovědi modelů. Podobná anomálie byla už pozorována i dříve na tokamaku TCV.

Klíčová slova: útlumová délka, tepelný tok, H-mód, divertor, tokamak

Překlad názvu: Charakterizace tepelných toků v okrajovém plazmatu tokamaku COMPASS v plazmatech s módem vysokého udržení

Contents

Introduction

Thermonuclear fusion is the powerhouse of stars. In a world with ever increasing demand for sustainable sources of energy, the fusion power represents a unique opportunity. The fusion research is an international effort, which aims to harness the excess energy released during fusion reactions and use it here on Earth to supply electricity. In order to create a star on Earth it is vital to first solve the question of confining high-temperature plasma of more than 10 millions °C inside the reactor for a prolonged periods of time, during which the plasma particles are able to collide with high-enough momentum to trigger a fusion reaction. The two most promising methods of plasma confinement is the magnetic confinement fusion (MCF) and inertial confinement fusion (ICF). The former approach, MCF, is the focus of this thesis and it uses strong magnetic fields to control the trajectories of charged plasma particles so that they cannot escape.

Tokamak is a type of a fusion device, which utilizes the MCF approach. As shown in Fig. 1, the main feature of the tokamak is the toroidal vacuum vessel, which contains the plasma, and around it there are several sets of magnetic field coils, which generate strong helical magnetic field (a superposition of toroidal and poloidal field) inside the vessel. In order to reach the temperatures necessary for fusion reactions, the plasma is heated up by induction heating and other auxiliary heating elements. The largest contemporary tokamak is the Joint European Torus (JET), which is to be succeeded by the fruit of the international collaboration, the ITER tokamak, in following years. There are many other tokamaks scattered around the globe including two machines in the Czech Republic: the educational GOLEM tokamak and the COMPASS tokamak.

The COMPASS tokamak is a medium-sized fusion device with major radius $R_0 = 0.56\,\mathrm{m}$ and minor radius $a = 0.23\,\mathrm{m}$ [2]. Its toroidal coils generate a toroidal magnetic field of up to $B_\phi = 1.6\,\mathrm{T}$ and the central solenoid is able to induce a plasma current of $I_\mathrm{p} = 300\,\mathrm{kA}$. A typical length of one discharge is around 300 ms. Auxiliary heating is provided by two 400 kW neutral beam injectors that inject 40 keV neutral particles into the plasma. It can operate in both the limiter and the divertor configuration, the latter enabling it to achieve the high confinement mode (H-mode), which offers better plasma parameters than the 'default' low confinement mode (L-mode). Refer to chapter 1 for

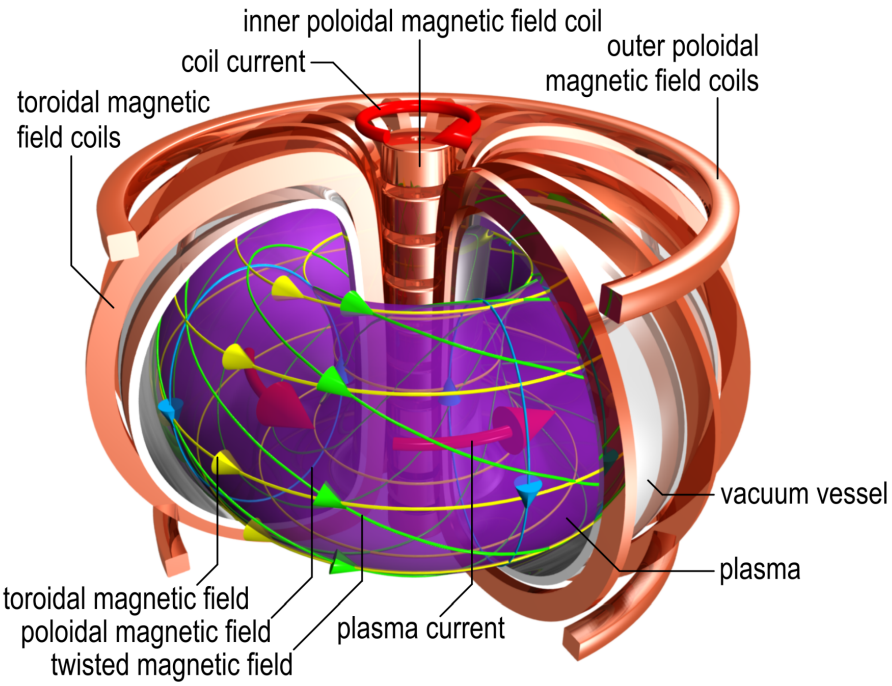

Fig. 1: Illustration of a tokamak fusion device. Its main components are the toroidal vacuum vessel and the magnetic field coils. Inside the vessel (light gray) is the plasma (purple) confined by the helical magnetic field (green), which is generated primarily by the toroidal coils, the outer poloidal coils and the plasma current (red), which is in turn induced by the inner poloidal coils. [1]

more details about field configurations and confinement modes. The research in the COMPASS tokamak is focused on the edge plasma physics, plasma-wall interaction, L- to H-mode transition and runaway electrons. In the near future it is to be succeeded by the COMPASS-Upgrade tokamak, which is designed to have high toroidal field $B_\phi = 5\,\mathrm{T}$, plasma current $I_\mathrm{p} = 2\,\mathrm{MA}$ and high temperature ($\leq 500\,^\circ\mathrm{C}$) of the vacuum vessel during operation [3].

Several decades of the tokamak research indicate that the plasma confinement can be optimized by increasing the machine size and the magnetic field. That is why the next step towards a fusion power plant is the ITER tokamak, which exceeds the design parameters of any previous tokamak. However, there is a number of caveats that need to be solved yet. One of these caveats is the heat flux carried by particles q, which together with radiation constitutes the majority of all power output from the plasma and which is a result of imperfections in plasma confinement. The parallel transport directs the escaped particles towards the first wall, more specifically to the divertor targets, where the energy is absorbed through the plasma-material interaction. If the profile of q is very narrow, it can cause fast deterioration of the material components and permanent damage.

The width of the q profile is characterized by the power decay length λ_q. Curiously, there is a significant disagreement between λ_q predictions for ITER using the gyrokinetic simulations [4] and the empirical scaling models [5],

which predict 10× more narrow profiles perhaps beyond our current material capabilities. The main topic of this thesis is the analysis of empirical λ_q models for H-mode plasma in the COMPASS tokamak, which represents the opposite extreme of the machine size spectrum offering additional insight into the accuracy of the models.

The first chapter of this thesis introduces the magnetic field configurations of the tokamak, the operational regimes and the physics of the scrape-off layer (SOL). The chapter also describes the theory of the power balance in the tokamak. Next, the methods of power decay length λ_q research are presented in the chapter 2 together with a list of recently published empirical scaling models for H-mode plasma. The chapter 3 focuses on the edge plasma diagnostics in the COMPASS tokamak that were used in this thesis, namely the Thomson scattering and the divertor array of electrostatic probes. The chapter 4 describes the process of forming the inter-ELM λ_q database on the COMPASS tokamak from both upstream and downstream data and the results are presented in the chapter 5. Apart from the power decay length measurements, the chapter also includes the results of the analysis of power balance in several selected discharges. Finally, the uncertainty and interpretation of the results is discussed in the chapter 6.

Chapter 1

Physics of the scrape-off layer (SOL) and divertor plasma

This chapter aims to provide a theoretical insight into the topic of peripheral plasma regions in tokamak, namely the scrape-off layer. A definition of common terms related to the description of plasma regions is presented. The two common configurations of plasma confinement, the limiter and the divertor, are introduced and compared. The simple SOL model is derived and its deficiencies are discussed followed by an introduction to the complex SOL model. Last section of this chapter is dedicated to the divertor heat flux in the context of the power balance in tokamak.

1.1 Plasma in tokamak

An important concept in the design of tokamak devices is the toroidal symmetry, which in turn applies to the confined plasma. Therefore, when describing plasma in tokamak it is often sufficient to simplify the problem to a 2d visualization in poloidal plane. An example of this type of visualization can be seen in Fig. 1.1 and Fig. 1.2.

The colored lines in Fig. 1.2a and Fig. 1.2b represent poloidal projection of surfaces with constant magnetic flux, further referred to as flux surfaces. The direction of magnetic field, which determines the ideal trajectory of an isolated charged particle, is always tangential to a flux surface. In tokamak plasma, the trajectories of charged particles are affected by drifts and collisions, enabling transport in the cross-field direction (i.e. perpendicular to the flux surface). However, the design of a tokamak device ensures that the magnitude of cross-field transport of particles is very limited in comparison to the parallel transport.

As seen in Fig. 1.2a, flux surface can either close itself inside the tokamak vessel, effectively confining the enclosed particles, or it can intersect inner wall and in-vessel components. By convention, it is then referred to as the *closed* and the *open* surface, respectively. The boundary between closed and open surfaces, orange line in Fig. 1.2a, is the last closed flux surface (LCFS) and it separates two plasma regions with distinct properties. The region beyond LCFS, also known as the *scrape-off layer* (SOL), is the main focus of

this thesis. The inner region of confined plasma is referred to as the *main plasma*, see Fig. 1.1a for a simplified schematics. Further discussion of the SOL region requires introducing the two main configurations of magnetic confinement in tokamak, the limiter (Fig. 1.1a) and the divertor (Fig. 1.1b) configuration. [6, 7]

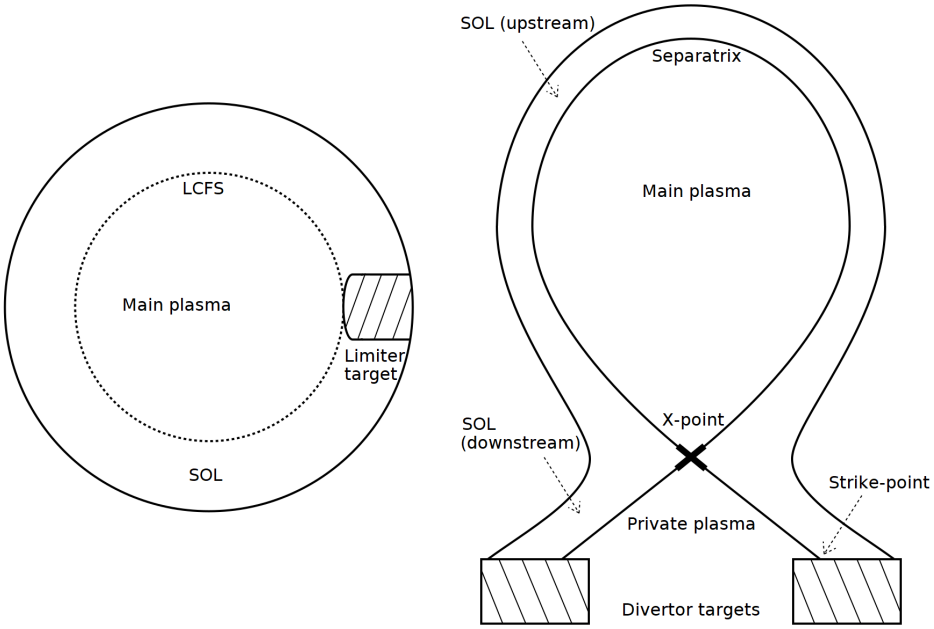

(a) : Limiter configuration. **(b) :** Divertor configuration.

Fig. 1.1: Schematics of limiter and divertor configurations.

1.1.1 Limiter configuration

Main goal of both divertor and limiter configuration is to limit the contact of plasma with the wall and prevent material erosion. Limiter configuration introduces a specialized durable in-vessel component, the limiter, which acts as a sink for charged plasma particles that would otherwise diffuse toward the wall. As depicted in Fig. 1.2a and Fig. 1.1a, the radial dimension of the limiter determines the thickness of the SOL, the bulk of the plasma leans on the limiter and comes into close contact with it. The limiter in the figure is a toroidal limiter, it extends along the walls creating a ring-like shape and therefore conforming with the toroidal symmetry of tokamaks. Similarly, a poloidally symmetrical limiter is also recognized, however, it is less common.

The limiter configuration is simple and uses only a single passive component. However, this advantage is usually outweighed by the negative effects of its close proximity to the main plasma. While the wall is shielded from direct contact with it, plasma still interacts with the material of limiter producing impurities (free atoms, usually with higher Z than the hydrogen fuel). The impurities diffuse into the hot main plasma causing an increase in energy losses

through radiated power. Nevertheless, the limiter approach was historically successful in the context of experiments with moderate plasma temperatures and heating, where the effects of plasma-material interaction are limited. Nowadays, tokamak devices designed purely for the limiter configuration are rare in favor of the divertor configuration.

1.1.2 Divertor configuration

The divertor configuration uses a dedicated poloidal field coil to alter the magnetic field and convey the SOL plasma away from the main plasma and direct it at a divertor target as depicted in Fig. 1.2b and Fig. 1.1b. This effectively slows the diffusion of produced impurities into the main plasma by increasing the distance. Note that in Fig. 1.1b the main boundary is labeled as the *separatrix*, instead of LCFS, because the boundary is no longer a closed surface. A distinct feature of the separatrix is the X-point, where the surface intersects itself and the poloidal magnetic field is zero. An identical feature can be found in a simple configuration of magnetic field generated by two long parallel wires, when the current in both wires flows in the same direction, demonstrating the similarity between these two configurations. In the tokamak the pair of wires is substituted by the divertor coil and the plasma itself.

In the context of advantages of the divertor approach, it has been already mentioned that it is able to shield the vessel wall from interaction with plasma particles, while mitigating the problems with impurities, which are inherent to the limiter configuration. It is also known to provide higher chance of creating the edge transport barrier and reaching the High confinement mode (H-mode), see section 1.1.3. In addition to that, the divertor targets can be coupled with pumping systems to provide an effective method of removing reaction products (helium) from plasma in future reactors. Most of present tokamak experiments use primarily the divertor configuration and it is the focus of this thesis. As a side note, Fig. 1.2b describes the common poloidal-field divertor configuration with a single target positioned below plasma. This is often referred to as the *lower single null* configuration.[1] There are experiments which study the effects of upper single null or double null configurations [9], [10], [11]. A theoretical alternative to the conventional poloidal-field divertor would be the toroidal-field divertor, but, similarly to the poloidal limiter, it is not commonly implemented.

Field configuration depicted in Fig. 1.2b defines two plasma regions that are unique to the divertor configuration. The first one is the *divertor region* located near the divertor targets, which has a high density of neutral particles and a high radiation density. The other one is *private flux region*, it is located beneath the X-point and it exists strictly as a result of cross-field transport of particles from SOL. Its properties are similar to those of the divertor region.

[1] Single null refers to the fact that there is a single X-point, i.e. point where there is zero poloidal magnetic field. Lower single null then specifies that the X-point is located in the lower part of the tokamak vessel.

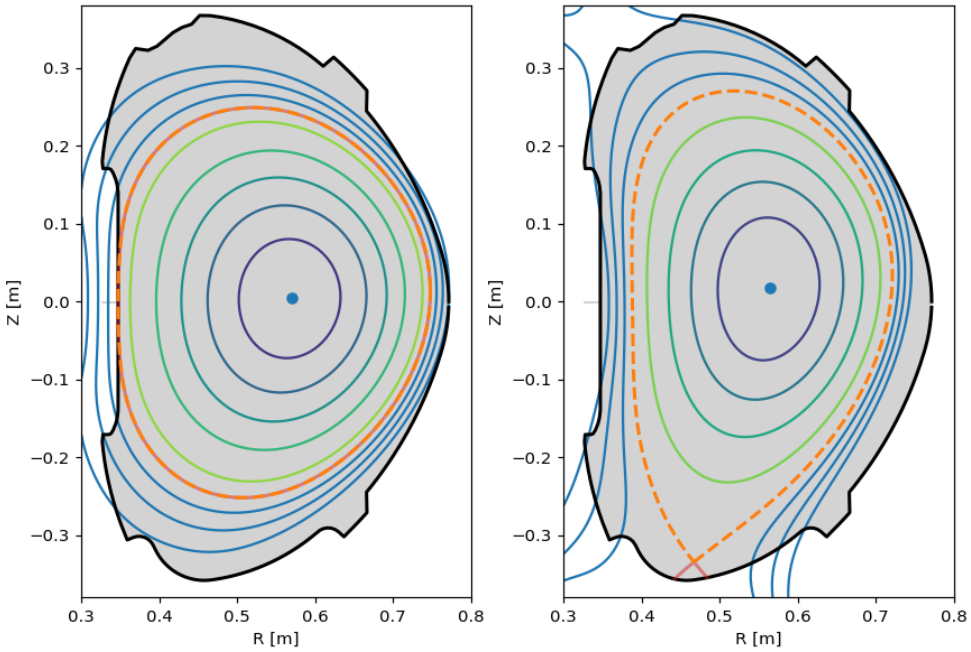

(a) : Limiter configuration. The limiter component is located on the inner vessel wall (on the left). Dashed orange line represents the LCFS, which separates the main plasma and the SOL region. Field lines outside of LCFS are referred to as open lines in the context of the vessel, because they intersect its surface.

(b) : Divertor configuration. Dashed orange line represents the separatrix, which intersects itself above the divertor target, which is located on the bottom of the vessel, creating the X-point. On the COMPASS tokamak the X-point is very close to the targets, which results in atypically small size of the divertor plasma regions.

Fig. 1.2: Comparison of the (toroidal) limiter configuration and the (poloidal) divertor configuration using data from EFIT reconstruction of two discharges on the COMPASS tokamak. The view shows magnetic field lines in poloidal cross-section of a tokamak chamber on the right side from the toroidal axis. Plotted with the use of [8].

Upstream from both of these regions remains the SOL, which is, unlike them, in close contact with the main plasma and therefore its properties differ from the downstream regions.

1.1.3 High confinement mode

The High confinement mode (H-mode), discovered in 1982 in the ASDEX tokamak [12], is an important step forward in the field of tokamak fusion research. Before its discovery, all tokamak devices operated in what is today known as the Low confinement mode (L-mode). The experiments showed that the confinement time of L-mode plasma is negatively affected by the use of auxiliary high-power heating, which is, however, a necessary factor in order to maintain fusion temperatures and produce fusion energy in tokamak. The H-mode mitigates the negative effects and as a result, it offers two- or three-fold longer confinement time than L-mode with the same levels of heating power. [13]

While the L-mode could be presented as the 'default' regime of operation, the H-mode is achieved via a transition from L-mode, which is referred to as the L-H transition. The transition itself is triggered by a set of conditions, which are mostly related to the properties of the edge plasma. According to the current research, the main threshold includes the minimal temperature of the edge plasma and the minimal average density of plasma. Then, under these conditions the *edge transport barrier* is formed and the cross-field transport is significantly reduced. [13]

Reaching the temperature threshold requires sufficient heating power. Thus, a more practical threshold of heating power is often recognized instead. To increase the heating power, additional non-ohmic heating techniques are used, including the neutral beam injector (NBI) or heating by electromagnetic waves (ECRH, ICRH). However, if the edge plasma contains high concentration of neutrals or impurities (e.g. because of wall material erosion), an increase in temperature is followed by an increase in power losses through radiation of the neutrals and impurities and the overall heating efficiency rapidly decreases. Therefore the radiation losses need to be controlled as well. In this context, the use of divertor configuration offers a significant advantage over the limiter configuration, because it limits the diffusion of neutrals into plasma, see section 1.1.2.

A common H-mode characteristic is the significant decrease of cross-field transport and therefore also a decrease of the flow of particles that escape the confinement through the separatrix. This phenomenon appears to be caused by a barrier of some kind, the edge transport barrier. The idea of the edge transport barrier provides the basis for most of the today's attempts at explaining the physics of H-mode and source of its advantageous properties. A popular theory states that a shear flux of particles in the edge plasma region helps to dissolve turbulent structures that would have otherwise contributed to the cross-field diffusion. Nevertheless, both its behavior and the process of forming the barrier are subjects of active research.

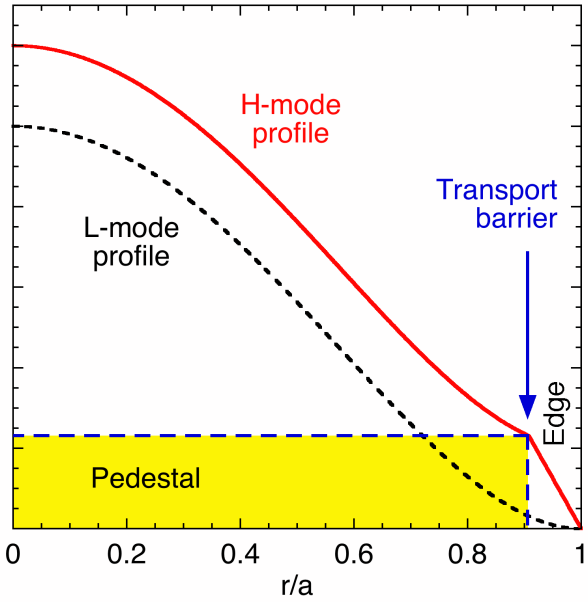

Fig. 1.3: Schematic comparison of L-mode and H-mode plasma pressure radial profiles. The H-mode profile features the characteristic *pedestal* and the steep slope in the edge region. Profiles of plasma temperature and density show similar characteristics. [15]

Another important characteristic of the H-mode plasma and a consequence of the transport barrier is the fact that the plasma pressure profile (and electron temperature and density profiles) forms a very steep downwards slope in the edge area near the separatrix as seen in Fig. 1.3. When compared to an L-mode profile, the H-mode profile behaves similarly in the core area but as a whole it appears to be lifted up on a *pedestal*. As a result of that, the magnitude of confined plasma pressure is significantly higher in the H-mode case. As a side note, the pedestal is a well recognized term in the fusion community that is often used to describe either the steep slope or the elevated shape of an H-mode profile in general. [14]

The transport barrier acts as a dam that blocks the flow of river (the cross-field flow of particles) filling up a reservoir (the pedestal). However, the water-level, or rather the pedestal slope and the plasma density, cannot rise indefinitely. Eventually, the pedestal collapses and a small portion of the plasma mass is ejected during what is called the *Edge localized mode* (ELM) instability. The cycle can be also described by the ballooning-peeling model, see Fig. 1.4. The mass ejection is accompanied by a sharp peak of D_α radiation, which serves as a reliable method of detecting the ELM instability on devices with carbon first wall, including the COMPASS tokamak. Example of the D_α signal is presented later in chapter 4, Fig. 4.3. Devices with an all-tungsten first wall, for example the ASDEX-Upgrade, may utilize different diagnostic methods such as measuring the shunt currents. The ELMs occur quasi-periodically with frequency ranging in the order of 10 kHz in smaller devices down to 10 Hz in the larger ones and the ejected particles can carry

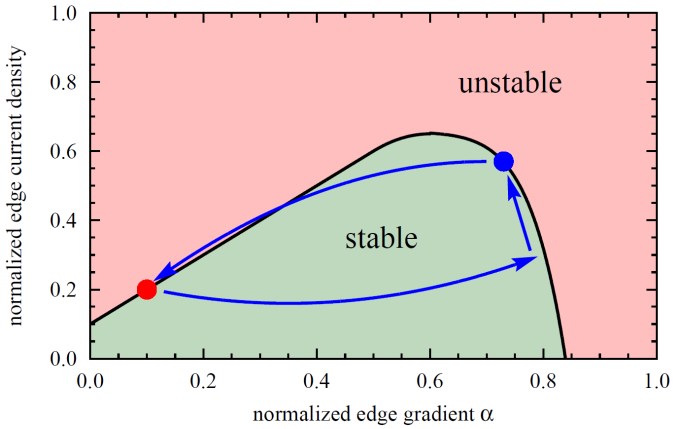

Fig. 1.4: Illustration of the peeling-ballooning model of the ELM instability. The start of the ELM cycle is marked with the red dot on the left side, where the current density and edge gradients are low. During the ballooning phase the edge gradients rise until the threshold of ballooning instability is reached (right edge of the stable region). At that point the gradients are saturated and the current density starts increasing, which triggers the peeling instability. Finally, a portion of the confined plasma is ejected relaxing both the current density and the edge gradients. [16]

1–10 % of the total plasma energy. The largest tokamak ITER is expected to operate with natural ELM frequency in the order of 1 Hz.

While high-energy ELM present a significant heat strain for the divertor targets and may even cause permanent material damage, in general, the they offer a means of continuous purification of the plasma by ejecting the impurities as well as the reaction products. The combination of ELM instability and H-mode is referred to as the ELMy H-mode and based on many years of continuing research it is considered to be the most promising operational mode for ITER. However, the search for a stable ELM-free H-mode, which would avoid the divertor heat strain of ELM instabilities, and other alternatives is a hot topic of current fusion research. [17, 18]

As described in the Fig. 1.4, near the end of the short period of time between two ELM events, the *inter-ELM* period, the plasma temperature, density and pressure gradients reach a saturated, quasi-stationary state. It is assumed that this state occurs approximately during the last third of the cycle. The plasma parameters measured during the quasi-stationary inter-ELM phase are suitable (and thus often used) for statistical research and inference of scaling laws between devices. [19, 5]

1.1.4 Further research of confinement modes

While the ELMy H-mode is recognized as the most promising confinement mode for ITER, it is not necessarily an ideal solution for all future fusion reactors. A main concern is that the target heat strain caused by the strongest (type-I) ELMs in a reactor-sized tokamak may be beyond current material capabilities of the PFCs. Thus, the research of alternative, more favorable

confinement modes is an important topic in the fusion community.

One example is the I-mode confinement regime, which was first introduced on the Alcator C-Mod[17] and further investigated in several other tokamaks including the ASDEX Upgrade[20]. I-mode combines advantages of the H-mode performance with L-mode stability and can be thought of as an intermediate stage between the two. A setup with upper single null divertor, which offers an 'unfavorable' direction of ∇B drift, is typically used in order to increase the heating power P_{H} threshold for H-mode and thus widen the P_{H} operating window for I-mode. Similarly to H-mode it features an energy transport barrier, which is observed as the temperature pedestal. However, the particle transport barrier is absent and the density profile is similar to an L-mode profile. The particles are able to flow continuously and the occurrence of strong type-I ELM events is avoided. Less energetic phenomenons, known as the pedestal relaxation events (PDE), may still appear when the plasma is close to the transition to H-mode. Current effort at ASDEX Upgrade is focused on proving compatibility of I-mode with detachment, which is a key requirement for future reactors [21].

1.2 Simple SOL model

The Simple SOL model provides a simple stationary solution for plasma transport in the SOL region. It uses several key assumptions that are closely linked to the limiter configuration. Because of that, the relevance of the solution is limited to the aforementioned configuration, while in most cases the divertor configuration requires a more complex approach, which is described in the next section 1.3.

1.2.1 Conditions of the simple SOL

According to [7], the model assumes that the neoclassical effects (e.g. banana orbits) and other kinetic effects caused by the curvature of magnetic field $\vec{B}$ can be ignored. This can be justified by the strong collisionality of the SOL plasma at low temperatures. As a result of that, the SOL and the helical curvature of $\vec{B}$ filed lines can be 'straightened out' as illustrated in Fig. 1.5 and the fluid model of plasma can be used.

There are several important terms related to the straightened-out model, which ought to be introduced. The typical parallel-to-$\vec{B}$ distance that a charged particle has to travel before striking a solid surface is referred to as the *connection length* $L_{\parallel}$. In the case of Fig. 1.5 it is equal to the half of the distance between the two bounding targets. It is assumed that a majority of the particles enter the SOL at the symmetry point, halfway between both targets. In an actual tokamak the connection length is defined as the shortest distance along the field lines from outer midplane to a target, because the majority of particles enters the SOL near the outer midplane. $L_{\parallel}$ on the LFS is shorter than $L_{\parallel}$ on the HFS as a result of a difference in the strength of the toroidal magnetic field and in the poloidal distance from outer

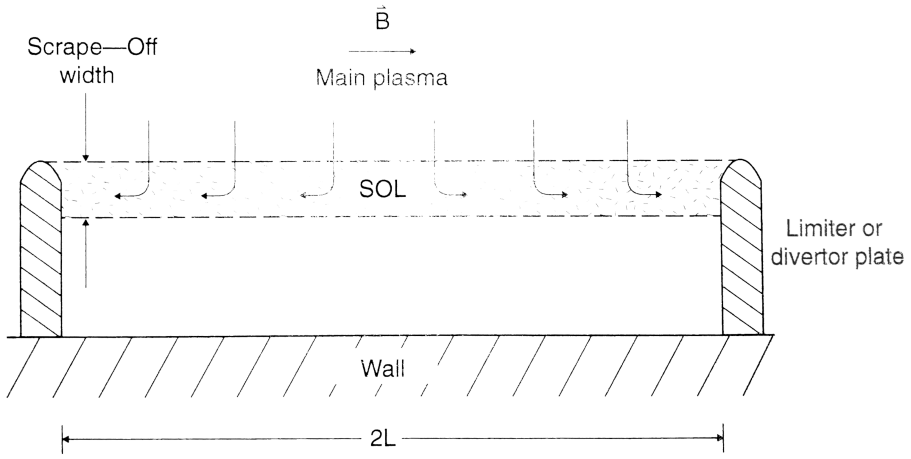

Fig. 1.5: An illustration of the 'straightened-out' SOL model, where the curvature of the particle trajectories is ignored. Particles affected by cross-field transport processes leave the main plasma across the LCFS. Once they enter the SOL region, the much faster parallel transport swiftly pulls them towards the limiter or divertor plane. Thus, the width of the SOL is affected by the ratio between the strength of cross-field and the parallel transport. [7]

midplane. In general, the $L_{\parallel}$ measures tens of meters for large tokamaks, such as JET, and decreases down to several meters for smaller tokamaks, such as COMPASS. Using the connection length it is possible to calculate an estimate of a *characteristic particle dwell time* in SOL

$$\tau_{\mathrm{sol}} \approx \frac{L_{\parallel}}{c_{\mathrm{s}}}, \tag{1.1}$$

where c_{s}

$$c_{\mathrm{s}} = \sqrt{\frac{k(T_{\mathrm{i}} + T_{\mathrm{e}})}{m_{\mathrm{i}}}} \tag{1.2}$$

is the ion acoustic speed in hydrogen plasma ($Z = 1$). T_{i} and T_{e} is the ion and electron temperature respectively. Later in this section it is discussed that the acoustic speed c_{s} is the *characteristic speed* of the plasma fluid in SOL as it reaches the sheath. The characteristic time τ_{sol} is typically quite short, in the order of 1 ms or less. Using the τ_{sol} it is possible to provide a very simple estimate of the SOL width

$$\lambda_{\mathrm{sol}} \approx \sqrt{D_{\perp}\tau_{\mathrm{sol}}} = \sqrt{D_{\perp}\frac{L_{\parallel}}{c_{\mathrm{s}}}}, \tag{1.3}$$

assuming the cross-field transport is dominated by classical or neoclassical diffusion with diffusion coefficient $D_{\perp}$. However, experiments show that this approximation is not very accurate as the turbulent effects play a significant role in cross-filed transport.

After introducing the straightened-out model, the main conditions of the Simple SOL model can be listed as follows:

1. Electron T_e and ion T_i temperatures are constant along the field lines.
2. Electrons and ions are thermally decoupled.
3. The only source of plasma particles is cross-field transport from the main plasma. No ionization within the SOL.
4. No friction caused by collisions with neutrals.
5. The only particle sink and heat sink is the sheath at the limiter (or divertor) target. No recombination within the SOL and no radiative or charge-exchange cooling.

1.2.2 Plasma sheath

Plasma sheath is an important phenomenon associated with the SOL region, which appears on the interface of plasma and solid surface and has a significant impact on the particle transport.

When a charged particle impacts a solid surface, such as the limiter or the divertor target, it may become trapped or deposit its charge by recombination. Due to the higher thermal velocity of electrons, the negative charge is deposited at much faster rate and the surface becomes negatively charged. The resulting electric field attracts ions and repels low-energy electrons, creating a local concentration of net positive charge in a narrow region in front of the surface — the sheath. The magnitude of this local quasineutrality disturbance keeps increasing, until the ion current is able to balance out the electron current and an equilibrium is established.

At this point, the positive charge of the sheath shields most of the negative potential of the surface φ_{wall} (Debye shielding). Typically $\varphi_{\text{wall}} \approx -3kT_e/e$ with respect to the plasma potential. However, note that there is a small residual electric field, described by a pre-sheath potential drop $\varphi_{\text{pre-sh.}} \approx -0.5kT_e/e$, which still affects the SOL, see Fig. 1.6. The ions are accelerated toward the sheath, while the electrons are governed by a balance between the repulsion of electric field and the pressure gradient.

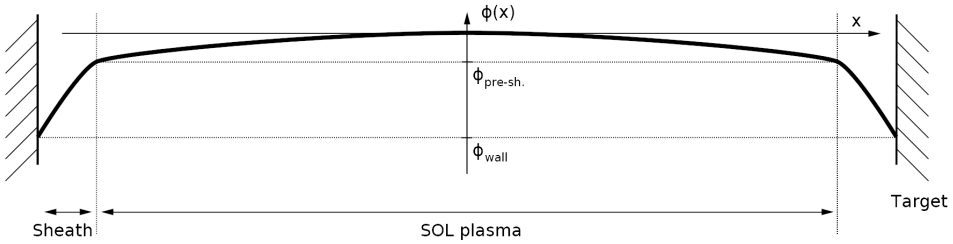

Fig. 1.6: Schematics of shielding a negative wall potential φ_{wall} by the plasma sheath. Small residual pre-sheath potential $\varphi_{\text{pre-sh.}}$ still affects the SOL plasma. Both φ_{wall} and $\varphi_{\text{pre-sh.}}$ are defined relative to the plasma potential.

One more important observation about the sheath is the Bohm criterion,

which and can be symbolically formulated as

$$v_{\text{sh.-in}} \geq c_{\text{s}} \tag{1.4}$$

The criterion simply states that the speed of plasma particles entering the sheath $v_{\text{sh.-in}}$ is always greater or equal to the ion acoustic speed c_{s}, equation (1.2). Relation (1.4) applies for cold plasma, where the ions and electrons are thermally decoupled and $T_{\text{e}} \gg T_{\text{i}} \approx 0$ can be assumed, which is one of the simple SOL conditions in 1.2.1. The relation is a useful tool for analytic modeling of SOL. Its derivation can be found for example in [7, Chapter 2]. A more generalized formulation of the criterion applies for $T_{\text{i}} > 0$ as well.

1.2.3 1d plasma flow along the field lines

Although there are numerous 2d computer models of SOL, it is usually not possible to carry out any significant 2d modeling analytically. Instead, a common approach is to separate parallel and cross-field directions and solve two 1d problems. [7, 13] A straightforward solution for the problem of the cross-field transport is given by the equation (1.3). The parallel transport is analyzed in this subsection.

The 1d ion fluid in hydrogen plasma ($Z = 1$) can be described by a pair of equations

$$\frac{\mathrm{d}}{\mathrm{d}x}\left(n_{\text{i}} v\right) = S_{\text{p}} \tag{1.5}$$

$$\cancelto{0}{m_{\text{i}} n_{\text{i}} \frac{\mathrm{d}v}{\mathrm{d}t}} + m_{\text{i}} n_{\text{i}} v \frac{\mathrm{d}v}{\mathrm{d}x} = e n_{\text{i}} E - \frac{\mathrm{d}p_{\text{i}}}{\mathrm{d}x} - m_{\text{i}} S_{\text{p}} v \tag{1.6}$$

where (1.5) represents the conservation of particles and (1.6) represents the conservation of momentum. The quantity S_{p}, units $\mathrm{s}^{-1}\,\mathrm{m}^{-3}$, is the volumetric rate of the particle source. In the case of the Simple SOL model, new charged particles are created by the ionization of slow neutrals in the main plasma, which then diffuse to the SOL.

Because the goal is to find a stationary solution, the first term in the second equation (1.6) can be omitted, leaving only the convection term on the left side. The right side combines the effects of electric field induced by electrons, effects of the ion pressure and the drag caused by particles coming from the particle source. The incoming particles cause drag, because as a whole their flow velocity is zero. Based on the isothermal assumption (see section 1.2.1), the pressure term can be replaced using the equation of state

$$\frac{\mathrm{d}p_{\text{i}}}{\mathrm{d}x} = k T_{\text{i}} \frac{\mathrm{d}n_{\text{i}}}{\mathrm{d}x}. \tag{1.7}$$

The electric field term is not that simple and requires an analysis of the electron fluid. The electron fluid can be described by a similar pair of equations as (1.5) and (1.6). However, it can be shown that the convection term and the drag term are proportional to $m_{\text{e}}/m_{\text{i}}$ and thus negligible. So

the behavior of the electron fluid is approximately determined by the balance between the electric field the and pressure gradient, which is the presumption of the Boltzmann relation

$$n_{\mathrm{e}}(x) = n_{\mathrm{e}0} \exp\left(\frac{e\varphi(x)}{kT_{\mathrm{e}}}\right). \tag{1.8}$$

By assuming the quasineutrality of plasma $n_{\mathrm{i}} = n_{\mathrm{e}}$ and substituting $E = -\mathrm{d}\varphi/\mathrm{d}x$, the term for electric field in the ion equation (1.6) can be rewritten as

$$en_{\mathrm{i}}E = -en_{\mathrm{i}}\frac{\mathrm{d}\varphi}{\mathrm{d}x} \overset{(1.8)}{=} -kT_{\mathrm{e}}\frac{\mathrm{d}n_{\mathrm{i}}}{\mathrm{d}x}, \tag{1.9}$$

where the second step is derived from the Boltzmann equation by applying $\mathrm{d}/\mathrm{d}x$.

The terms (1.7) and (1.9) can be substituted in the original set of ion fluid equations (1.5) and (1.6), the second equation can be divided by ion mass m_{i}

$$\frac{\mathrm{d}}{\mathrm{d}x}(nv) = S_{\mathrm{p}} \tag{1.10}$$

$$nv\frac{\mathrm{d}v}{\mathrm{d}x} = -\frac{k\left(T_{\mathrm{i}} + T_{\mathrm{e}}\right)}{m_{\mathrm{i}}}\frac{\mathrm{d}n}{\mathrm{d}x} - S_{\mathrm{p}}v \tag{1.11}$$

The index for density n_{i} was omitted, because the equations now describe the combined plasma fluid, electrons and ions together. Note that the temperature factor on the right side equals to the square of ion acoustic speed c_{s}^2, see (1.2). In fact, after combining the equations (1.10) and (1.11) (by eliminating $\mathrm{d}n/\mathrm{d}x$), it is convenient to go further and replace v with dimensionless Mach number

$$M = v/c_{\mathrm{s}} \tag{1.12}$$

and formulate the final result as follows

$$\frac{\mathrm{d}M}{\mathrm{d}x} = \frac{S_{\mathrm{p}}}{nc_{\mathrm{s}}} \cdot \frac{1 + M^2}{1 - M^2}. \tag{1.13}$$

Next step is to analyze the equation (1.13). Since the factor $S_{\mathrm{p}}/nc_{\mathrm{s}}$ is inherently positive, the sign of $\mathrm{d}M/\mathrm{d}x$ is given by the second factor. Assuming that the flow starts at subsonic speeds $M < 1$ at a symmetry point between the targets, the derivative is always positive and the flow accelerates towards the targets. However, the singularity $M \to 1$ suggests that the flow cannot exceed the acoustic speed $v \leq c_{\mathrm{s}}$. When combined with the Bohm criterion (1.4), it hints at an interpretation that the singularity is reached at the plasma-sheath interface and that plasma enters the sheath with

$$v_{\text{sh.-in}} = c_{\mathrm{s}}. \tag{1.14}$$

Based on this reasoning, [7] presents simple solutions for $n(x)$ and $\varphi(x)$ evaluated at the plasma-sheath interface in the ideal simple SOL model. The plasma density $n_{\text{sh.}}$ at the sheath entry point

$$n_{\text{sh.}} = \frac{1}{2}n_0, \tag{1.15}$$

where n_0 is density at the symmetry point, and the pre-sheath potential fall $\varphi_{\text{pre-sh.}}$, i.e. the potential not shielded by sheath,

$$\varphi_{\text{pre-sh.}} \approx -0.7\frac{kT_\text{e}}{e}. \tag{1.16}$$

According to [7] it should be noted that these solutions are very general in the sense that they are completely independent of the particle source S_p.

A more detailed analysis of equation (1.13) would require specifying the particle source S_p. It should be mentioned that there are two source mechanisms that usually dominate the SOL. One is the local ionization of neutrals by electrons, which can be described using known ioniz. rate coefficients. The other one is the cross-field diffusion, which is not a true source of ions but appears such in 1d analysis.

1.3 Transition to the Complex SOL model

This section outlines the main differences between the Simple and the Complex SOL model, the deficiencies of the former and the improvements of the latter. In general, limiter SOLs are often simple and divertor SOLs are often complex. Complex SOL is harder to understand and analyze than simple SOL, but it is more advantageous in the context of tokamak operation. Detailed formulation of a Complex (Divertor) SOL model and analysis of its results is beyond the scope of this thesis. Refer to [7, Chapter 5] for further reading.

1.3.1 Conditions of the complex SOL

A complex SOL is characterized by the fact that some, or none, of the simple SOL conditions listed in 1.2.1 do not apply. Thus, the conditions can be reformulated as follows:

1. There are non-zero parallel gradients of temperature.
2. Collisions between electrons and ions are frequent enough to transfer thermal energy.
3. Ionization of neutrals and power loses due to radiation within the SOL volume.
4. Friction caused by collisions with neutrals.
5. Recombination within the SOL volume if T drops below a few eV.

Note that this list only highlights the most important complicating factors and is by no means final. According to [7], there are many other factors which could be considered.

1.3.2 Parallel temperature gradients

The conditions 1.2.1 of the Simple model assume that the temperature of plasma is constant along the length of the SOL. In limiter configuration the SOL is always in contact with the main plasma and the connection length $L_{\parallel}$ is usually short, therefore the assumption can be reasonable. That is not the case for divertor configuration, since it introduces the separated downstream regions and it significantly extends the $L_{\parallel}$ together with the dwell time τ_{sol}. Suddenly, the finite thermal conductivity of the relatively cool SOL plasma (Spitzer-Harm conductivity $\propto T^{5/2}$) may become an important constraint, which creates significant temperature gradients.

Based on the magnitude of temperature gradients, the analytical models recognize multiple distinct regimes of heat transport in SOL. When the temperature gradients are negligible, the heat transport is dominated by the particle flux (convection) and the only important element influencing the transport is the sheath. This is the *flux-limited* or *sheath-limited* regime and it is characteristic of the Simple SOL model.

When the opposite is true, the dominating factor, as mentioned above, is the thermal conductivity. The effect of the sheath loses significance. The SOL is then said to be in a *conduction-limited* regime, which is characteristic of the Complex SOL model and divertor configurations.

It ought be stressed that the term 'limited' does not refer to the heat transport itself. The power leaving the plasma is fixed and independent of the regime. What is limited are the properties of SOL plasma, the temperature and density.

1.3.3 Local ionization and radiation loses

There are several outcomes of an interaction between plasma particle and the limiter or divertor target. One option is that the particle recombines at surface and bounces back without being captured. This is called *recycling* and it is the primary source of hydrogen (fuel) neutrals. And ionization of these recycled neutrals is the primary source of SOL plasma particles.

In simple SOL, the ionization occurs in the main plasma and the ionized particles enter SOL more or less homogeneously distributed along its length. In complex SOL, the collisions are frequent enough that the ionization can occur within the SOL volume. Since the highest concentration of recycled particles is close to the target, where they are produced, the majority of ionization processes is localized there as well. Thus the source of plasma particles is not homogeneously distributed. This helps to establish a parallel temperature gradient and the conduction-limited regime.

Volume power loses via radiation in the main plasma negatively affect the confinement and need to be minimized. However, in the SOL region these power loses are in fact desirable. When a significant fraction of incoming power P_{SOL} is radiated away before it reaches the target, for example in the *detached* regime (see below), the overall power density is decreased, which helps to lower the thermal strain of material. Additionally, the power losses

also support the parallel temperature gradient and reduce the temperature of plasma near a divertor target.

1.3.4 Advanced regimes of the complex SOL

Several factors, including the radiative power losses and establishing parallel temperature gradient, may actively reduce the plasma temperature near a divertor target T_t. Note that this is generally not possible for limiter configuration, where the connection length $L_{\parallel}$ is not long enough to induce a significant temperature gradient. When T_t is reduced further and further, the complex SOL transitions to different regimes beyond the conduction-limited regime. Each of these regimes is progressively more advantageous in terms of power management.

Initially, hot plasma particles interact directly with the target surface and the heat flux is focused onto a relatively small area. This changes with the advanced regimes, which are listed here in the order of decreasing temperature T_t[7]:

1. First comes the *high recycling* regime, which is sometimes used interchangeably with the *conduction-limited* regime. As the name suggests, the plasma-surface interaction is dominated by the recycling process and SOL becomes self-sufficient in terms of plasma particles. Low T_t and high saturation of walls with hydrogen atoms mitigates other processes such as the adsorption and sputtering. However, all the power still reaches targets.

2. Next transition is the *strongly radiating* regime. Low T_t prolongs the time before a recycled hydrogen atom is ionized again, which results in more excitations and subsequent radiation loses. Similarly, the radiation from low Z impurities also increases because their radiation function has maximum at very low temperatures. So a portion of the power is radiated, but the radiating zone is often still very close to the targets.

3. The final regime is the *detached* regime. At very low T_t the neutral friction and volume recombination may become a significant factor. The result is a 'cushion' of neutral gas, which prevents almost all direct plasma-surface interaction and redistributes the incoming power by means of isotropic radiation.

Note that there are no precise thresholds between the regimes, particularly between 1. and 2., the transitions are usually gradual.

1.4 Power balance in tokamak

Tokamak is a thermonuclear fusion reactor. Its purpose is to confine hot plasma for an extended period of time so that the probability of the rare fusion reactions becomes large enough to generate a sustained power output. The confinement of plasma energy and particles is never ideal. Instead, the

energy is continuously channeled away by plasma radiation and by cross-field transport into the SOL. When the power generated from fusion reactions is unable to fully compensate the losses, an external power input (plasma heating) needs to be introduced. A relation between all of these factors is referred to as the *power balance* and it is vital in relation to the application of tokamak as a fusion power source.

1.4.1 The power balance equation

The power balance in tokamak can be described by the following equation

$$\frac{\mathrm{d}W_\mathrm{p}}{\mathrm{d}t} + P_\mathrm{L} = P_\mathrm{I} + P_\mathrm{H}, \tag{1.17}$$

where the left-hand side represents the power consumption and the right-hand side is the power input. The consumption is a sum of the increase in confined plasma energy W_p and the power losses P_L. It is balanced out by the the internal power input P_I from the fusion reactions and the external power input P_H provided by the plasma heating components. It should be noted that the fusion input term P_I is relevant only in the context of large experiments such as JET and ITER, smaller experiments primarily focus on the confinement of plasma without fusion reactions.

Equation (1.17) describes the power balance in the most general case. A common simplification is the stationary balance

$$P_\mathrm{L} = P_\mathrm{I} + P_\mathrm{H}, \tag{1.18}$$

where the change in plasma energy is neglected $\mathrm{d}W_\mathrm{p}/\mathrm{d}t \approx 0$. This assumption is reasonable during the so-called *flat-top* phase of a tokamak discharge, when the plasma current is approximately constant as well as any other sources of heating power.

In the absence of any input power, the balance (1.17) simplifies to $\mathrm{d}W_\mathrm{p}/\mathrm{d}t = -P_\mathrm{L}$, which represents a spontaneous cooling-down of the confined plasma. Based on this relation, the confinement time τ_E is defined as

$$\tau_\mathrm{E} = \frac{W_\mathrm{p}}{P_\mathrm{L}} \tag{1.19}$$

The confinement time is an important characteristic quantity in fusion physics and it describes the effective energy inertia of the confined plasma. It is used to formulate the Lawson criterion [6, chapter 1] and as a parameter in empirical scaling laws.

1.4.2 Power losses and heating power

The two main mechanisms of power losses in a tokamak is the plasma radiation and the cross-field transport. Hot plasma emits intensive bremsstrahlung, which is a radiation of free moving charged particles with a continuous spectrum, in combination with various sources of line radiation from both

the fuel particles and the impurities. Tokamak plasma is optically thin, and therefore majority of the radiated energy leaves the volume of confined plasma and it is deposited on the first wall.

The other mechanism is the cross-field transport of energy and particles. While the magnetic field of a tokamak can confine a solitary charged particle, the collisions between plasma particles still induce a slow cross-field transport via diffusion, banana trajectories and other related processes. Beside the collisional processes, the cross-field transport is also induced by non-collisional turbulent processes, which originate from plasma instabilities. Therefore the confined plasma continuously loses heat and particles to the SOL region, which then channels them towards the limiter or divertor targets where the energy is dissipated by interaction with solid material. Depending on the regime of SOL transport, the energy may be also dissipated by radiation as discussed in section 1.3.4.

As was mentioned before, fusion power is often insufficient to compensate the losses and external plasma heating components need to be introduced. The foundation of every tokamak is the ohmic heating by plasma current, which is generated primarily by electromagnetic induction. The main disadvantage of the induction heating is its inherent pulse-like nature and the fact that the ohmic heating loses efficiency with increasing plasma temperature. Thus, the ohmic heating is typically combined with other alternatives such as the neutral beam injector (NBI) or heating by electromagnetic waves (ECRH, ICRH), which offer a reasonably efficient and continuous power input. The COMPASS tokamak features two NBI devices, each delivering up to 400 kW of heating power in a beam of neutral particles with 40 keV of energy per particle.

Chapter 2

Models of inter-ELM power decay length

This chapter introduces the power decay length λ_q, which is an important practical quantity in the context of SOL plasma research. It can be used to characterize one of the most significant limiting factors of large tokamak devices — the heat strain of the divertor target. Understanding this quantity and how it scales between devices is essential for the design of future tokamaks. Following that, several recent findings in this field of research that focus mainly on the ELMy H-mode plasma are presented and discussed.

2.1 Power decay length

As described in section 1.1, particles that escape the main plasma travel along the open filed lines through the SOL and divertor regions, before colliding with the divertor target. When a particle impacts the target, a significant portion of its energy can be deposited on the solid surface in the form of heat. Therefore, a steady flow of impacting plasma particles creates a heat flux $q_{\parallel}$ [$\mathrm{W\,m^{-2}}$], where $\parallel$ refers to the direction parallel to the field lines. The theoretical model from section 1.2 approximates the SOL plasma as a thin layer, where plasma density and temperature follows an exponential decay in the radial (cross-field) direction. It can be assumed that a radial profile of the particle heat flux $q_{\parallel}$ bears similar characteristics. Mainly, that the majority of particles impacts the surface near the strike point and that beyond some characteristic width, decay length, $q_{\parallel}$ quickly decays. An example of a heat flux profile measured on the COMPASS tokamak divertor can be seen in Fig. 2.1.

Power decay length, or power width, λ_q, is a practical quantity that characterizes the heat flux profile. By convention, λ_q is projected to outer midplane rather than measuring it directly at the divertor, so that the effects of flux expansion specific to divertor geometry are removed [22]. Refer to section 2.1.2 for more information about flux expansion. The next section introduces several different alternatives to how the decay length is calculated.

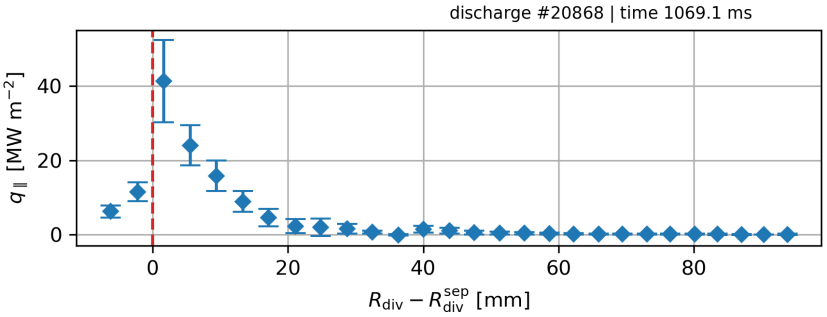

Fig. 2.1: Example of $q_{||}$ radial profile measured using divertor probe array in the COMPASS tokamak. Position of the separatrix is marked by the dashed line.

2.1.1 Experimental estimation of decay length

There are three common methods used to calculate the power decay length [22]:

1. integral decay length
2. full width at half maximum (FWHM)
3. parameter in exponential fit $\sim \exp(-x/\lambda_q)$

All of these methods operate with the assumption that the shape of the profile is dominated by one main peak close to the separatrix, which slopes down exponentially. Despite sharing this strong assumption, the methods often produce slightly different results.

The integral decay length, method 1., is defined by a following relation [23]

$$\lambda_q^{\text{int}} \equiv \frac{\int_{\text{div}} q(s) 2\pi R(s) \mathrm{d}s}{2\pi R_{\text{peak}} q_{\text{peak}}} \cdot f_{\text{x}}, \tag{2.1}$$

where $q = q(s)$ is the divertor heat flux profile, q_{peak} is its peak value and R_{peak} is the corresponding coordinate. Quantity f_{x} is the flux expansion factor (2.5). The heat flux q [W m^{-2}] is integrated over the surface of divertor target, which is described by s and R coordinates and assumed to be toroidally symmetric. $R = R(s)$ is the toroidal radius and s is the profile coordinate along the curve of the divertor surface when projected to the poloidal plane. Often the heat flux profile features a steeper component with short decay length near the separatrix and a tail with long decay length [22]. The main feature of the integral method is that it considers the full span of the profile including the tail in the far SOL [23], which results in wider λ_q values. Although, it may be argued that such results are perhaps misleading and that other methods, which focus on the main peak close to separatrix, should be preferred.

The FWHM decay length, method 2., is calculated as a FWHM of the main heat flux peak. While FWHM is a straightforward and widely accepted measure of peak-dominated profiles, it characterizes only the single main

peak close to the separatrix. It ignores both secondary peaks, which can be occasionally observed, and the tail of the profile.

The decay length can be also obtained by finding the best fit of the profile with an exponential function[19], method 3.,

$$q(\bar{s}) = q_0 \cdot \exp\left(-\frac{\bar{s}}{\lambda_q f_{\mathrm{x}}}\right), \quad \text{where } \bar{s} = s - s_{\mathrm{sep}}, \ s \in [s_{\mathrm{sep}}, +\infty). \tag{2.2}$$

Here $q = q(\bar{s})$ is the heat flux profile; peak heat flux q_0 and decay length λ_q pose as the fit parameters. The f_{x} is the magnetic flux expansion factor (2.5). The transformed coordinate $\bar{s}$ is determined by the position of the separatrix at the divertor target s_{sep}, i.e. the strike point. Notice that the formula applies only beyond the strike point $s \geq s_{\mathrm{sep}}$. In the private flux region $s < s_{\mathrm{sep}}$ the heat flux is either assumed to be $q(\bar{s}) \approx 0$ or it is also fitted with (2.2) mirrored at the strike point producing a secondary λ_q.

The formula (2.2) is based on a simple model of the upstream SOL region, where the main influence is cross-field diffusion from the main plasma, see section 1.2. However, the conditions are different in the divertor region, where the neighboring high-density main plasma and its the density gradient no longer dictates the cross-field transport. A common observation is a bi-directional diffusion both into the private-flux region and outwards, which results in the dispersion of the profile. The exact processes that dominate the diffusion are unknown and subject of current research. Eich[19] proposes that this can be accounted for by introducing a Gaussian function with a width parameter S. The improved model of a heat flux profile is then given by a convolution of (2.2) with the Gaussian

$$q(\bar{s}) = \frac{q_0}{2} \cdot \exp\left[\left(\frac{S}{2\lambda_q f_{\mathrm{x}}}\right)^2 - \frac{\bar{s}}{\lambda_q f_{\mathrm{x}}}\right] \cdot \operatorname{erfc}\left(\frac{S}{2\lambda_q f_{\mathrm{x}}} - \frac{\bar{s}}{S}\right), \quad \bar{s} \in (-\infty, +\infty). \tag{2.3}$$

A comparison of the original exponential model (2.2) and the Eich model (2.3) is shown in Fig. 2.2.

Notice that for $S \to 0$ the function (2.3) approaches the original profile (2.2). Also, in this case the s_{sep}, as defined in (2.2), does not have to be specified explicitly. Since the function domain is not limited by the strike point, it is possible to regard s_{sep} as an additional parameter of the fit, together with q_0, λ_q and S. When specifying s_{sep} explicitly, an estimate from magnetic equilibrium reconstruction has to be used. The equilibrium estimate may however differ from the reality as a result of the involvement of magnetic drifts in the divertor region, which is discussed for example in [13]. Finally, when the profile is measured by an infrared camera, a background parameter q_{bg} should be included as well $\tilde{q}(\bar{s}) = q(\bar{s}) + q_{\mathrm{bg}}$. It accounts for the plasma radiation, which causes a weak background in the IR band as well as additional, approximately homogeneous, heating of the target.

The power decay length λ_q^{int} estimated using the integral method (2.1) should be equal to the FWHM and fit method (2.2), assuming the profile is an

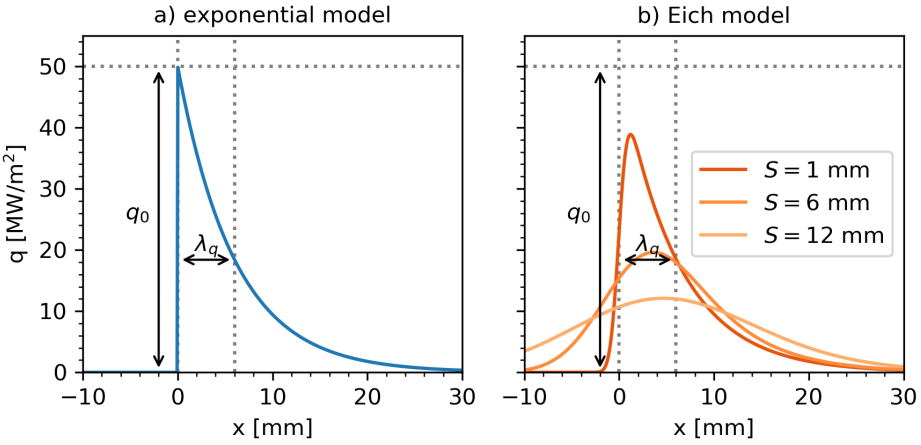

Fig. 2.2: Comparison of the models for the particle heat flux profile in SOL plasma. The figure shows the exponential model (2.2), graph a), and the Eich model (2.3), graph b).

ideal exponential function with constant decay length. However, the results of the improved fit method (2.3) deviate depending on the S parameter. Makowski[24] shows that

$$\lambda_q^{\text{int}} \approx \lambda_q + 1.64 \cdot S, \tag{2.4}$$

where λ_q^{int} is the integral decay length and λ_q is the estimation from (2.3). The relation is satisfied with good approximation (error $< 4\,\%$ for $S/\lambda_q < 10$) when a reasonable fit of $q(\bar{s})$ data is achieved.

2.1.2 Magnetic flux expansion and projection to outer midplane

The magnetic flux expansion factor is used to project decay lengths measured at the divertor target to a more standardized location, typically the outer midplane. It is an attempt to mitigate effects of varying divertor geometry between tokamaks — namely the expansion of the magnetic flux due to the difference in strength of the poloidal magnetic field between the upstream and downstream regions. In this way, the decay lengths can be compared across multiple devices to discover the main underlying effects that define the parameters of SOL plasma.

The (effective) magnetic flux expansion factor is defined as

$$f_{\text{x}} = \frac{R_{\text{div}} B_\theta^{\text{div}}}{R_{\text{omp}} B_\theta^{\text{omp}}} \frac{1}{\sin\beta}, \tag{2.5}$$

where R is the toroidal radius coordinate, B_θ is the poloidal magnetic field and β is the angle between the field lines and the surface. The labels *div* and *omp* refer to position at the divertor target and at outer midplane. Since both spatial coordinate (R) and magnetic filed (B_θ, $\sin\beta$) vary across the surface

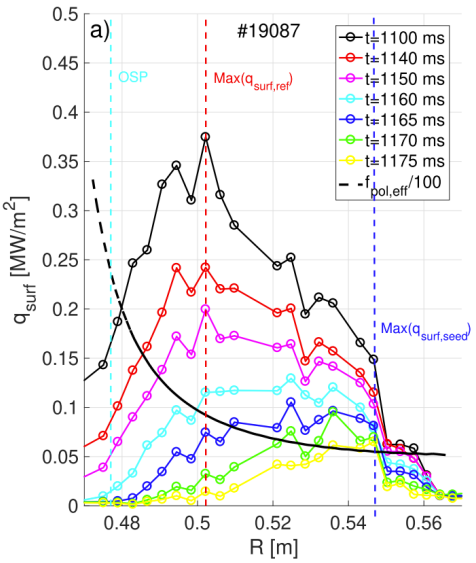

Fig. 2.3: Heat flux profile and flux expansion $f_x \equiv f_{pol,eff}$ profile along the LFS divertor target in the COMPASS tokamak. f_x profile is plotted in black and it is monotonously decreasing outwards (to the right) from the outer strike point (OSP). Published in [26]

of the target, it is obvious that f_x is not constant. However, the difference between f_x in the area close to the strike point and further away is often very small, e.g. a few percent[19]. Then the f_x is considered to be approximately constant.

When f_x varies significantly along the divertor target, the alternative is to use profile mapping based on MHD equilibrium reconstruction. To reconstruct the equilibrium, numerical codes such as EFIT[25] are typically employed. The equilibrium can then be used to remap the heat flux profile from divertor to a different physical location along the magnetic surfaces, for example to the outer midplane. The power decay length is estimated from the remapped profile by one of the methods listed in section 2.1.1, omitting the flux expansion factor $f_x \equiv 1$.

Profile of the flux expansion factor along the LFS divertor target in the COMPASS tokamak is plotted in Fig. 2.3. The factor varies significantly in range 25-5, decreasing from strike point outwards.

2.1.3 Upstream decay lengths

As mentioned above, the power decay length is primarily measured by divertor diagnostics (probes, IR camera), i.e. in the downstream regions. One of the reasons is simply the (un)availability of diagnostic systems. According to chapter 3, which lists the three most common diagnostics relevant to power width research, both the probe array and infrared camera measurements are localized to the divertor target. The only viable option to measure radial plasma profiles in the upstream SOL is the Thomson scattering (TS), which

has rather low temporal resolution.

Despite the difficulties, comparing properties of upstream SOL plasma and divertor plasma is certainly a scientifically interesting task. Stangeby[22] presents two simple models that relate the upstream electron temperature $\lambda_{T_e}^{up}$ and density $\lambda_{n_e}^{up}$ widths with divertor power width λ_q. The first model, the *conduction-limited* model, describes collisional plasma, where the heat transport is dominated by Spitzer-Harm (thus SH superscript) heat *conduction* of electrons

$$\lambda_q^{SH} \approx \frac{2}{7}\lambda_{T_e}^{up}. \tag{2.6}$$

The second model, *flux-limited* model, describes plasma with weak collisionality, where the particle *flux* dominates heat transport

$$\frac{1}{\lambda_q^{fl}} \approx \frac{3/2}{\lambda_{T_e}^{up}} + \frac{1}{\lambda_{n_e}^{up}}. \tag{2.7}$$

In order to decide, which model applies, the (normalized) collisional frequency of SOL electrons needs to be estimated

$$\nu^*_{\text{e-SOL}} \equiv \frac{L_\parallel}{\lambda_{ee}} \approx 10^{-16}\frac{n_{\text{up}}L_\parallel}{T^2_{\text{e-up}}} \quad [\text{m}^{-3}, \text{m}, \text{eV}], \tag{2.8}$$

where $L_\parallel$ is the connection length, defined in section 1.2.1, n_{up} is upstream density, $T_{\text{e-up}}$ is upstream electron temperature and λ_{ee} is mean free path for electron-electron collision. The Spitzer-Harm conductivity, i.e. the conduction-limited model, fully holds for $\nu^*_{\text{e-SOL}} \gtrsim 50$, while the flux-limited model applies approximately when $\nu^*_{\text{e-SOL}} \lesssim 1$. [7, 22]

2.2 Published power decay length scaling regressions

This section serves as an overview of several recently published results on the topic of power decay length λ_q scaling in H-mode discharges. Presented are the methods of measuring λ_q, viable scaling parameters and important results of the regression analyses. The main motivation of the collective research is to extrapolate the scaling laws and provide predictions for the ITER tokamak.

2.2.1 Goldston 2011

Goldston[27] introduced a heuristic model for SOL power width in H-mode plasma based on theory of Pfirsch-Schlüter flows, which are caused by vertical magnetic drifts. The model assumes non-turbulent particle transport coupled with anomalous electron thermal transport. It is relevant at zero or very low gas-puff rates and with outgassed walls, when any volumetric particle sources

are negligible and the plasma is well attached to the divertor. The prediction of divertor power width can be formulated for ${}^{2}_{1}\mathrm{D}$ plasma as

$$\lambda_q \approx 5671 \cdot 2^{7/16} \cdot P_{\mathrm{SOL}}^{1/8} \frac{(1+\kappa^2)^{5/8} a^{17/8} B^{1/4}}{I_{\mathrm{p}}^{9/8} R_0} \left(\frac{Z_{\mathrm{eff}}+4}{5}\right)^{1/8}, \tag{2.9}$$

where P_{SOL} refers to the power loses from main plasma to SOL via particle transport, B is the total magnitude of magnetic field and I_{p} is the plasma current. R_0, a and κ refer to the canonical parameters of tokamak plasma geometry, i.e. major, minor radius and elongation respectively. All quantities are in SI units.

Finally, a reasonable quantitative agreement of relation (2.9) with experimental data from tokamaks C-Mod, DIII-D, JET and NSTX was presented.

2.2.2 Eich 2013

Report [5] introduced a substantial multi-machine database for the H-mode SOL power decay length λ_q, which combined data from 6 tokamak devices: JET, DIII-D, ASDEX Upgrade, C-Mod, NSTX and MAST. The main focus of this research paper was the regression analysis of power decay length measured during inter-ELM periods of H-mode discharges, which was motivated by the need of up-to-date predictions for future devices such as ITER and DEMO.

The inter-ELM periods were defined as 50–99 % of the ELM cycle, 30–99 % in the case of DIII-D. The decay length λ_q was estimated from data measured by infrared camera using the improved fitting method (2.3). A background parameter q_{bg} was added to account for black-body radiation of the target, see text below (2.3). Note that the regression was undertaken on the fit estimation of λ_q itself without relating it to the integral value using (2.4). The scaling analysis would have required including the S parameter, which is, however, strongly affected by the divertor geometry and is therefore unsuitable for universal inter-machine predictions. More precise ITER prediction, which would incorporate estimations of the S parameter based on the ITER divertor design, was instead proposed as a future next step.

Total of 11 different scaling parameters was considered, which included magnetic field (toroidal B_ϕ and poloidal B_θ at outer midplane), safety factor (q_{95}, q_{cyl}), vessel geometry, plasma geometry, and P_{SOL}, The regression analysis provided several statistically significant results, the two main being

$$\lambda_q = (0.63 \pm 0.08) \cdot B_\theta^{(-1.19 \pm 0.08)} \tag{2.10}$$

$$\lambda_q = (0.86 \pm 0.25) \cdot B_\phi^{(-0.80 \pm 0.21)} \cdot q_{\mathrm{cyl}}^{(1.11 \pm 0.15)} \cdot P_{\mathrm{SOL}}^{(0.11 \pm 0.09)} \cdot R_0^{(-0.13 \pm 0.16)} \tag{2.11}$$

where λ_q [mm], B_θ and B_ϕ [T], q_{cyl} [–], P_{SOL} [MW], R_0 [m].

The first result (2.10) (labeled in [5] as scaling #14), which states approximately $\lambda_q \propto 1/B_\theta$, was sufficient to describe the entire database of 6 devices and it represented the strongest single-parameter dependency. The

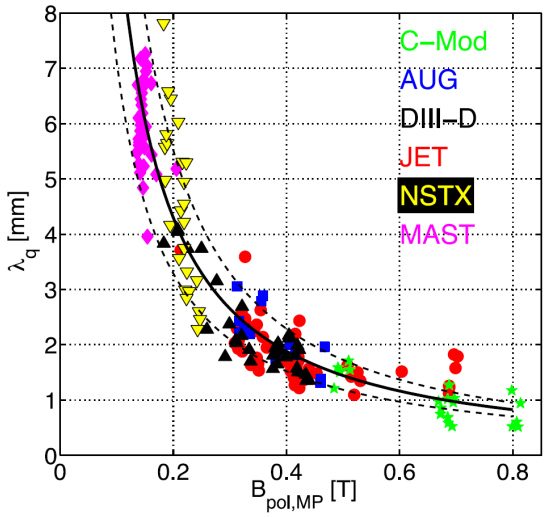

Fig. 2.4: Single-parameter scaling of power decay length λ_q vs. poloidal field $B_{\mathrm{pol}} = B_\theta$. Results from report Eich2013[5], equation (2.10).

scaling is visualized in Fig. 2.4. The second result (2.11) showed a promising accordance with the prediction based on the heuristic drift-based model (2.9), when the database was limited to devices with conventional aspect ratio, i.e. JET, DIII-D, ASDEX Upgrade.

To clarify the relationship between the model (2.9) and result (2.11), the relation (2.9) can be simplified and approximated as follows

$$\lambda_q \propto P_{\mathrm{SOL}}^{1/8} \frac{a^{17/8} \hat{\kappa}^{10/8} B^{1/4}}{(a\hat{\kappa}\langle B_\theta\rangle)^{9/8} R_0} \approx P_{\mathrm{SOL}}^{1/8} \frac{B_\phi^{9/8} a}{\langle B_\theta\rangle^{9/8} R_0} \frac{B^{2/8}}{B_\phi^{9/8}} \approx P_{\mathrm{SOL}}^{1/8} \frac{q_{\mathrm{cyl}}^{9/8}}{B_\phi^{7/8}}. \tag{2.12}$$

Weak dependency on Z_{eff} was omitted and $I_{\mathrm{p}}^{9/8}$ was substituted using

$$\langle B_\theta\rangle = \frac{I_{\mathrm{p}}\mu_0}{2\pi a\hat{\kappa}} \quad \Leftrightarrow \quad I_{\mathrm{p}}^{9/8} = \left(\frac{2\pi}{\mu_0} a\hat{\kappa}\langle B_\theta\rangle\right)^{9/8} \tag{2.13}$$

where

$$\hat{\kappa} = \sqrt{\frac{1+\kappa^2}{2}}. \tag{2.14}$$

Remaining factor $\hat{\kappa}^{1/8}$ was omitted as well (weak dependency), expression $1 = B_\phi^{9/8}/B_\phi^{9/8}$ was inserted and approximation $B^{2/8} \approx B_\phi^{2/8}$ was used. Finally, the cylindrical safety factor q_{cyl} can be formulated as

$$q_{\mathrm{cyl}} = \frac{aB_\theta}{\sqrt{2}\langle B_\theta\rangle R_0}. \tag{2.15}$$

Below are listed four other scaling models from this report (scaling #3, #5, #9 and #11) that which are referenced further on in the context of report

Maurizio2021[28]

$$\lambda_q = 0.65 \cdot B_\theta^{-1.11} \tag{2.16}$$
$$\lambda_q = 0.52 \cdot B_\theta^{-0.92} \cdot q_{95}^{0.25} \cdot R_0^{0.10} \tag{2.17}$$
$$\lambda_q = 0.70 \cdot B_\phi^{-0.77} \cdot q_{95}^{1.05} \cdot P_{\mathrm{SOL}}^{0.09} \cdot R_0^{0.00} \tag{2.18}$$
$$\lambda_q = 0.52 \cdot B_\phi^{-0.63} \cdot q_{95}^{0.95} \cdot P_{\mathrm{SOL}}^{0.05} \cdot R_0^{0.21} \cdot f_{Gw}^{-0.48} \tag{2.19}$$
$$\tag{2.20}$$

where λ_q [mm], B_θ and B_ϕ [T], q_{cyl} [–], P_{SOL} [MW], R_0 [m].

2.2.3 Brunner 2018

Report [29] extended the multi-machine H-mode database[5] with new measurements from Alcator C-Mod. As a result of that, the range of B_θ was increased above the expected ITER-level and near the level of reactor-class tokamak up to $\sim 1.3\,\mathrm{T}$, see Fig. 2.5. An array of divertor probes with high spatial resolution was used to estimate λ_q. In this case, the heat flux profile was not described well by the improved fitting model (2.3) and a multi-λ_q model was introduced instead, which is a combination of 4 exponential functions with 4 different λ_q parameters. The new data further confirmed the original prediction (2.10).

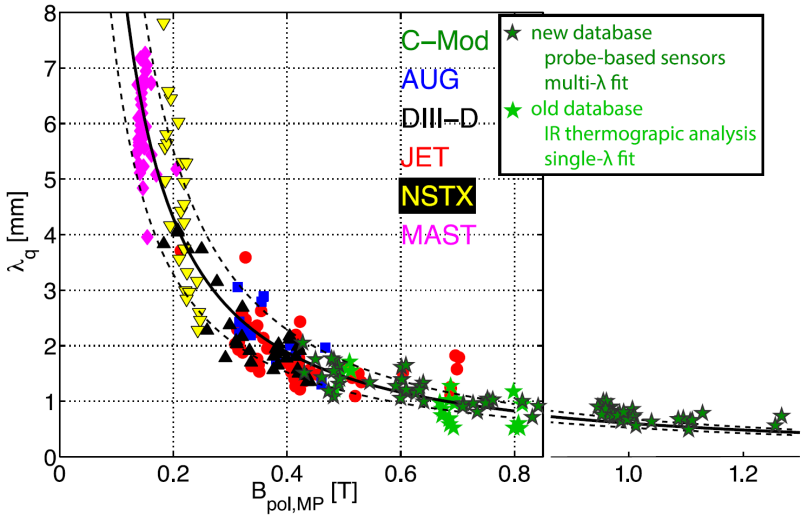

Fig. 2.5: The extended multi-machine database from report Brunner2018[29], original database is shown in Fig. 2.4. The new data from C-Mod support the earlier findings.

The report also included a multi-regime analysis of heat fluxes, which compared H-, L- and I-mode plasma. The single-parameter B_θ scaling was shown to be different for each of the mentioned modes, the exponents varied between -0.6 and -1.0, see Fig. 2.5. Another scaling was proposed, which was

based on the volume-averaged core plasma pressure $\bar{p}$

$$\bar{p} = \frac{2}{3}\frac{W_{\mathrm{MHD}}}{V}, \tag{2.21}$$

where W_{MHD} is the stored plasma energy and V is the plasma volume. The equation shows that $\bar{p}$ strongly relates to the stored energy and, by extension, to the quality of confinement. The respective scaling result

$$\lambda_q = (8.35 \pm 0.09) \cdot \bar{p}^{(-0.48\pm0.01)} \quad [\mathrm{mm; kPa}], \tag{2.22}$$

which can be interpreted approximately as $\lambda_q \propto \sqrt{1/\bar{p}}$, appeared to unify the confinement regimes. See Fig. 2.6.

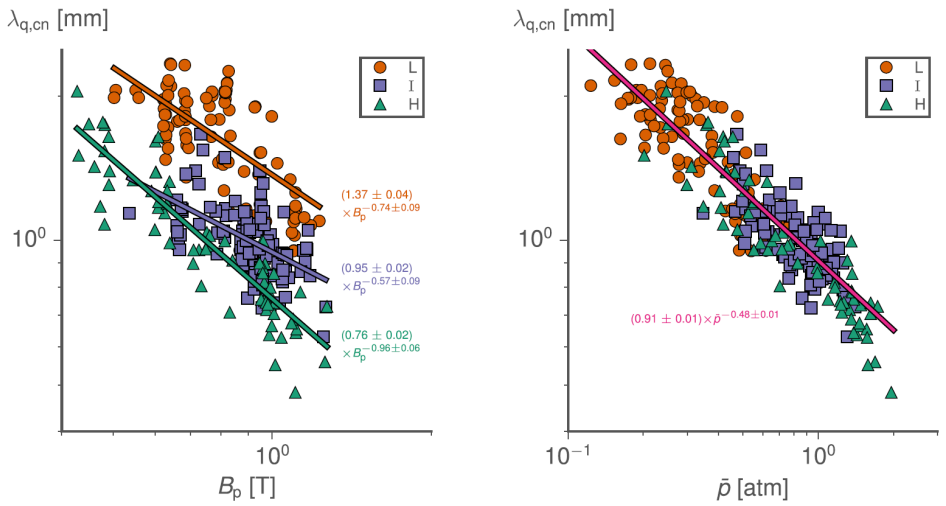

Fig. 2.6: Comparison of poloidal field $B_{\mathrm{p}} = B_\theta$ scaling and pressure $\bar{p}$ scaling in multi-regime databse from report Brunner2018[29]. The $\bar{p}$ scaling appears to unify the regimes.

Projections for λ_q in future devices based on (2.22) were similar to those based on the poloidal magnetic field (2.10). However, it was argued that the inverse dependence on core plasma pressure $\bar{p}$ ($\sim$ plasma confinement) implies unfortunate consequence for reactors. Namely that the quality of core plasma confinement can be improved only at the expense of narrow heat flux to divertor.

2.2.4 Silvagni 2020

Report [30] was focused on the cross-regime analysis in ASDEX Upgrade (AUG), following the findings of Alcator C-Mod in [29]. In this case, both the downstream and upstream measurements were obtained. Divertor heat flux was measured using an infrared camera and upstream profiles were measured using the Thomson scattering diagnostics (TS).

In addition to confirming the volume-averaged core plasma pressure dependence (2.22), the report explored several other related parameter options. A

regression against edge electron pressure p_e^{95}, which was obtained from TS pressure profile at $\rho = \sqrt{\psi_n} = 0.95$, was calculated. The result was a similar scaling prediction

$$\lambda_q = (2.45 \pm 0.02) \cdot (p_e^{95})^{(-0.34 \pm 0.01)} \quad [\mathrm{mm; kPa}]. \tag{2.23}$$

In the case of AUG, p_e^{95} was found to be more suitable for its cross-regime database; the λ_q values were less scattered and the resulting correlation coefficient of the regression was closer to unity. The results are shown in Fig. 2.7.

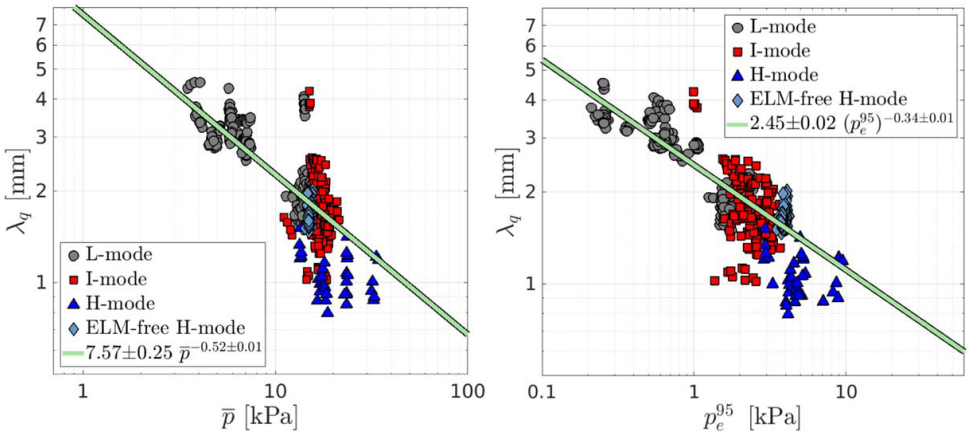

Fig. 2.7: Comparison of pressure scaling results from report Silvagni2020[30], the average core pressure $\bar{p}$ and the edge electron pressure p_e^{95}.

In I-mode and H-mode the p_e^{95} is an estimation of pressure at the pedestal top. It was argued that the p_e^{95} strongly relates to pedestal pressure gradient and the scaling (2.23) was interpreted as a relation between λ_q and the pedestal slope. Conclusion being that a steep pedestal slope is to result in small λ_q and narrow heat flux.

Additionally, upstream scaling was also analyzed using temperature λ_{T_e} (left) and density λ_{n_e} (right) profiles measured with TS. It was shown that the conduction-limited model (2.6) had been able to describe the cross-regime database well. Dependency of density width $\lambda_{n_e}^{\mathrm{up}}$ on λ_q expressed a large variation of values for wider power widths and appeared to be less significant. See Fig. 2.8 for comparison.

2.2.5 Horacek 2020

Report [31] examines power decay length λ_q scaling in L-mode plasma rather than in ELMy H-mode plasma. Despite that, it is relevant to the topic of this thesis because it included the COMPASS tokamak. A database of L-mode discharges was obtained by combining 5 tokamak devices: COMPASS, EAST, C-Mod, MAST and JET. With the exception of MAST, all devices used the single-null divertor configuration and measured λ_q using the divertor probe array. MAST used double-null configuration and IR camera, which was demonstrated to be consistent with its probe array.

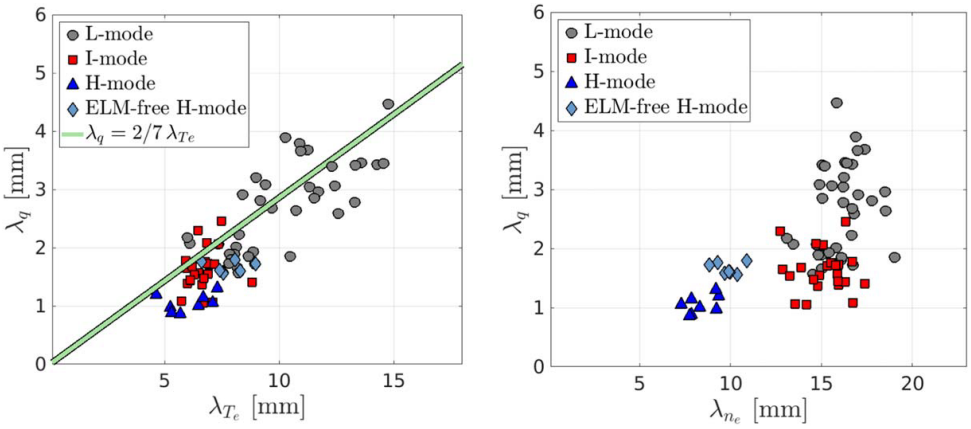

Fig. 2.8: Relation between upstream temperature T_e, density n_e decay lengths and the downstream power decay length λ_q. The conduction limited model (2.6) is shown for reference. Silvagni2020[30].

For the analysis of λ_q scaling, a set of 12 most prominent parameters was considered: $j_\mathrm{p}, B_\phi, B_\theta, \bar{n}_\mathrm{e}, P_\mathrm{SOL}/S_\mathrm{LCFS}$, $\bar{p}$, β, f_Gw, q_{95}, q_cyl, a/R_0, κ and δ_up. Many of the listed parameters are dimensionless, because the main aim of the report was to derive predictions for ITER without extrapolation. Presently, the largest operational tokamaks achieve only a half or a third of the ITER-scale in many important aspects of their design. Therefore, any prediction based on an absolute value of the parameters requires significant extrapolation, which arguably impacts the soundness of the prediction.

The report explored a significant number of parameter combinations and possible scaling predictions. While most of them were related to the L-mode plasma, a variant of the Brunner's average core pressure $\bar{p}$ scaling (2.22) was presented

$$\lambda_q = 0.024 \cdot \bar{p}^{-0.44} \left(\frac{a}{R_0}\right)^{-1.96} \beta^{-0.27} \tag{2.24}$$

The original scaling (2.22) was shown to apply universally for the H-, L- and I-mode regimes, therefore it may seem reasonable to assume that the new scaling (2.24) inherits this property as well despite the fact that it is based purely on the L-mode data.

Graphs Fig. 2.9 and Fig. 2.10 show examples of single-parameter scaling models, which include L-mode data from divertor probe array on the COMPASS tokamak. In both of these cases, the COMPASS data appears to deviate from the general trend given by other devices.

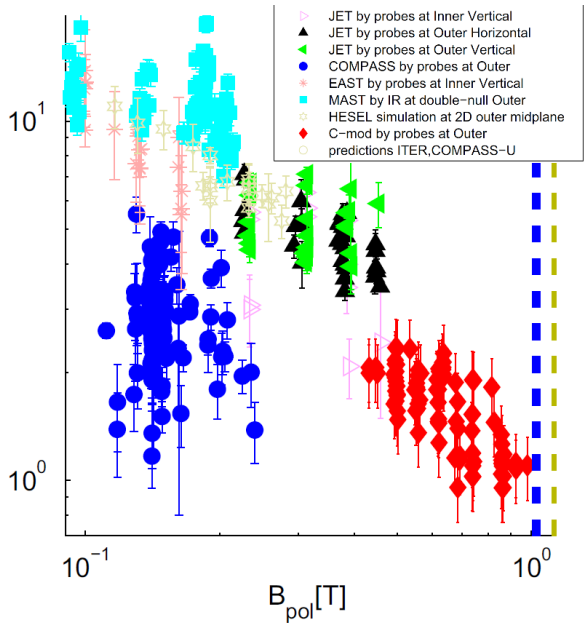

Fig. 2.9: Scaling of L-mode decay length λ_q in respect to the poloidal field B_θ. Data from COMPASS divertor probe array is marked in blue, notice that the λ_q values appear to be approx. $5\times$ smaller than the general trend given by data from the other tokamaks. Horacek2020[31].

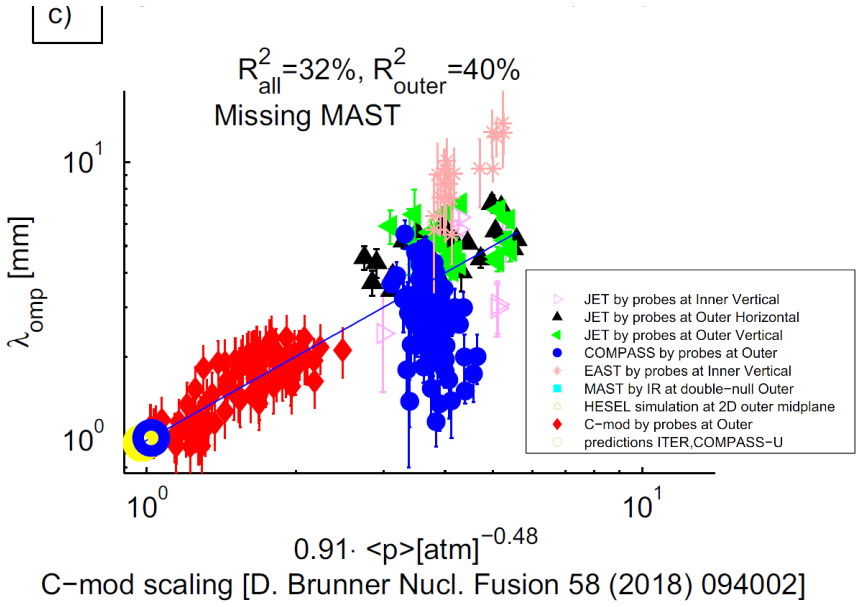

Fig. 2.10: Scaling of L-mode decay length λ_q in respect to the average core pressure $\bar{p}$, first introduced by Brunner (2.22). Data from COMPASS divertor probe array is marked in blue, notice the large variance of λ_q. Horacek2020[31].

2.2.6 Maurizio 2021

Report [28] tested the predictions of the λ_q multi-machine regression analysis from [5] and the upstream relations from [22] (presented in section 2.1.3) on the TCV tokamak. TCV is a medium-size device with major radius $R_0 = 0.88\,\mathrm{m}$ and minor radius $a = 0.25\,\mathrm{m}$. It is comparable to the COMPASS tokamak both in terms of the size (COMPASS: $R = 0.56\,\mathrm{m}$, $a = 0.23\,\mathrm{m}$) and magnetic field capabilities[10, 2]. Additionally, the TCV discharges used in this report [28] feature COMPASS-like parameters and the standard single-null divertor configuration was used for the experiments.

The divertor heat flux profile was measured using the infrared tomography system and the upstream temperature and density profiles were measured using the Thomson scattering diagnostics (TS). In both cases the profiles were mapped to outer midplane using the magnetic equilibrium reconstruction.

The relations between upstream and downstream measurements were tested in L-mode and ELM-free H-mode plasma, because in these regimes both IR and TS diagnostics yield a high signal amplitude. It was observed that the relation between upstream and downstream λ_q is reasonably well characterized by the flux-limited model (2.7) (low collisionality). For reference, the electron collisionality (2.8) was calculated using values of $T_{\text{e-up}}$ and $n_{\text{e-up}}$ at separatrix measured by TS. The calculation yielded $\nu^*_{\text{e-SOL}} \approx 14$, which according to thresholds from section 2.1.3 indicates moderate collisionality $1 \lesssim \nu^*_{\text{e-SOL}} \lesssim 100$.

The inter-ELM decay length predictions from report Eich2013[5] were tested on a database of 20 ELMy H-mode discharges with type-I ELMs. All discharges were in attached divertor regime. Reliability of IR measurements proved to be low due to relatively low divertor target heat loads and short integration times. Therefore, the upstream measurements from TS calculated using the flux-limited model (2.7) were used instead. The inter-ELM phase was defined as 60–95 % of the ELM cycle, ELMs were detected based on their characteristic spikes in D_α emission. The measured temperature and density profiles from a series of consecutive ELM cycles were grouped together to estimate the decay lengths.

The TCV results were compared with some of the λ_q scaling predictions from Eich2013[5], plots are shown in Fig. 2.11. In some cases there was a reasonable accordance (regressions #9 and #11 from [5]). However, in some other cases the predictions significantly overestimated the TCV results $\lambda_q^{\text{TCV}}/\lambda_q^{\text{scaling}} \approx 0.5$, including the case of the single-parameter poloidal field B_θ scaling (2.10). The 'anomalous' B_θ scaling of TCV inter-ELM decay length is also illustrated in comparison with data from other tokamaks in Fig. 2.12.

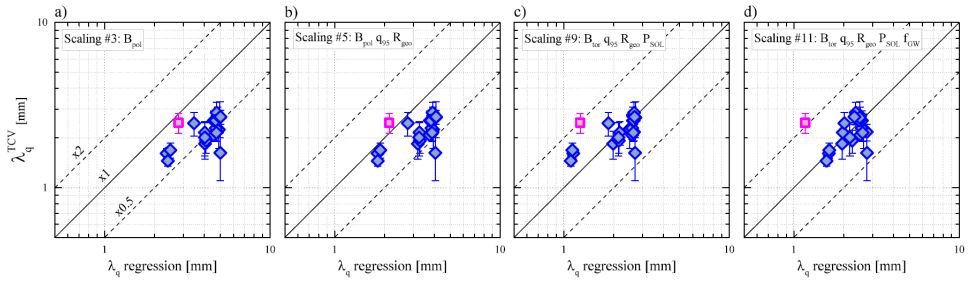

Fig. 2.11: Comparison of the results from Maurizio2021[28] on the TCV tokamak and several regressions from Eich2013[5]. Regressions #9 and #11, plots c) and d), show accordance with the TCV λ_q measurements, while the other two appear to overestimate the measured values.

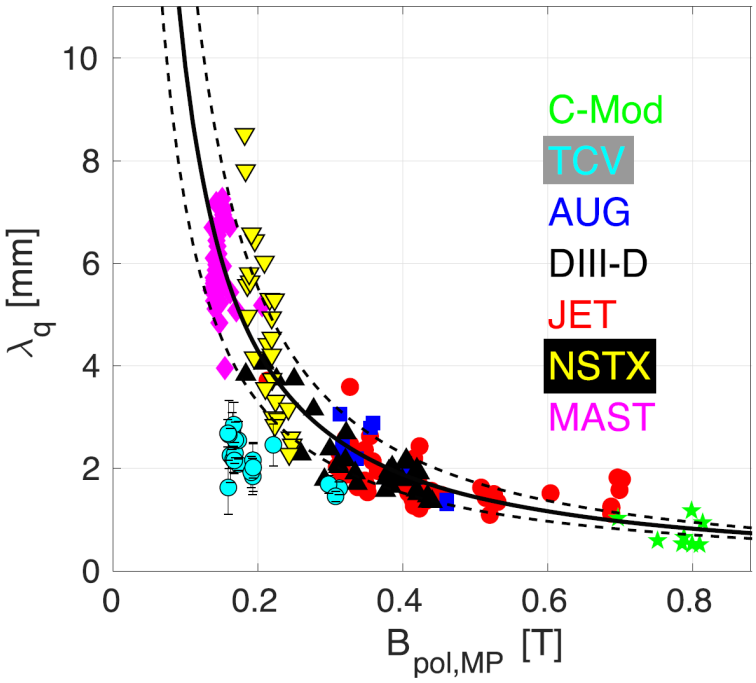

Fig. 2.12: Comparison of the results from Maurizio2021[28] on the TCV tokamak and the original multi-machine database, see Fig. 2.4. The TCV results exhibit significantly shorter decay lengths λ_q for given $B_{\mathrm{pol}} = B_\theta$ values.

Chapter 3

Diagnostics of the edge plasma in the COMPASS tokamak

This chapter provides an overview of the edge plasma diagnostic methods used in the thesis. The divertor probe array and the infrared camera are able to infer the properties of the downstream divertor region based on the interaction of plasma with the divertor targets. Thomson scattering, on the other hand, offers non-invasive measurements of the upstream SOL, which is directly adjacent to the main plasma. All three of these diagnostic methods are commonly used on the COMPASS tokamak as well as the majority of other tokamaks which are focused on the plasma edge research.

3.1 High resolution Thomson scattering

3.1.1 Description of the diagnostic system

Thomson scattering (TS) is a method of plasma diagnostics that is used to measure plasma profile of electron temperature T_e and density n_e. It is based on the interaction of short (1–10 ns) high-energy (1–10 J) laser pulse with a small local volume of free electrons and the subsequent analysis of the spectrum of scattered light. The intensity of the scattered light and the shape of its spectrum is determined by the density and temperature of electrons in the small volume. A vital assumption is that the electrons are in thermal equilibrium, which implies the Maxwell-Boltzmann distribution of velocity. Theoretical models of the scattered spectrum combine the theory of Thomson scattering cross section and the relativistic Doppler effect [32, 33]. The TS cross section states the dependency of scattered power on the laser-beam power and the electron density. The Doppler effect is caused by the thermal movement of electrons and it results in the widening and shift of the original quasi-line laser spectrum towards shorter wavelengths. The magnitude of the widening and shift is given by the local electron temperature.

The TS diagnostic system on the COMPASS tokamak[35, 34], see Fig. 3.1, utilizes 4 Nd:YAG lasers that operate at the wavelength of 1064 nm. The lasers use the Q-switching technology in order to generate 7 ns high-energy pulses with the repetition rate 30 Hz each, giving a total of 120 Hz. The laser

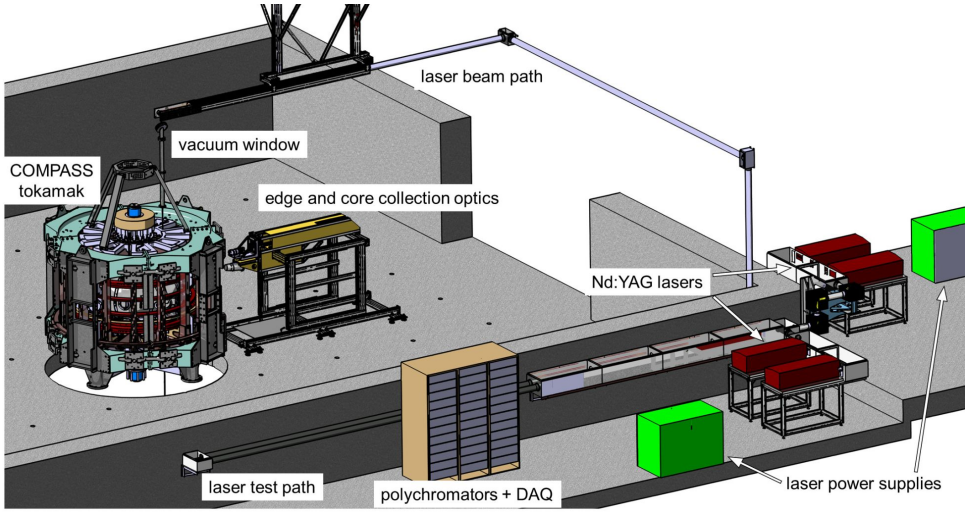

Fig. 3.1: Schematics of the TS diagnostic system on the COMPASS tokamak. The optical fibers, which connect the collection lenses and the polychromators, were omitted. [34].

beam is reflected using a series of mirrors above the tokamak vessel and it enters it through a port in the vertical direction. A small fraction of the beam energy is scattered and collected through a side port using a set of two collection lenses (core TS and edge TS, observing the corresponding regions of plasma), while the remaining portion is dissipated by an beam dump at the bottom of the vessel. The pair of collection lenses focuses light from small plasma volumes along the laser beam path onto a column of 54 optical fibre bundles, which define the 54 finitely sized "points" of the diagnostics' spatial axis. The core TS consists of 24 points offering a spatial resolution of 7–12 mm, while the edge TS has 30 points with higher resolution of 3.5 mm. Optical fibres transport the scattered light to polychromators, which utilize a cascade of 5 different spectral filters followed by avalanche photodiodes to sample the spectrum. Each polychromator outputs a 5-channel analog signal, which is converted to digital signal and numerically integrated in time. The T_e and n_e profiles are calculated from the integrated signal using an optimized theoretical model of TS spectrum and fitting algorithms[36].

3.1.2 Observed plasma region

The TS diagnostics on the COMPASS tokamak measures a T_e and n_e radial profile along the vertical axis Z in the upper area above the midplane. When mapped to the 1d poloidal magnetic flux coordinate ψ, the collection lenses cover approximately $\psi \in [0, 1.2]$, as seen in Fig. 3.2. The edge TS itself observes the periphery of the main plasma near the separatrix and the SOL region beyond it. In the context of the significant poloidal asymmetry introduced by the divertor configuration, it should be also mentioned that the observed SOL region is located far from both LFS and HFS divertor targets. Therefore, in this sense it represents an area that is to be least affected by

any effects localized to and induced by the divertor region. This is in contrast with the situation concerning the divertor diagnostics (i.e. the divertor probes and the infrared camera).

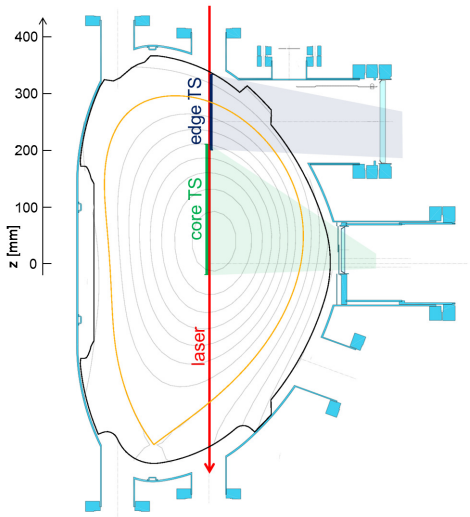

Fig. 3.2: A poloidal view of the TS laser beam paths inside the vaccum vessel and the coverage of collection optics. Laser beams travel down along the Z axis into the beam dump below the vessel. A full radial profile above the midplane is observed. [34]

3.1.3 Data availability

The TS diagnostic system has undergone a major upgrade of the edge TS section since its installation on the COMPASS tokamak[37]. For the purpose of this thesis only the data gathered after the upgrade was considered. The upgrade was finalized before discharge #15179 and it has been followed by approx. 6000 discharges until the most recent discharge #21316. The TS is one of the main plasma diagnostics and therefore there are measured TS profiles available for most of those discharges.

The first factor that limits the availability of TS data and that is relevant to the research of SOL in the inter-ELM phase is the temporal resolution. As a result of the combined laser repetition rate 120 Hz the time between TS measurements is longer than 8 ms, while the time between ELMs during H-mode is typically 2–4 ms. Whether a measurement occurs during the 1–2 ms-long inter-ELM phase or not is essentially a random event. Usually, there are 1 or 2 measurements per H-mode dischrage that meet these criteria.

The second limiting factor is the lower quality of older TS data due to stray-light. Starting with discharge #20366 an automatic stray-light correction procedure has been implemented mitigating the negative effects. In order to apply the correction to any of the previous discharges, each of them must be examined individually. In general, the results are also less reliable when compared to the automatic procedure.

3.2 Divertor array of Langmuir and ball-pen probes

3.2.1 Description of the diagnostic system

Langmuir probes (LP) represent a simple but effective method of plasma edge diagnostics with high temporal resolution, typically in the order of microseconds. A typical LP is a small electrode of a well-known shape and size that is exposed to the plasma. Particles from plasma start to interact with the probe and a potential sheath is formed near its surface. Without any voltage bias, the probe attracts electrons until it reaches the floating potential V_f, which is smaller than the plasma potential Φ. In this state the net current is zero. When a voltage is applied to the probe, the resulting current flowing onto the probe follows an I-V characteristic, which depends on the properties of plasma. A theoretical model of the I-V characteristic based on physics of Maxwellian plasma can be derived. The model can be then used to determine the electron temperature T_e and electron density n_e from a measured I-V characteristic of the probe. In addition to V_f and T_e, the LP can be used to measure the saturated ion current density $j_\mathrm{i}^\mathrm{sat}$ by applying a large negative voltage to the probe. [6, chapter 10]

Measuring the I-V characteristic requires the use of swept bias voltage, which effectively decreases the time resolution and may underestimate peak values. There are several alternative methods of measuring T_e that try to avoid this disadvantage, one of them being the ball-pen probe[38, 39]. The ball-pen probe (BPP) is a specialized probe consisting of a conductive collector placed in a tubular shielding. The design resembles a tip of ballpoint pen, thus the name. By retracting the collector inside the shielding, it is possible to affect the ratio of electron and ion saturated current ($I_\mathrm{e}^\mathrm{sat}$ and $I_\mathrm{i}^\mathrm{sat}$), because the particles impact the probe under a very small angle. The ions are affected less because of their large gyration radius $\sim 10\,\mathrm{mm}$, which is comparable to the retraction distance. The gyration radius of electrons is significantly smaller $\sim 10\,\mu\mathrm{m}$, but some of them are still able to reach the collector, possibly influenced by the $\vec{E} \times \vec{B}$ drift[40]. As a result, the electrons are at a disadvantage and the $I_\mathrm{e}^\mathrm{sat}$ decreases. The retraction distance is adjusted so that the ratio of currents $\mathfrak{R} = I_\mathrm{e}^\mathrm{sat}/I_\mathrm{i}^\mathrm{sat}$ approaches unity $\mathfrak{R} \approx 1$. According to the theory of Langmuir probes, when $\mathfrak{R} = 1$ the potential on the probe (BPP) is equal to the plasma potential Φ. By combining the BPP with a normal LP that measures the floating potential V_f it is possible to measure the electron temperature T_e with high temporal resolution. The T_e is then calculated using the following formula[38]

$$T_\mathrm{e} = \frac{\Phi - V_\mathrm{f}}{\alpha}, \tag{3.1}$$

where α is a combined coefficient related to both the LP and BPP and the type of plasma. On the COMPASS tokamak, $\alpha \approx 1.4$ for deuterium plasma.

The divertor diagnostic system on the COMPASS tokamak includes an

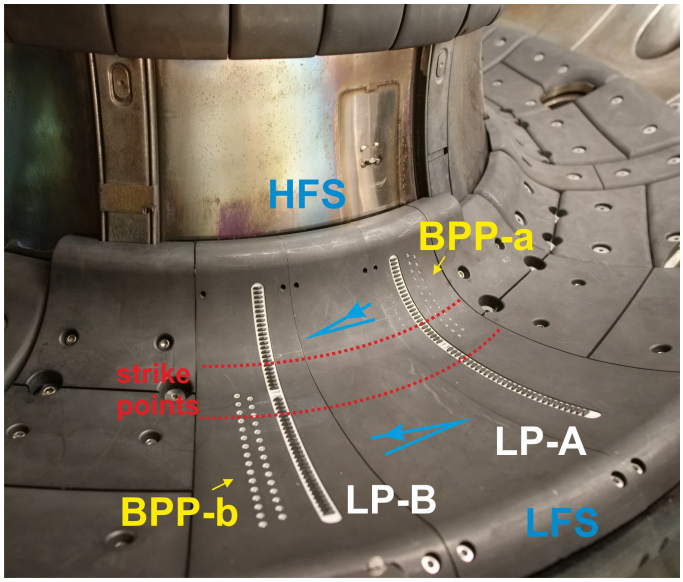

Fig. 3.3: Photo of the divertor probe array in the COMPASS tokamak. The array consists of two sets of Langmuir probes (LP-A, LP-B) and one set of ball-pen probes (BPP). The BPPs are split into two sections and positioned in such way that they are not shadowed by the LPs. The blue lines indicate the usual direction of the field lines and their angle of incidence. [41]

array of 2×55 LPs and 55 BPPs. The probes are installed in parallel rows along the poloidal direction on the surface of divertor tiles. The setup is visible in Fig. 3.3. Pairs of BPPs and LPs from the first set are used for T_e profile measurements. LPs from the second set use $-270\,\mathrm{V}$ bias voltage to measure the profile of saturated ion current density j_i^{sat}. All probe signals are sampled at 4 MHz resulting in $< 1\,\mu\mathrm{s}$ temporal resolution. The spatial resolution is determined by the spacing between probes, which is 3.5 mm.

An agreement with the IR camera $q_{\parallel}$ measurements is demonstrated in section 3.3, see the graph in Fig. 3.4.

3.2.2 Observed plasma region

The divertor probe array on the COMPASS tokamak covers both HFS and LFS areas of the divertor target. However, there are ongoing discussions about the HFS section of the array and the reliability of its measurements. Therefore only data from the LFS section are used in this thesis.

The array observes the properties of the divertor region and the private flux region near the surface of divertor tiles. As illustrated in Fig. 3.3 the LFS strikepoint, which separates the two regions, is often located very close to the end of the LFS section of probes. Because of that, the majority of probes observe the divertor region and only a few of them (typically 2–3) observe the private flux region.

3.2.3 Data availability

The array was installed on the tokamak 4 years ago and first measurements were acquired in discharge #12343. Similar to the TS diagnostics, the array is also kept operational by default and collects data during most of the discharges. In total, approx. 9000 discharges between #12343 and the most recent discharge #21316 offer data measured by the divertor probe array.

In the context of individual probes, it is not uncommon to encounter faulty measurement from one or two probes in the array. When discarding the faulty data point it is often possible to avoid any major impact on the measured profile. However, the absence of a data point may significantly affect the uncertainty of the profile, when the point for example resides in the private flux region, where the profile gradients are high.

3.2.4 Calculating particle heat flux

As was mentioned above, the probe array on the COMPASS tokamak is able to measure radial profiles of saturated ion current density $j_\mathrm{i}^\mathrm{sat}(s)$, plasma potential $\Phi(s)$ and electron temperature $T_\mathrm{e}(s)$, where the coordinate s represents a spatial coordinate along the surface of LFS divertor target.

Charged particles, which escape the confined plasma, travel through the SOL and eventually impact the divertor target inducing a heat flux. In the context of the SOL plasma theory it is useful consider a parallel[1] projection of the heat flux $q_\parallel$. It can be estimated as

$$q_\parallel(s) = \gamma \cdot T_\mathrm{e}(s) \cdot j_\mathrm{i}^\mathrm{sat}(s) = \gamma \cdot T_\mathrm{e}(s) \cdot \frac{I_\mathrm{i}^\mathrm{sat}(s)}{A_\mathrm{LP}}, \tag{3.2}$$

where $A_\mathrm{LP} = 2.8 \times 10^{-6}\,\mathrm{m}^2$ is the effective probe surface area perpendicular to the field lines and γ is the sheath heat transmission factor. Calculating an accurate γ factor is often problematic. An estimate of $\gamma = 11$ is used for the COMPASS tokamak, which is based on a surprisingly good agreement between empirical measurements from the IR camera [42, 31] and a theoretical prediction in locally non-ambipolar conditions based on equations from [43, 7]. It should be noted that γ does not have any effect on the decay length λ_q measurements, although it is important for the power balance calculations.

By integrating the heat flux along the surface of the divertor target it is possible to calculate the total thermal power P_div generated by impacting particles

$$P_\mathrm{div} = \int_\mathrm{div} q_\perp(s)\mathrm{d}\phi\mathrm{d}s = 2\pi R \int_\mathrm{div} q_\perp(s)\mathrm{d}s. \tag{3.3}$$

In this context, a projection of the heat flux perpendicular to the surface $q_\perp$ has to be used instead of the parallel projection $q_\parallel$. A relation between these projections is given by the impact angle β between the magnetic field lines and the surface

$$q_\perp = q_\parallel \sin(\beta). \tag{3.4}$$

[1] Parallel to the magnetic field lines.

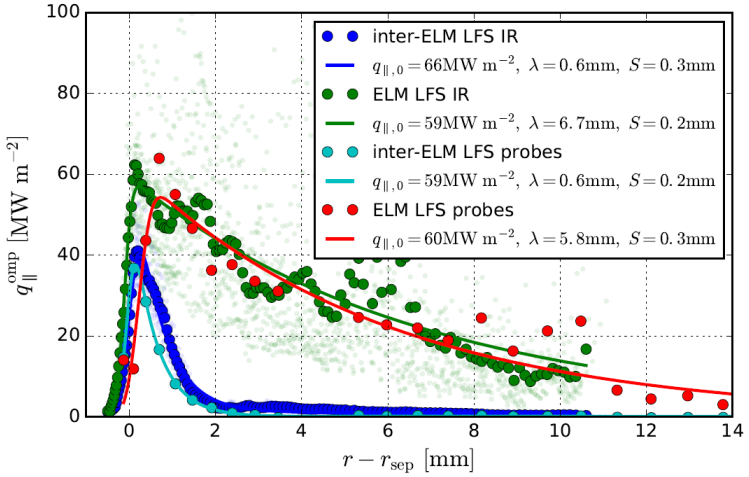

Fig. 3.4: A comparison of radial divertor heat flux $q_{\parallel}$ profiles in the COMPASS tokamak during H-mode measured using the fast IR camera and the LFS section of divertor probe array. Both diagnostics are in a good agreeement. [44]

3.3 Fast infrared camera

3.3.1 Description of the diagnostic system

Infrared (IR) thermography is a primary method of measuring surface temperature of plasma facing components including the divertor target. Furthermore, the temperature profile can be used to estimate the local heat flux of incoming plasma. The method is based on detection of thermal radiation from solid surface. An ideal solid surface can be described by the theory of black-body radiation, i.e. by the Planck's law and Stefan-Boltzmann's law. In practice, the reflective properties of the surface and influence of the detection optics has to be considered as well. Additional complications are often introduced in the form of background radiation from plasma and mechanical vibrations of the tokamak. [44]

The COMPASS tokamak is equipped with a high resolution divertor IR system, which was commissioned in 2018 and features a fast IR camera[42]. It observes an area of approx. 190 mm × 152 mm of the divertor target from a vertical port at the top of the vacuum vessel. The frame rate of the camera is 1.9 kHz in full frame mode (320 × 256 px), which can be increased up to 50 kHz with the use of subwindowing (320 × 4 px). This translates to a temporal resolution of 20 µs.

Graph in Fig. 3.4 shows an example of heat flux $q_{\parallel}$ measurements during H-mode using both the IR camera and the divertor probe array, which is described in section 3.2. The camera and the probes are in good agreement.

3.3.2 Data availability

The data processing is more complicated than in the case of the TS diagnostics or the probe array and often requires manual intervention. As a result of that, is is used selectively and the availability of heat flux measurements from the FIR camera is limited. In the context of the power decay length database, which is described in chapter 4, only a small fraction of discharges offered processed data from FIR camera. The available data was used primarily for reference and comparison as it was insufficient for any detailed analysis.

Chapter 4

Collecting the power decay length database

This chapter describes the data collection. First section presents the method, how the prospective H-mode discharges were filtered from the COMPASS database and what criteria were used. Following two sections are focused on the calculation of decay lengths in downstream and upstream plasma.

4.1 Selecting H-mode discharges

In order to characterize inter-ELM power decay lengths and their scaling, a sufficiently large and diverse database of prospective ELMy H-mode discharges needs to be collected. Because the criteria, listed in subsection 4.1.2, are quite restrictive, a large portion of COMPASS database had to be analyzed. Both algorithmic pre-selection and final manual selection was employed. The complete process is described in detail in this section.

4.1.1 Overview of the COMPASS discharge database

As of the year 2021, the database of COMPASS tokamak contains over 21,000 discharges. Only the more recent campaigns, years 2017–2021, discharges #15179–#21316, were considered. #15179 is the first discharge after the last upgrade of Thomson scattering (TS) diagnostics, which added new port window and new lenses[34].

The discharges were separated into two groups #15179–#20365 and #20366–#21316. It reflects the introduction of the automatic TS stray-light correction system, which improves the quality of measured data. Discharges before #20366 had to be corrected one at a time by hand, which is a less reliable process and it is often unable to provide satisfactory results. However, it was discovered that including the older group has the benefit of increased parameter space for B_θ and other important scaling parameters. Examples of the difference in the variability of the parameters can be seen in Fig. 4.1 and Fig. 4.2.

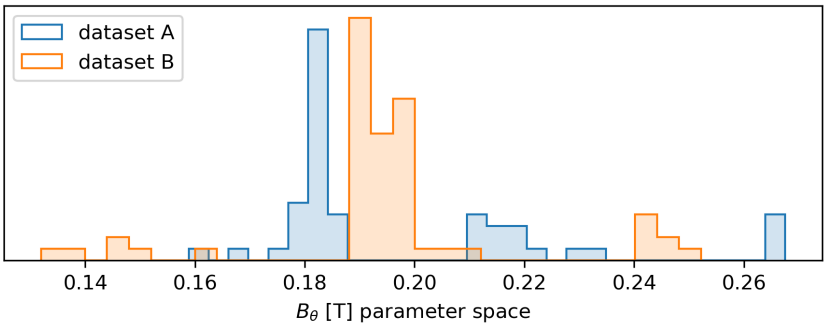

Fig. 4.1: Comparison of available parameter space of the poloidal magnetic field B_θ in discharge datasets A and B.

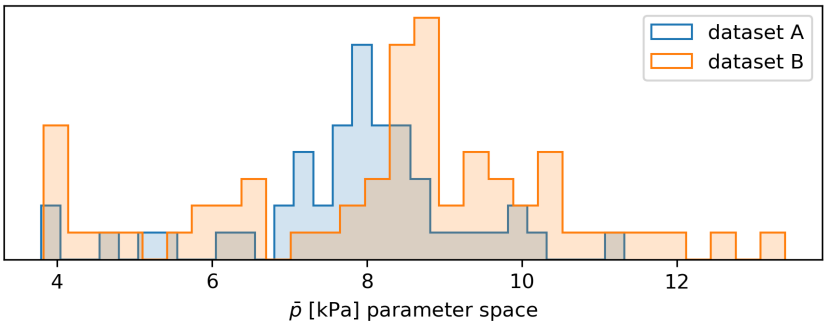

Fig. 4.2: Comparison of available parameter space of the line mean core plasma pressure $\bar{p}$ in discharge datasets A and B.

4.1.2 Criteria

The discharges were selected according to following criteria:

(i) Data from both TS and divertor probe array is available.

(ii) Discharge contains ELMy H-mode phase.

(iii) At least one TS record 'happens' to hit a specific phase of an ELM cycle, 70–85 %. It has to occur during the flat-top phase of plasma current.

(iv) Current was not applied to RMP coils.

(v) No non-hydrogen gas is injected (i.e. seeding experiments).

The first condition (i) is straightforward. Sometimes the diagnostics may be turned off or for example the data acquisition systems may fail. While TS and divertor probes are used regularly, the fast infrared camera was effectively disqualified, because it is not available that often, especially for H-mode discharges.

An automated system that recognizes ELMy H-mode discharges from H_α signal is implemented on the COMPASS tokamak and can be used to validate

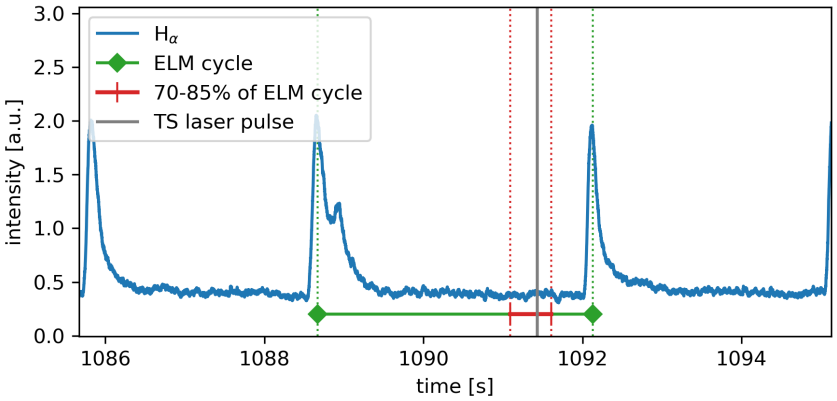

Fig. 4.3: Signal of H_α (D_α) radiation in the COMPASS tokamak in ELMy H-mode plasma. Peaks correlate with the ELM events and ejection of mass from the confined plasma. A single ELM cycle is marked with a green line and the quasi-stationary phase, which was used for the λ_q measurements, is marked with a red line.

the second criterion (ii). The system occasionally produces false positive results, so the results should be double-checked manually.

One of the main topic of this thesis is the comparison of upstream and downstream measurements. That requires a synchronized record of TS and divertor probes. While data from probes is gathered continuously with high sampling frequency $\sim 1\,\mathrm{MHz}$, TS records are sampled at 120 Hz, which is smaller than typical ELM frequency $\sim 1\,\mathrm{kHz}$. Thus the main task is to find a TS record that happened to correlate with a given phase of ELM cycle, criterion (iii). Typically, a second half or last third of the cycle is used, see section 1.1.3 and reports [5], [29]. In this case, a more restrictive phase 70–85 % was selected to ensure quality of data by increasing the margin from the rising slope of H_α peaks, see Fig. 4.3.

Finally, two other criteria, (iv) and (v), that address invasive plasma edge research were added. Resonant magnetic perturbation (RMP) is an experimental method of actively controlling and influencing the ELMs, which could have influence on the divertor heat flux footprint. Seeding experiments attempt to directly influence the SOL regime, see section 1.3.4, by injecting e.g. nitrogen gas into the divertor area.

4.1.3 Automatized pre-selection

During the first phase of discharge selection a convenient automatized script was created to crawl through the COMPASS database, discharges #15179–#21316, and generate a preliminary selection based on criteria (i) and (ii). Additionally, all runaway electron campaigns were discarded, which significantly reduced the ratio of false positive H-mode detection. A total of 1660 discharges was selected.

Next, the ELM cycle criterion was enforced. The automatic H-mode

detection system on the COMPASS tokamak also detects individual ELMs as peaks in H_α signal and estimates the time of a maximum in each peak. The time interval from peak to peak is regarded as the ELM cycle. An algorithm that calculates whether any TS record in a discharge fulfills the criterion (iii) was implemented. The algorithm also discards cycles, whose length deviates more than 50 % from a mean ELM period in that discharge, to eliminate false positives and irregular edge cases near the start and end of the H-mode phase. Once again the crawler script was used to apply the algorithm and narrow down the selection to 925 discharges.

The RMP current signal and valve control signals were used in a similar manner to filter out discharges according to criteria (iv) and (v). Together the algorithms isolated a total of 640 prospective discharges ready for manual inspection.

4.1.4 Manual selection

As a follow-up to the automatized selection, a manual check was conducted. The goal was to discard the remaining falsely recognized H-mode discharges and any obvious outliers. The final product was a selection of the specific TS records that had been sampled from a stable ELMy H-mode phase during a flat-top phase of plasma current, which were ready to be used for the inter-ELM decay length analysis.

While 640 discharges is not a completely unreasonable number for a one-time manual breakdown, a certain amount of optimization was introduced. Firstly, a simple visualization app that is able to conveniently iterate through relevant data about the discharges and ELMs was created. Secondly, as discussed before, the discharges had to be separated into two groups based on the method of TS stray-light correction. The group of more recent discharges with better correction method, denoted as the *dataset A*, was reasonably small (76 disch.). It was analyzed in full, leaving a final set of 35 discharges, 49 inter-ELM TS records.

Since the other group was both significantly larger and was expected to contain lower quality data, it was processed only selectively. A smaller subset was assembled with the intention to extend the total variability of discharge parameters, mainly the poloidal field B_θ. Sufficient parameter variability is necessary for the scaling analysis of decay lengths. After conducting the manual data checking and manual TS stray-light corrections, the result was the *dataset B* of 40 discharges, 62 inter-ELM TS records.

4.1.5 Summary

Table Tab. 4.1 provides a brief summary and comparison of the two collected datasets. When combined the whole database provides a total of 141 inter-ELM records (timestamps of TS measurements) that can be used for heat flux decay length analysis in both upstream and downstream SOL. Note that, on average, only 1–2 records were found in each discharge, which may prove to be limiting in some aspects. For example, in [29] the upstream decay lengths are

calculated from several inter-ELM TS profiles measured in a single discharge grouped together, which may decrease error of the estimation. However, the low number of records per discharge eliminates that approach.

As mentioned above, the extended dataset B improves and extends the parameter space of the main dataset A. A comparison in coverage of poloidal magnetic field B_θ is shown in histogram in Fig. 4.1.

dataset	discharge range	dischrg.	records	B_θ [T]
A (main)	#20366–#21316	35	49	0.15–0.19
B (extended)	#15179–#20365	40	62	A∪B: 0.13–0.26

Tab. 4.1: An overview of the two collected datasets of H-mode discharges. The 'records' column refers to the total number of actual inter-ELM TS records (profiles) in the dataset. The last column summarizes the coverage of the poloidal magnetic field parameter B_θ, see Fig. 4.1.

4.2 Downstream decay length

The downstream heat flux decay length λ_q was estimated from the divertor probe array, which is described in chapter 3. The array consists of ball-pen probes (BPP) and Langmuir probes (LP). It is able to measure spatial profile of divertor heat flux $q_\parallel(s)$. Although the array spans over both LFS and HFS targets, the HFS section of array is known to produce less reliable results, thus, only LFS measurements were utilized.

4.2.1 Divertor heat flux profile

The parallel heat flux profile $q_\parallel(s)$ was calculated using equation (3.2) from the data measured by the divertor probe array, that is the electron temperature $T_\mathrm{e}(s)$ and the saturated ion current density $j_\mathrm{i}^\mathrm{sat}(s)$. The coordinate s is a spatial coordinate along the surface of LFS divertor target.

Unlike the Thomson scattering, data measured by probes has high sampling frequency and therefore the time dimension needs to be considered. An arithmetic mean was calculated over the 70–85 % ELM cycle interval, i.e. the quasi-stationary phase, to estimate T_e and $j_\mathrm{i}^\mathrm{sat}$ at the time of given inter-ELM interval. The standard deviation was used as an estimate of uncertainty. The heat flux was then calculated using these averaged values.

Equation (3.2) also includes the sheath heat transmission factor γ. This factor is not important in the context of decay length λ_q estimation, because it only affects the absolute value of $q_\parallel$. Originally, value $\gamma = 11$ was selected, which is an empirical estimate based on data from infrared camera in L-mode discharges[31]. Different estimations are discussed in relation to the power balance calculations in section 5.5.

4.2.2 Fitting the heat flux profile

In the COMPASS tokamak, the magnetic flux expansion factor f_x varies significantly along the divertor target, see Fig. 2.3. Therefore, the divertor heat flux $q = q(s)$ was mapped to outer midplane $q = q(R_{mp})$ via EFIT. The heat flux profile was then characterized by a best fit of the Eich model (2.3) (coordinate $\bar{s} \mapsto \bar{R}_{mp} = R_{mp} - R_{mp}^{sep}$). Decay length λ_q was estimated as a parameter of the fit, together with the power spreading parameter S, peak heat flux q_0 and position of separatrix (strike point) R_{mp}^{sep}. As an alternative, the profiles were also fitted using the simple exponential model (2.2), which includes only the decay length λ_q and peak heat flux q_0. The R_{mp}^{sep} position, which is required to calculate the $\bar{R}_{mp}$ coordinate, was derived from EFIT in this case. The results of the two models are compared in section 5.1.

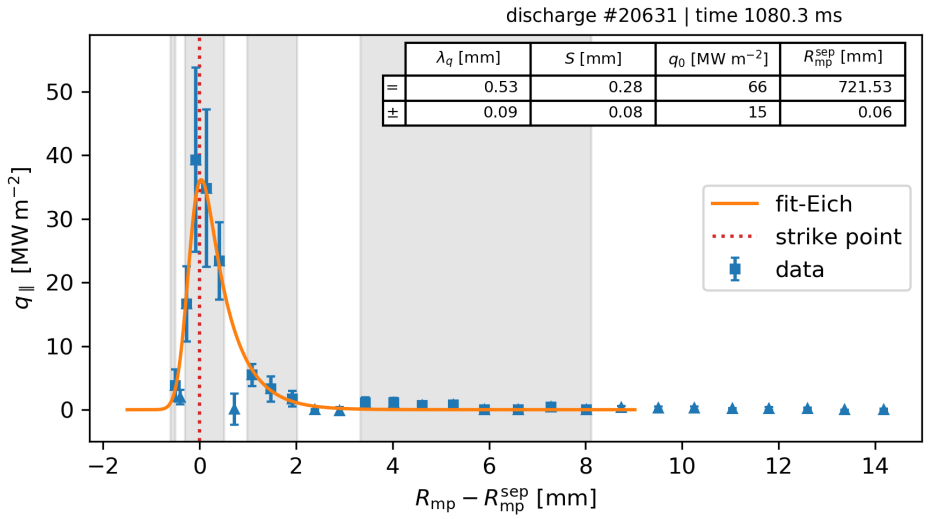

Fig. 4.4: Example of heat flux q measured by LFS divertor probes and mapped to outer midplane. Fit using the Eich function (2.3), gray areas highlight selected points. Far points ($\psi_n > 1.08$) and faulty points (here: 4 points near the strike point) were discarded. The red dotted line is the EFIT estimate of strike point position, shown for reference.

Example of a q profile fitted using the Eich model is in Fig. 4.4. It illustrates several common issues that were encountered during fitting. First is the fact that the strike point was located very close to the edge of LFS probe array, which resulted in a small number of points, typically 1–3, in the private plasma region. In some instances there were none at all, which significantly reduced the stability of the fit. Occasionally, some data points had to be discarded because of a probe fault.

Second topic for discussion are the errorbars, which were estimated as a standard deviation in the time window. Although they may present a reasonable estimate for the points near the strike point, where the heat flux is large, the estimates become very small in the tail increasing the influence

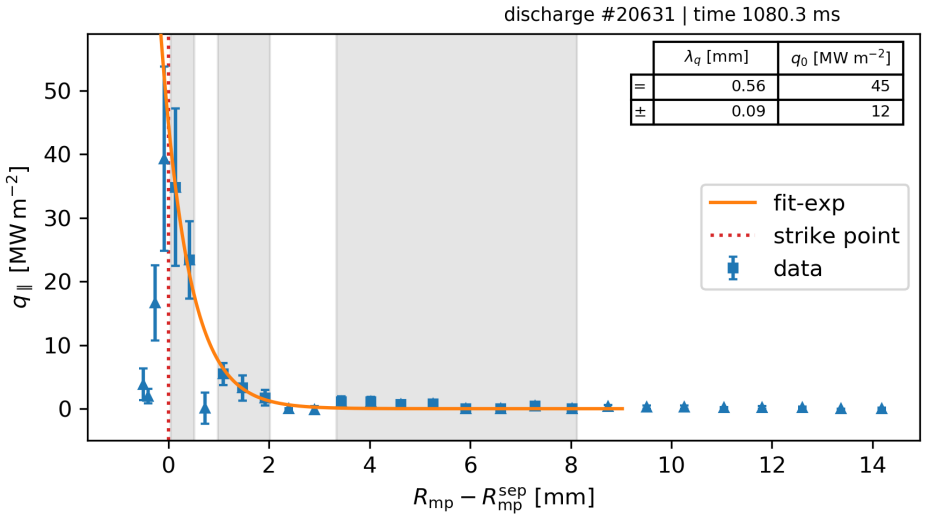

Fig. 4.5: Alternative fit of divertor probes data from Fig. 4.4. All points in private flux were discarded and simple exponential model (2.2) was used. The strike point position R_{mp}^{sep} was estimated from EFIT.

of tail points on the results. To test this, new fit of profiles without errorbars was re-calculated, but the difference in results proved to be neither significant nor systematic.

A third observation is a small anomaly in the profile (local maximum), which sometimes appeared in the tail. A hint of this phenomenon can be seen in Fig. 4.4 near $R_{mp} - R_{mp}^{sep} = 6.2\,\text{mm}$ for example, although it not very pronounced here. Its source and the effects on λ_q are discussed later on in the section 6.1.

Example of a fit using the simple exponential model is in Fig. 4.5. All data in the private flux region was discarded. Although in this case the fits are similar, note that often this second approach was more stable and the uncertainty of parameters was smaller. Comparison of the results from first and second approach is analyzed in more detail in section 5.1.

4.3 Upstream decay lengths

The upstream decay lengths, λ_{T_e} and λ_{n_e}, were estimated from electron temperature and density profiles in the pedestal area measured by the Thomson scattering (TS) diagnostics, which is described in chapter 3.

4.3.1 TS upstream profiles

An example of temperature T_e and density n_e profile measured by TS is in Fig. 4.6. The radial profiles are measured along the vertical coordinate Z above the midplane, as previously illustrated in Fig. 3.2. Results of EFIT

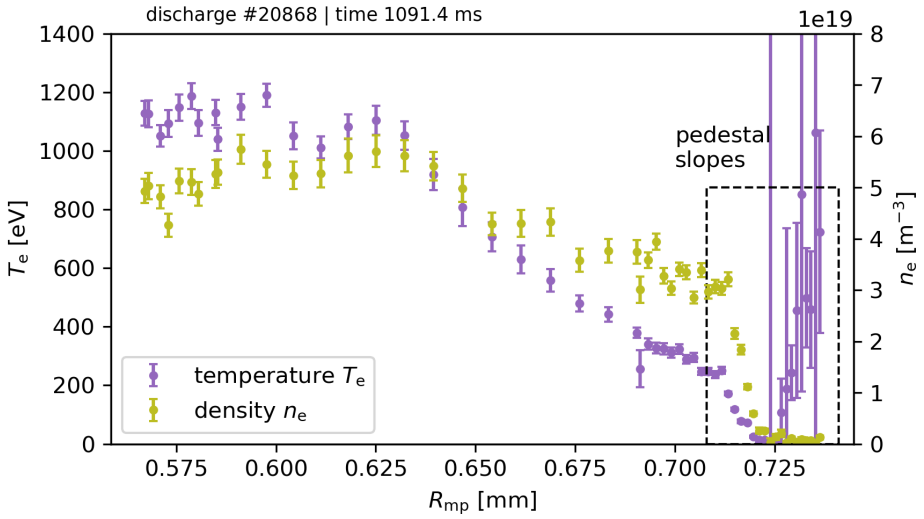

Fig. 4.6: Example of TS profiles of electron temperature and density measured during an inter-ELM interval. The dashed rectangle marks the area of interest, the pedestal slope, relevant for the estimation of the decay length.

equilibrium reconstruction were utilized to map the profiles to outer midplane R_{mp} using [8, 45].

The area of interest in Fig. 4.6 is the temperature and density pedestal slope, which are located near the separatrix and outlined by the dashed lines. The slope describes the upstream SOL profile and it can be characterized by the temperature λ_{T_e} and density λ_{n_e} decay lengths.

As a side note, it is worth to mention that according to the EFIT results on the COMPASS tokamak the pedestal slope often seems to be fully outside of the separatrix, as seen for example in Fig. 4.7. A more typical behavior observed on other tokamaks, e.g. TCV [28], is for the slope to be partially inside of the separatrix. The precision of EFIT equilibrium reconstruction is a problematic topic and a systematic error in position of the separatrix is not out of the question [25]. Therefore, the magnitude of any upstream SOL temperature and density profile measurements based on the EFIT separatrix may be systematically overestimated.

4.3.2 Fitting the TS profiles

The upstream decay lengths were estimated from temperature and density pedestal slopes as a best fit of an exponential function. Model for the temperature

$$T_e(R_{\mathrm{mp}}) = T_{\mathrm{e}}^{\mathrm{sep}} \exp\left(-\frac{R_{\mathrm{mp}} - R_{\mathrm{mp}}^{\mathrm{sep}}}{\lambda_{T_e}}\right) \tag{4.1}$$

and analogously model for the density

$$n_e(R_{\mathrm{mp}}) = n_{\mathrm{e}}^{\mathrm{sep}} \exp\left(-\frac{R_{\mathrm{mp}} - R_{\mathrm{mp}}^{\mathrm{sep}}}{\lambda_{n_e}}\right). \tag{4.2}$$

Here $R_{\mathrm{mp}}^{\mathrm{sep}}$ is a fixed position of separatrix as calculated by EFIT. The quantities λ_{T_e}, $T_\mathrm{e}^{\mathrm{sep}}$ and λ_{n_e}, $n_\mathrm{e}^{\mathrm{sep}}$ are the parameters of the fit.

In order to estimate the decay length, the pedestal slope had to be extracted from the full profile. The position of the pedestal strongly correlates with the position of separatrix, and therefore the normalized coordinate ψ_n can be used to extract the appropriate section of the profile. A threshold of $\psi_\mathrm{n} > 1.0$ was applied to select the points. Occasionally, the selection was adjusted manually by adding or removing 1–2 points near the threshold in order to correctly capture the top end of the slope. An example of the fit results can be seen in Fig. 4.7 and Fig. 4.8.

Initially, the pedestal slope data points were extracted including the far tail. This is not ideal because TS quickly loses precision at very low plasma density (low signal-to-noise ratio), as seen in the temperature example in Fig. 4.7 at 10–25 mm. The issue could be arguably more pronounced in the density profiles, Fig. 4.8, where the errorbars of the tail points are often underestimated allowing them to influence the results. Based on these concerns, a second version was computed with a more conservative selection, which discards all points beyond $\psi_\mathrm{n} > 1.1$. However, this approach reduced the selection to only 6 points per profile on average and mainly increased the stochastic variance of results. A very small systematic decrease of $\sim 10\,\%$ in λ_q and increase of $\sim 10\,\%$ in $T_\mathrm{e}^{\mathrm{sep}}$, $n_\mathrm{e}^{\mathrm{sep}}$ was observed. It was decided that the original approach, which includes more data points and does not arbitrarily discard potentially useful data, is sufficient.

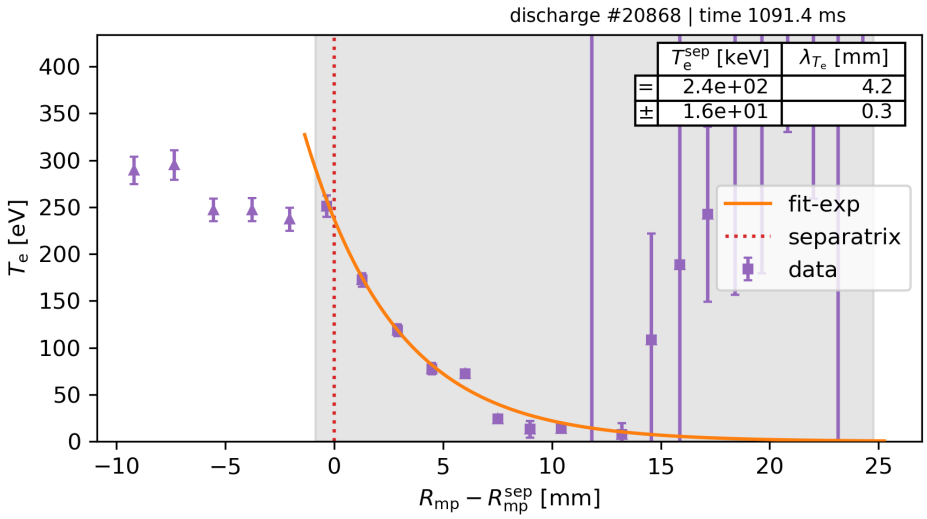

Fig. 4.7: Example of a fit of upstream T_e profile, pedestal slope, using (4.1). Profile was measured by the TS diagnostics. The precision of tail points in range 10–25 mm is affected by low density and thus signal-to-noise ratio, see Fig. 4.8.

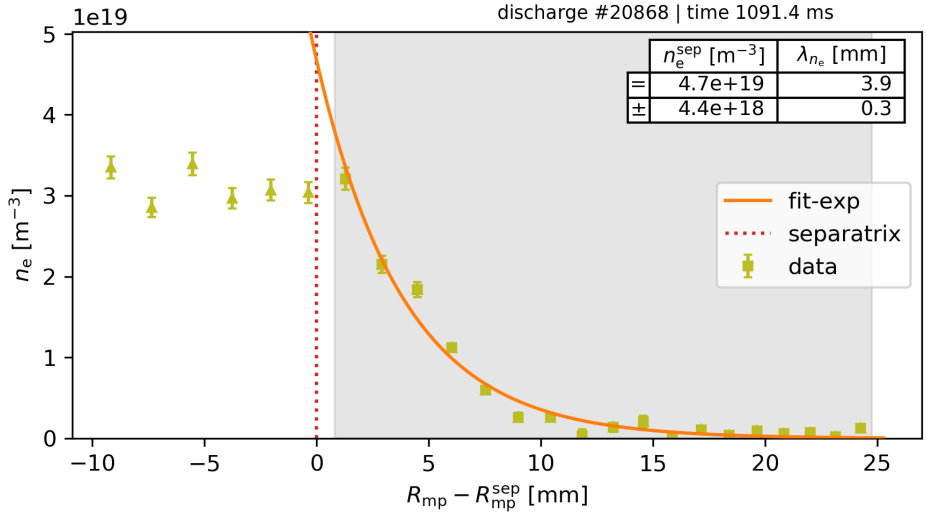

Fig. 4.8: Example of a fit of upstream n_e profile, pedestal slope, using (4.1). Profile was measured by the TS diagnostics. The errorbars of the tail points in range 10–25 mm are underestimated and do not correctly reflect the presence of noise and stray-light. However, the main section of the slope 0–10 mm consists of only 6 points, which do not seem to be sufficient to credibly define the exponential curve without the tail points.

Chapter 5

Analysis of results

This chapter describes the analysis of the COMPASS H-mode inter-ELM power decay length λ_q database gathered in chapter 4. The quality of the fits and uncertainty of the results is discussed. The relations between the upstream decay lengths and the downstream measurements, which were introduced in section 2.1.3, are examined. Similarly, the λ_q database is compared with the recently published models for downstream power decay length scaling, see chapter 2. The last section is dedicated to power balance calculations.

5.1 Downstream data

The downstream power decay lengths λ_q were estimated using data from the divertor probes. For this purpose, two different models were considered, the Eich model (2.3) (parameters λ_q, q_0, S, R_{sep}) and the simple exponential model (2.2) (parameters λ_q, q_0). Example of a fitted $q_{\parallel}$ profile is shown in Fig. 4.4 and Fig. 4.5. Comparison of the two models based on the uncertainty of the optimized parameters is shown in Fig. 5.1. The large uncertainty of q_0, S and R_{sep} in the case of the Eich model indicates that the fit of this model was often unstable and did not converge well. A possible cause is the deficiency of data points in the private flux area, as mentioned in section 4.2. Another cause may be the gaussian width parameter S, which was usually very narrow and thus had a minimal effect on the profile, or a correlation between R_{sep} and other parameters.

The main feature of the Eich model (2.3) is the introduction of the width parameter S, which accounts for dispersion of the SOL profile in the downstream region. Considering only results where the relative error of S was below 100 %, the absolute values of S were within the range 0.15–0.25 mm and the ratio S/λ_q was between 0.3–0.6. The absolute values are smaller than the resolution of probe array ~ 0.35 mm projected to outer midplane and the ratio is small $S/\lambda_q < 1$. Both of these facts imply that the effects of SOL profile dispersion were not significant and the simple exponential model may be sufficient.

Further comparison of the models is shown in Fig. 5.2. The figure shows a histogram of relative differences $\frac{exp-Eich}{Eich}$ between the estimated λ_q parameters

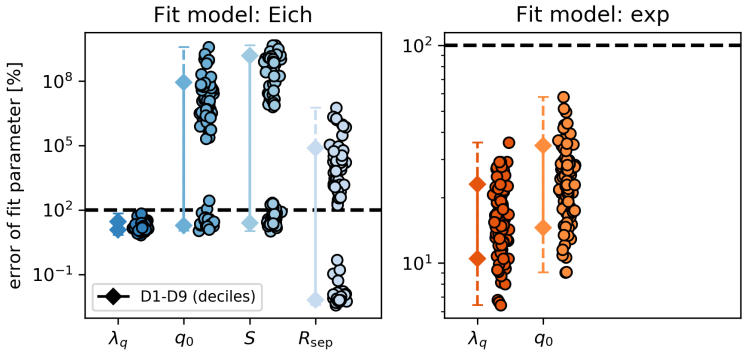

Fig. 5.1: Uncertainty of the downstream fit results, both datasets A+B. The Eich model (2.3) (left side) and the exponential model (2.2) (right side) are compared based on the relative errors of the fit parameters. The former shows significant instability of the fit (except for λ_q), while the latter appears to produce more reliable results.

and q_0 parameters. Differences of λ_q show only a limited systematic increase of 5–10 % and in general the difference does not exceed far beyond ±20 %. Contrary to that, the q_0 parameter is systematically 20–60 % smaller when calculated using the exponential model.

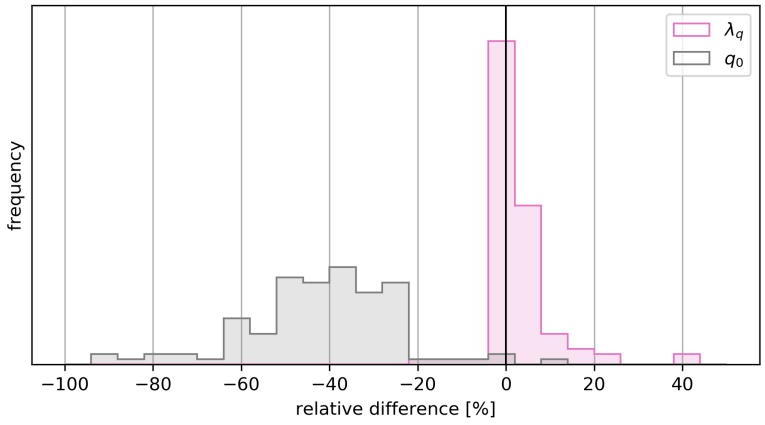

Fig. 5.2: Relative difference of parameters when estimated using the Eich model and the exponential model, $\frac{exp-Eich}{Eich}$. The graph shows combined results from datasets A+B. The differences in the estimation of the decay length parameter λ_q are limited $\sim 10\,\%$.

The reduced chi-square statistic, see appendix B, was calculated for results of both models and a summary is shown in Fig. 5.4. In both cases the results seem to be close to the ideal value of $\chi^2_\nu = 1$, although both models display an increased variance.

In conclusion, the exponential model was more stable and it had potential to produce more reliable results. The magnitude of the S parameter indicated that the widening of the SOL profile, which is addressed by the Eich model,

was relatively small. According to Fig. 5.2, the differences between the models in the context of λ_q were not systematic and did not exceed $\pm 20\,\%$. Based on these arguments it was decided to use the results of the exponential model rather than the Eich model for the purpose of this research.

5.2 Upstream data

The upstream decay lengths λ_{T_e} and λ_{n_e} were calculated using the exponential models (4.1) and (4.2), respectively. The uncertainty of fit parameters λ_q, $T_\mathrm{e}^\mathrm{sep}$ ($n_\mathrm{e}^\mathrm{sep}$) is summarized in Fig. 5.3. Both the temperature and density fits produced results with reasonable uncertainty estimations 5–20 %, which indicates a good stability of the method.

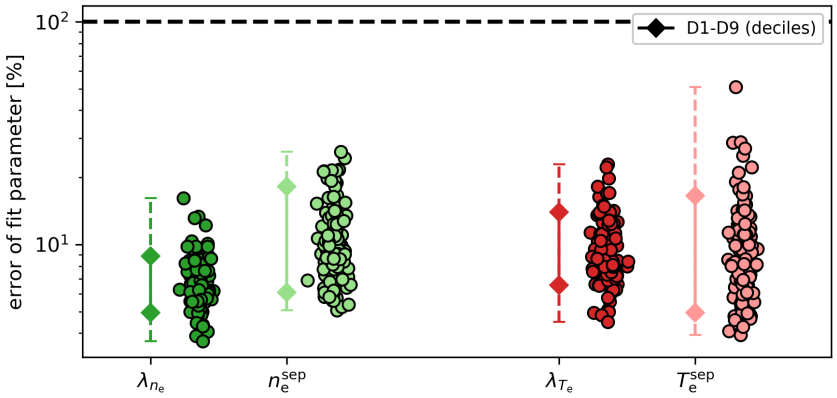

Fig. 5.3: Uncertainty of fit parameters in the upstream results, both datasets A+B. The estimated relative errors of the parameters appear to be reasonably small 5–20 % and do not indicate any significant instability of the fit model.

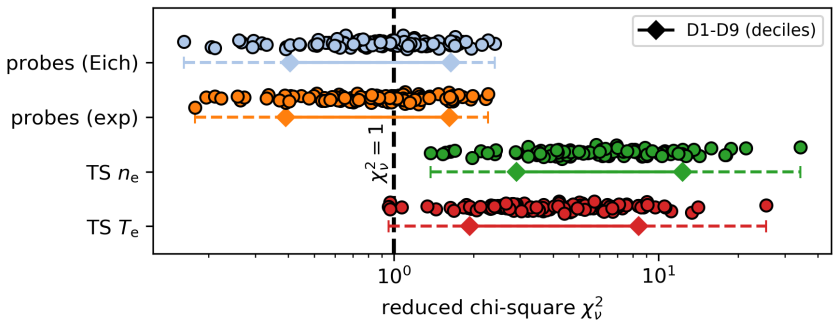

Fig. 5.4: Overview of χ^2_ν statistic, which characterizes the goodness of the fit. Both downstream models (Eich, exponential) are close to $\chi^2_\nu \approx 1$ indicating a good capture of the data. The upstream decay lengths show $\chi^2_\nu > 1$, which indicates that the model does not capture the data well in respect to the error of the observed TS data.

However, based on the discussion about insufficient spatial resolution in section 4.3, it can be argued that the uncertainty of results is underestimated. This fact is supported by the reduced chi-square statistic of fit results shown in Fig. 5.4. Both temperature T_e and density n_e results have χ^2_ν significantly larger than 1, which indicates that the fit did not fully capture the observed data in respect to the measurement errors. In this case, the fault does not seem to be connected to the model but rather to the occasional small-scale artifacts (probably due to residual stray-light) in combination with underestimated errors. See appendix B for more details about the χ^2_ν statistic.

5.3 Relation between upstream and downstream

According to [22], the upstream temperature and density decay lengths can be related to the downstream power decay length λ_q. The exact relationship depends on the transport regime which is dominating the SOL plasma. To determine the regime experimentally, the electron collisionality $\nu^*_{\text{e-SOL}}$ can be used, see equation (2.8). Below are listed the two cases, which were presented previously in section 2.1.3.

- Model (2.6), *conduction-limited* regime, strong collisionality $\nu^*_{\text{e-SOL}} \gtrsim 50$

$$\lambda_q^{\text{SH}} \approx \frac{2}{7}\lambda_{T_e}^{\text{up}}.$$

- Model (2.7), *flux-limited* regime, weak collisionality $\nu^*_{\text{e-SOL}} \lesssim 1$

$$\frac{1}{\lambda_q^{\text{fl}}} \approx \frac{3/2}{\lambda_{T_e}^{\text{up}}} + \frac{1}{\lambda_{n_e}^{\text{up}}}.$$

The distribution of collisionality parameter $\nu^*_{\text{e-SOL}}$ in the COMPASS inter-ELM database is shown in Fig. 5.5. The data indicates that the SOL was dominated by the *flux-limited* regime $\nu^*_{\text{e-SOL}} \lesssim 1$ in the majority of the database records. A small portion of the records was bordering the area of intermediate collisionality near the peak $q_\parallel$ and in the far SOL.

Comparison of decay length models (2.6) and (2.7) with the measured downstream power decay length λ_q is shown in Fig. 5.6. There was no significant correlation between the model and the downstream data in either case. The absence of any distinct trend could be explained by the limited variability of discharge parameters and the combined uncertainty of measurements as shown in Fig. 5.1 and Fig. 5.3. However, as seen in Fig. 5.6, the magnitude of downstream decay lengths was on average 1.8× smaller than the upstream estimate in the case of λ_q^{SH} and 2.4× smaller in the case of λ_q^{fl}. The discrepancy is also emphasized by the fact that according to the analysis of the collisionality parameter, the flux-limited model λ_q^{fl} should be more accurate.

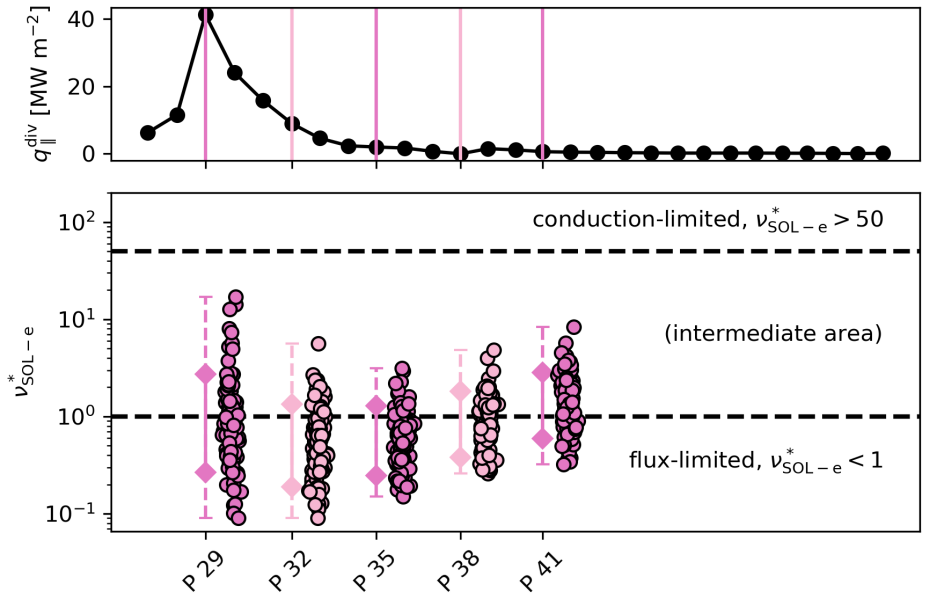

Fig. 5.5: Distribution of the electron SOL collisionality $\nu^*_{\text{e-SOL}}$, equation (2.8), in the combined datasets A+B. The upper figure presents a typical divertor $q_{\parallel}$ profile. Below is the distribution of $\nu^*_{\text{e-SOL}}$ evaluated at different points along the spatial axis of the divertor probes. Horizontal lines indicate the empirical conditions for the conduction- and flux-limited regime of SOL.

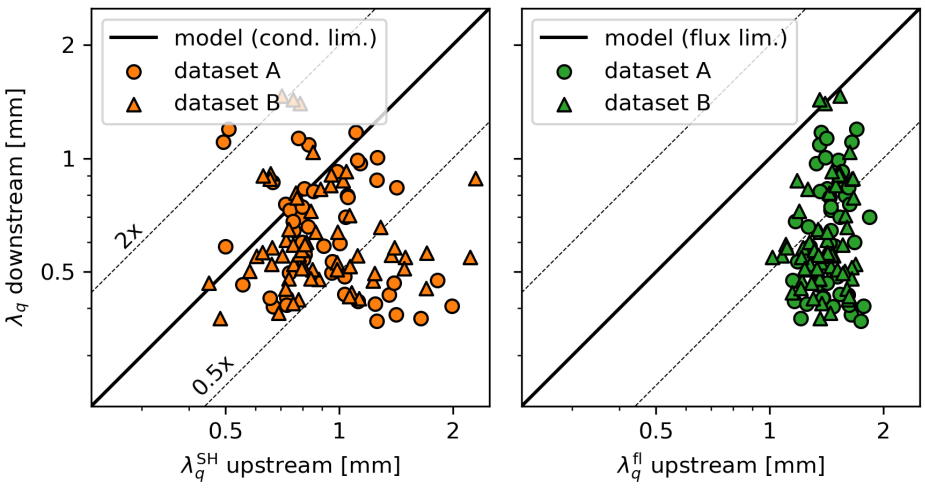

Fig. 5.6: Graph of correlation between upstream and downstream measurements. Upstream is calculated using the relations for conduction-limited (2.6) and flux-limited (2.7) SOL plasma.

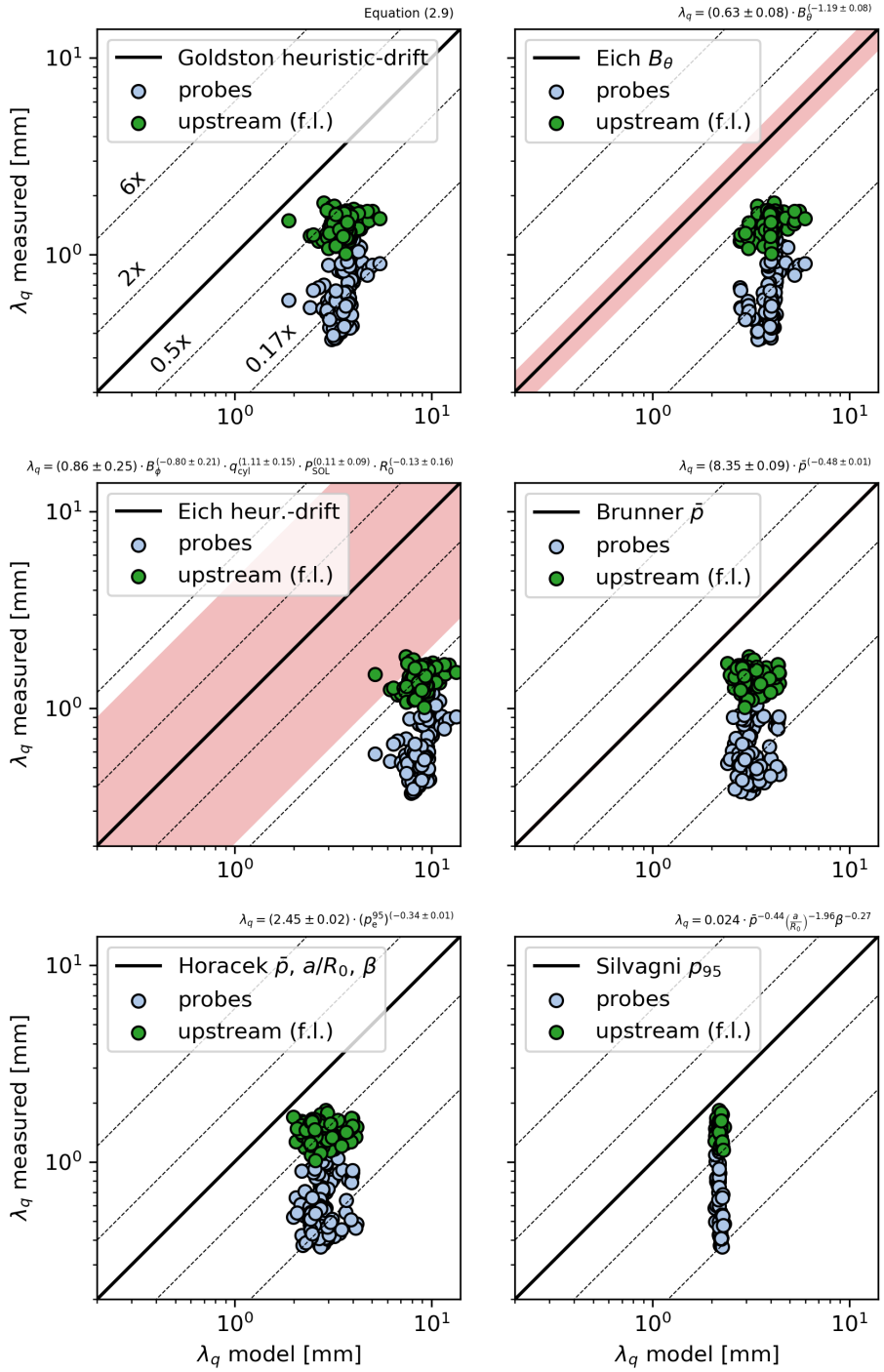

Fig. 5.7: Comparison of downstream and upstream λ_q measurements from the COMPASS tokamak with several selected scaling regressions that are listed in Tab. 5.1. Where available, the light red strip shows an estimate of the uncertainty of the regression.

Report	Parameters	Eq.
Goldston 2011 [27] (heuristic-drift)	B, I_p, P_SOL, R_0, a, κ	(2.9)
Eich 2013 [5] (see Goldston)	B_ϕ, q_cyl, P_SOL, R_0	(2.11)
Eich 2013 [5] #14	B_θ	(2.10)
Brunner 2018 [29]	$\bar{p}$	(2.22)
Horacek 2020 [31]	$\bar{p}, a/R_0, \beta$	(2.24)
Silvagni 2020 [30]	p_{95}	(2.23)

Tab. 5.1: An overview of the power decay length scaling models referenced in chapter 2. Comparison of the models with data from the COMPASS is plotted in Fig. 5.7.

5.4 Comparison with published scaling models

This section describes comparison of the published λ_q scaling models listed chapter 2 to data measured in the COMPASS tokamak. Tab. 5.1 presents an overview of the selected models and the scaling parameters across several recently published reports. There is the heuristic-drift model by Goldston2011[27] and the related empirical regression from Eich2013[5], which uses equivalent combination of parameters. Then there are also the 3 single-parameter regressions based on poloidal field B_θ, mean pressure $\bar{p}$, edge pressure p_{95} and an improved $\bar{p}$ model that includes additional parameters (aspect ratio and β). Comparison of the COMPASS data and the predictions of the models is shown in Fig. 5.7. In all cases, the measured decay length λ_q is anomalously short (factor of 2–6) in respect to the predictions. This is true for both upstream and downstream measurements, although the downstream deviates by a factor of 2–3 more than the upstream as a result of the upstream-downstream disagreement described in section 5.3. The improved $\bar{p}$ model from [31] and the p_{95} model from [30] predict values that are closest to COMPASS data, a factor of 1–2 difference in the case of upstream measurements.

5.5 Power balance

In addition to the analysis of the decay lengths, a balance of total power input and power losses was calculated in several H-mode discharges. On the COMPASS tokamak the power balance equation (1.17) takes following form

$$\frac{\mathrm{d}W_\mathrm{p}}{\mathrm{d}t} + \underbrace{P_\mathrm{rad} + P_\mathrm{div}}_{\text{losses}} = \underbrace{P_\mathrm{ohm} + P_\mathrm{nbi}}_{\text{heating}}. \tag{5.1}$$

The losses include the power P_rad radiated from the plasma volume, which was estimated by bolometers, and the power lost through cross-field transport of heat and particles P_div. The LFS component of term P_div was calculated from the LFS divertor heat flux q, which was measured by the divertor probes, using the formula (3.3).

The two components of the heating power, the right side of (5.1), are the ohmic heating P_{ohm} and the neutral beam injector (NBI) heating system P_{nbi}, which consists of two 300 kW injectors. The P_{ohm} component is always present and it can be estimated with a reasonable accuracy by measuring the plasma current and loop voltage, as opposed to estimating the effective NBI power P_{nbi} absorbed in the plasma, which often proves to be a difficult task. In this case, the following formula was used to estimate the efficiency η_{nbi} of NBI heating

$$\eta_{\mathrm{nbi}} = \eta_{\mathrm{neutr.}} \cdot \eta_{\mathrm{atten.}} \cdot \eta_{\mathrm{cx}} \approx 34\,\%, \tag{5.2}$$

where $\eta_{\mathrm{neutr.}} = 80\,\%$ is the efficiency of neutralization, $\eta_{\mathrm{atten.}} \approx 70\,\%$ describes losses due to beam attenuation and $\eta_{\mathrm{cx}} = 60\,\%$ describes losses due secondary charge exchange [46, 47]. A set of 2 H-mode discharges without NBI heating and 4 discharges with NBI heating were chosen for detailed power balance calculations.

The remaining term $\mathrm{d}W_{\mathrm{p}}/\mathrm{d}t$ is the change in confined plasma energy. Ideally, it should be negligible during the flat-top phase of a discharge. It was not omitted in the equation (3.3) in an attempt to confirm this fact and increase the accuracy of power balance estimation. The term itself was estimated from EFIT equilibrium reconstruction.

Calculation of the power balance in 6 selected discharges is shown in Fig. 5.8, Fig. 5.9 and Fig. 5.10. The balance was calculated over a time span of 10 ELM events, the graphs show time-averaged values of the terms from equation (3.3). All terms with the exception of P_{div} were approximately constant during this time window, black errobars in Fig. 5.9 and Fig. 5.10 show the standard deviation of the sum of the averages (not including P_{div}). The time evolution of the divertor term P_{div} includes power peaks correlated with the ELM events and because of that it cannot be considered constant. Nonetheless, as a first approximation, the ELM peaks were incorporated into the estimate by calculating an integral mean over the whole time window. For comparison, a mean over the quasi-constant inter-ELM time intervals (i.e. not including the ELM power peaks) was calculated as well, see Fig. 5.8, Fig. 5.9 and Fig. 5.10. To increase the precision of divertor heat flux measurements (see (3.2) and (3.3)) during the ELM events, when the heat flux is intensive, a correction of $j_{\mathrm{i}}^{\mathrm{sat}}$ measurements was applied in the following form

$$[j_{\mathrm{i}}^{\mathrm{sat}}]_{\mathrm{corr}} = \frac{j_{\mathrm{i}}^{\mathrm{sat}}}{1 - \exp\left(\frac{V_0 - V_{\mathrm{f}}}{T_{\mathrm{e}}}\right)}, \tag{5.3}$$

where $V_0 = -270\,\mathrm{V}$ is the negative bias voltage, V_{f} is the observed floating potential and T_{e} is the observed electron temperature.

The dotted area in the graphs visualizes the difference between the power input and power losses. Notice that it resides on the side of the power losses in all cases. As a rough estimate, the difference was attributed to the HFS divertor power losses $P_{\mathrm{div}}^{\mathrm{HFS}}$, since it was the only major power balance component which was not measured. However, the resulting ratio of $P_{\mathrm{div}}^{\mathrm{HFS}} : P_{\mathrm{div}}^{\mathrm{LFS}}$ proves to be quite high, more than 2 in the case of ohmic

discharges and more than 5 in the case of discharges with NBI. An expected value based on available data from IR camera is in the range 1–2, see Tab. 5.2.

Discharge	Time [ms]	$P_{\mathrm{div}}^{\mathrm{HFS}} : P_{\mathrm{div}}^{\mathrm{LFS}}$
#18455	1097.0–1135.4	1.3
#18235	1107.7–1136.2	1.9

Tab. 5.2: Ratio of divertor power losses at HFS and LFS target calculated from IR camera measurements in selected H-mode discharges. Data from the camera was not available for all discharges that were used in the power balance calculations.

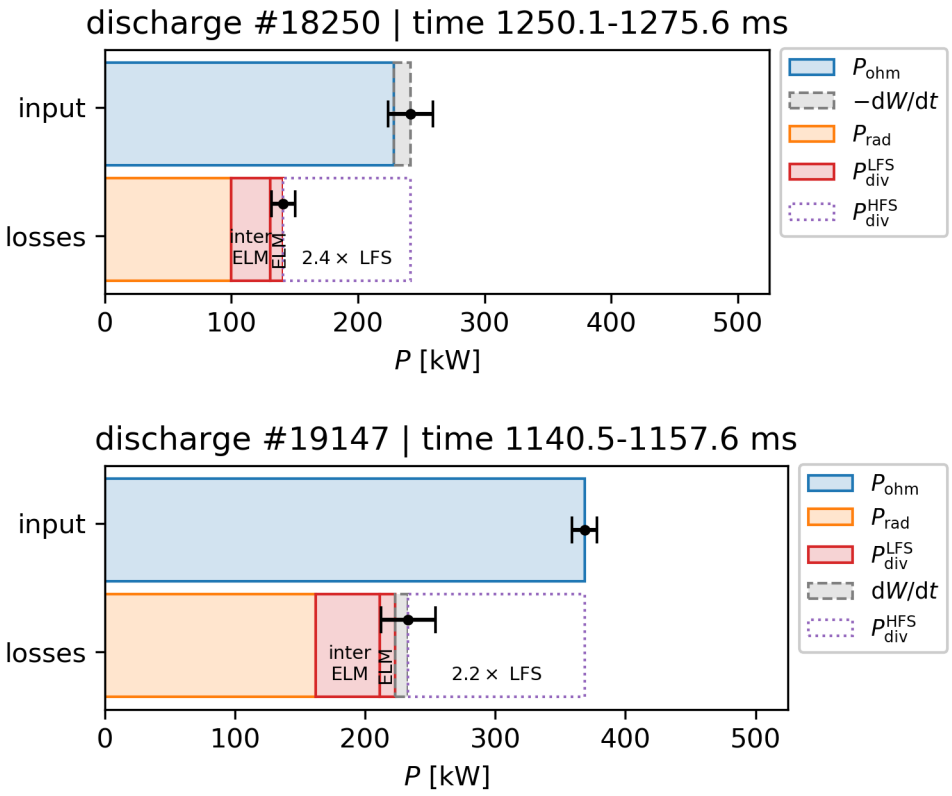

Fig. 5.8: H-mode power balance calculations in selected ohmic discharges (without NBI heating). Divertor power flux was measured only at the LFS target. Dotted rectangle marks the difference between input and losses, which should be in theory equal to the heat flux at the HFS target, see the balance equation (5.1).

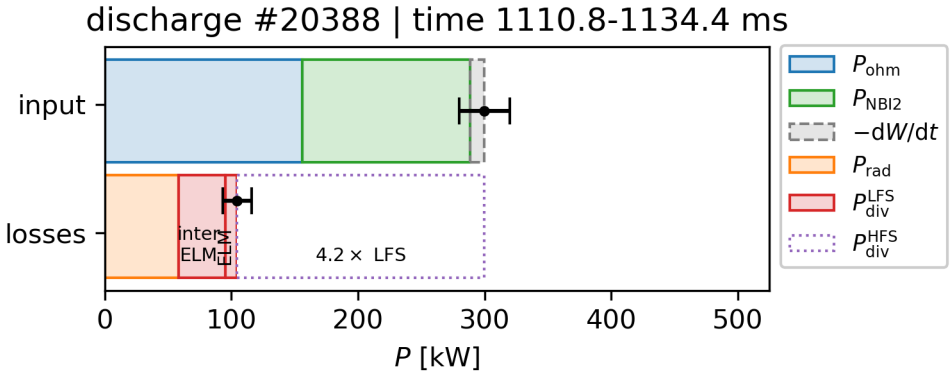

Fig. 5.9: H-mode power balance calculations in selected discharges with NBI heating. See also Fig. 5.10.

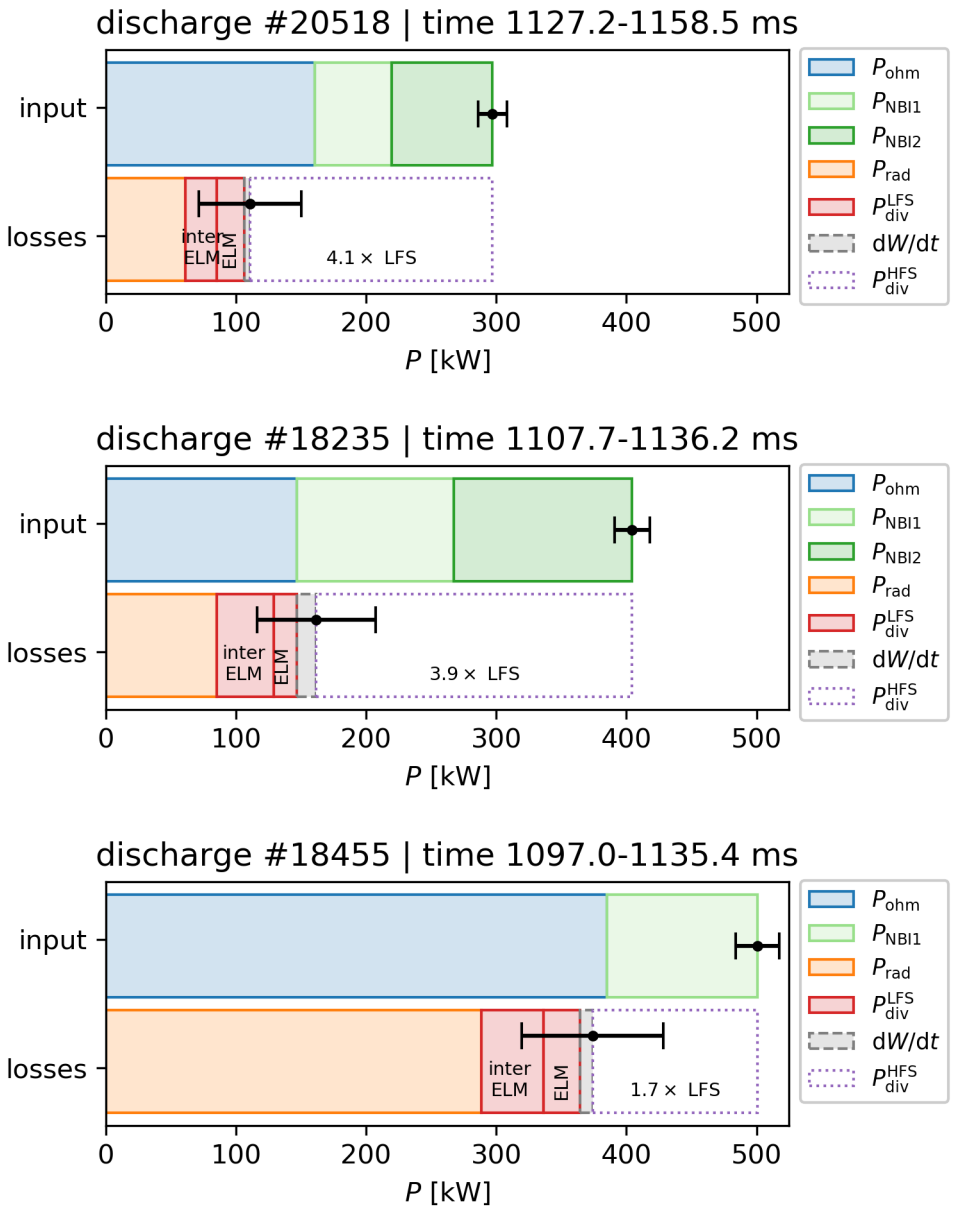

Fig. 5.10: H-mode power balance calculations in selected discharges with NBI heating. Divertor power flux was measured only at the LFS target. Dotted rectangle marks the difference between input and losses, which should be in theory equal to the heat flux at the HFS target, see the balance equation (5.1).

Chapter 6

Discussion

6.1 Quality of the power decay length measurements

The first point of the discussion is the database of inter-ELM power decay length in the COMPASS tokamak, how it was collected and how significant is the uncertainty of the λ_q measurements. The database was extracted algorithmically from multiple different experimental campaigns that were conducted over the span of several years in order to gain a reasonable number of plasma profiles. Therefore the database is expected to be afflicted by a significant statistical error both due to wide spectrum of experimental conditions and due to long-term changes in technical conditions of the machine (boronization of the first wall, adjustments in diagnostic systems, different calibrations etc.), which is a notable disadvantage of this approach. Its advantage is a larger range of plasma parameters and the objectiveness of the indiscriminate selection. The objectiveness has a potential to mitigate any systematic errors as opposed to a subjective manual selection of a few representative discharges.

The uncertainty of λ_q measurements is bound to the process of fitting the SOL profiles, which is described in the second half of chapter 4. Both in case of the upstream plasma profiles (TS diagnostics) and the downstream heat flux profile (divertor probes) the spatial resolution resulted in only 5–10 information-bearing data points per profile, which had a negative impact on the precision of measurements. It is possible to mitigate this issue by merging several profiles from consecutive inter-ELM periods, however, this approach was not available because of the rare occurrence of TS measurements during the 70–85 % period of an ELM cycle.

As a result of the level of uncertainty in λ_q in combination with a limited range of plasma parameters, the results from the COMPASS tokamak were not suitable for a single-machine regression analysis of λ_q scaling. The best application of the results was a comparison with published scaling models.

6.2 The anomaly of short power decay length

The analysis of the inter-ELM H-mode power decay lengths λ_q in the COMPASS tokamak showed that the tokamak is in a disagreement with many published scaling predictions, as discussed in section 5.4. Comparison of the results with several scaling models listed in Tab. 5.1 is plotted in Fig. 5.7. In general, the scaling predictions overestimated the decay length λ_q by a factor of 2 or more in the case of upstream measurements in the COMPASS tokamak. There was also a disagreement between upstream and downstream measurements, which is discussed separately in section 6.3.

Report	Parameters	Eq.
Eich 2013 [5] #3	B_θ	(2.10)
Eich 2013 [5] #5	B_θ, q_{95}, R_0	(2.17)
Eich 2013 [5] #9	$B_\phi, q_{95}, R_0, P_{SOL}$	(2.18)
Eich 2013 [5] #11	$B_\phi, q_{95}, R_0, P_{SOL}, f_{Gw}$	(2.19)

Tab. 6.1: Selected power decay length scaling models that were tested on the TCV tokamak, see Maurizio2021[28]. Comparison of the models with data from the COMPASS is plotted in Fig. 6.1.

A similar anomaly was observed in the TCV tokamak, report Maurizio2021[28]. As stated in section 2.2.6, TCV is comparable to COMPASS [2] in many aspects of machine and plasma parameters, although TCV has 1.6× larger major radius. Tab. 6.1 lists several λ_q regressions from Eich2013[5] that were tested against upstream measurements in TCV. Analogous comparison was performed with upstream data (flux-limited model (2.7)) from the COMPASS tokamak. Results from both tokamaks are shown in Fig. 6.1. There is an agreement between the tokamaks in models #3 and #5, where predicted λ_q noticeably overestimates the data, and also in model #11, where the predictions appears to be close to the measured values. The agreement is not perfect, since the COMPASS results systematically deviate more than the TCV results by a factor of ~ 1.6. The remaining model #9, graph c) in Fig. 6.1, correlates with the TCV data, but the COMPASS decay lengths are significantly overestimated by the prediction.

The anomaly was reported also in [44, p. 100] as a part of small analysis of inter-ELM power decay length in the COMPASS tokamak using divertor probes and IR camera. In this case, the selected scaling models overestimated the downstream measurements by a factor of 3–5.

The implications of the anomaly can be visualized in the strong single-parameter B_θ scaling that was presented in Eich2013[5]. The original graph of the dependency between λ_q and B_θ, Fig. 2.4, was extended to include data from TCV[28] and COMPASS tokamak (upstream measurements), Fig. 6.2. The extended graph shows a conflict between results from medium-sized conventional tokamaks TCV+COMPASS and spherical tokamaks[1]

[1] Spherical tokamaks represent a class of tokamak devices that are notable for their

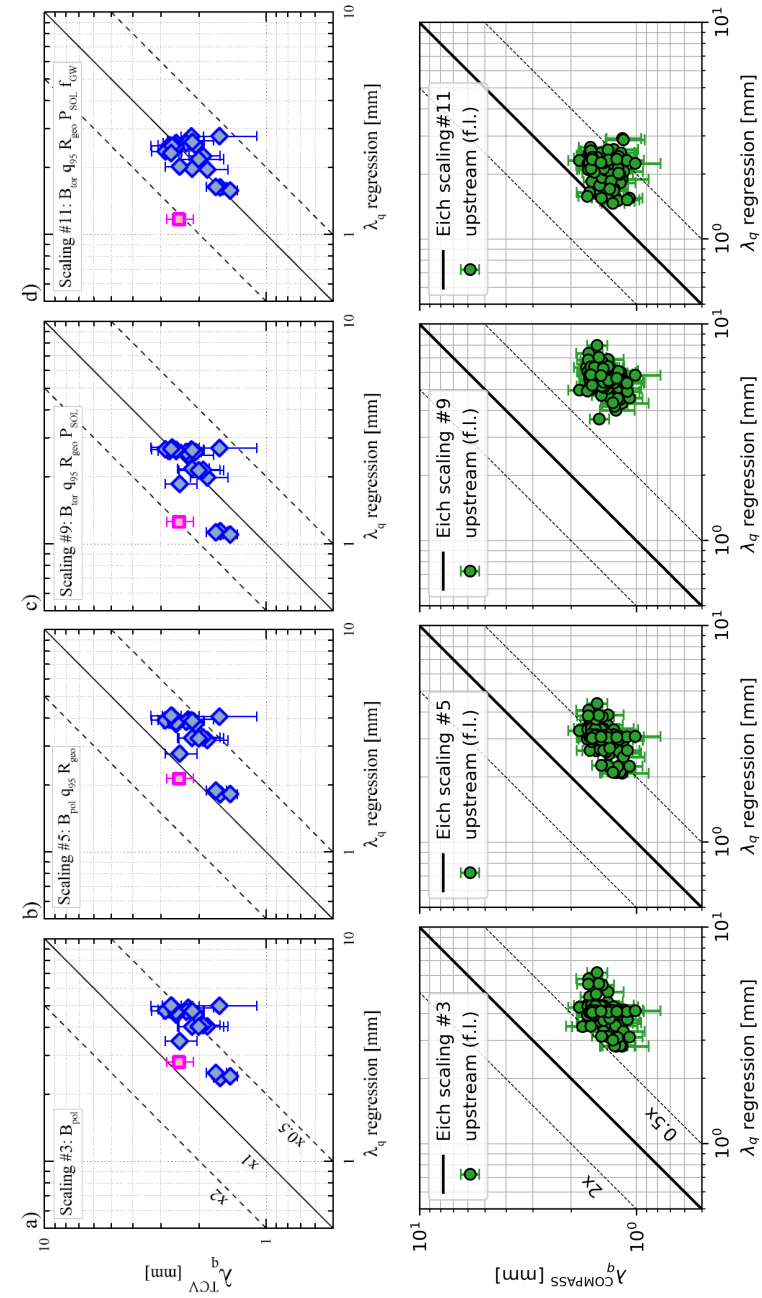

Fig. 6.1: Comparison of selected λ_q regressions published in Eich2013[5] with data from tokamak TCV[28] and tokamak COMPASS. Both tokamaks show similar deviation from the regressions with the exception of case c).

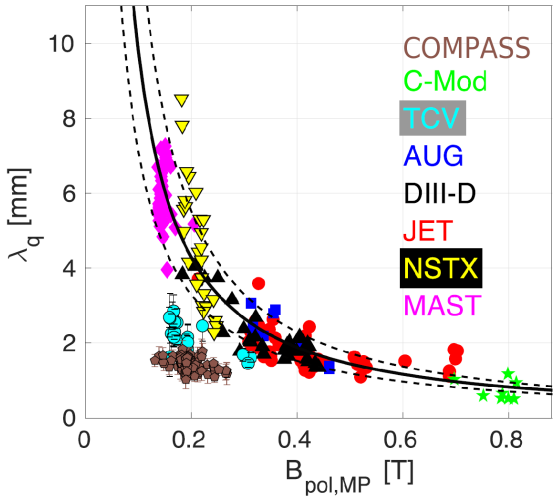

Fig. 6.2: The $B_\theta \equiv B_{\mathrm{pol,MP}}$ scaling prediction from Eich2013[5] with additional data from TCV tokamak[28] and from the COMPASS tokamak. The conventional medium-sized tokamaks TCV+COMPASS are in conflict with the spherical tokamaks NSTX+MAST.

NSTX+MAST at low $B_\theta = 0.15$–$0.25\,\mathrm{T}$. In theory, if the spherical tokamaks were not included in the regression, the resulting model would predict longer λ_q for large machines such as the ITER ($B_\theta \approx 1.2\,\mathrm{T}$). The difference in the ITER-prediction would be very small, though, when the data from Alcator C-MOD with ITER-like B_θ values are taken into account, see Fig. 2.5. Still, the anomaly offers a general observation that the current scaling models are not universally applicable and appear to break-down in the context of medium and small machines. It implies that in some aspect the machine size matters, in contrast to conclusions in Eich2013[5]. The machine size (major radius R_0, minor radius a) together with any other fixed or semi-fixed parameters present a challenge for the empirical scaling models. A sizable multi-machine database with a strong diversity of the aforementioned fixed parameters is required to observe their influence. Therefore, it is probable that the current models are missing some yet undiscovered scaling parameters, which are causing the decay length anomaly, because the influence of the parameters is amplified for example in smaller machines, in specific divertor geometries or as a result of different types (non-type-I) of ELMy H-mode regime. In summary, this observation should be taken into consideration when discussing the accuracy of any extrapolation of the current empirical scaling models.

low aspect ratio R_0/a. This is achieved by reducing the size of the central column and thereby creating an inner volume which approaches the shape of a sphere rather than a torus. The different structure of spherical tokamaks is known to have a significant impact on the parameters of both the confined plasma and the SOL region, although the exact effects are not fully explored.

6.3 Relations between upstream and downstream

Apart from the anomaly of short upstream decay lengths, which is supported by findings in the TCV tokamak [28] and discussed in previous section, a disagreement between upstream and downstream power decay length λ_q was observed in the COMPASS tokamak. As shown in (5.6), the majority of upstream data in flux-limited conditions λ_q^{fl} is systematically larger than the downstream λ_q by a factor of approximately 2. For comparison, the analysis was repeated on a small subset of L-mode discharges from Horacek2020[31] in the appendix C. Contrary to the H-mode results, the L-mode results shown in Fig. C.1 do not feature any significant systematic disagreement between upstream and downstream data.

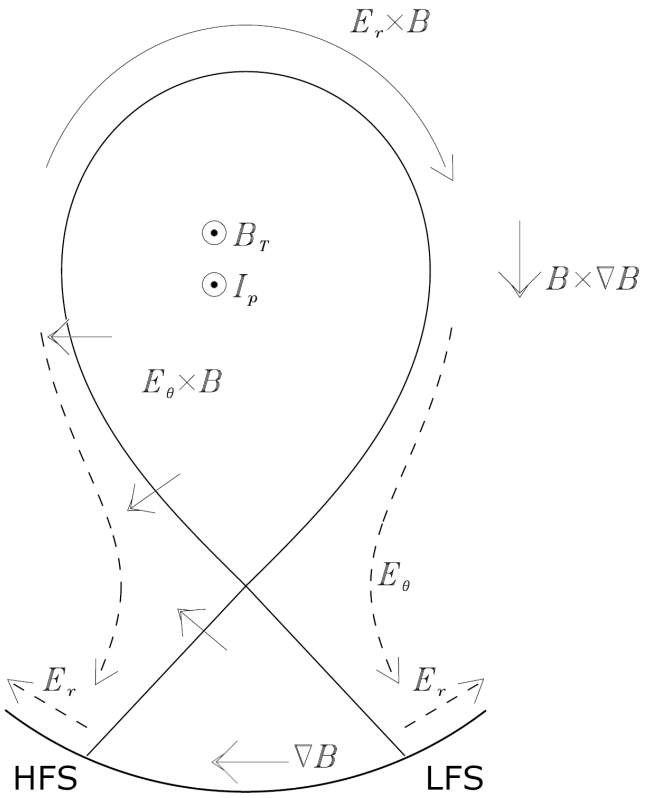

Fig. 6.3: Direction of radial and poloidal $\vec{E} \times \vec{B}$ drift and ∇B_ϕ drift ($\vec{B} \times \nabla B_\phi$) in the SOL plasma in the COMPASS tokamak. Forward direction of the toroidal magnetic field $B_\phi \equiv B_\mathrm{T}$ and plasma current I_p is assumed. [13]

The fact that this phenomenon manifests itself only in the H-mode discharges indicates that it may be connected to some properties specific to the H-mode regime. As stated before in section 1.1.3, the distinguishing property of the H-mode are the steep gradients in the edge plasma profiles. A steep gradient of radial plasma potential Φ generates a strong electrostatic field $E_r = -(\nabla\Phi)_r = -\partial\Phi/\partial r$ in the radial direction as seen in Fig. 6.4. When coupled with strong toroidal magnetic field $\vec{B}_\phi$, the fields induce an $\vec{E} \times \vec{B}$

drift in the poloidal direction. The effects of drifts on SOL heat flux profile in the COMPASS-D tokamak[2] were explored in [13, ch. 6] and the situation is illustrated in Fig. 6.3. The influence of the radial $\vec{E} \times \vec{B}$ drift and the ∇B_ϕ drift, which are also marked in Fig. 6.3 and discussed in [13], is not important in this case, because these drifts are not directly affected by the steepness of gradients in the SOL profiles.

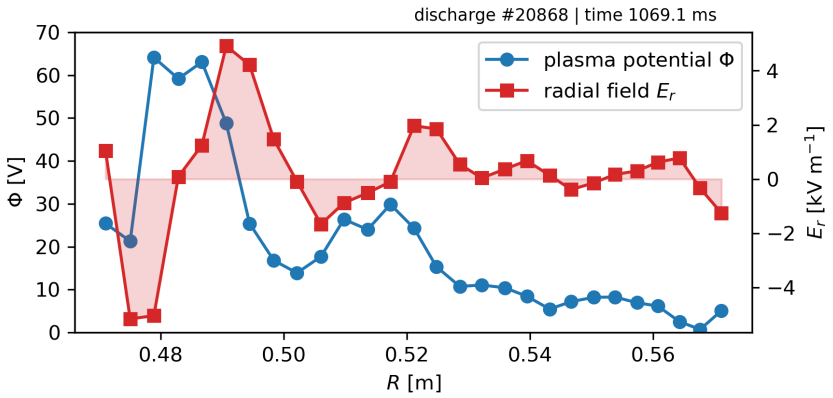

Fig. 6.4: Example of a radial profile of the plasma potential $\Phi(R)$, which was measured by the array of divertor probes, and a profile of the radial electric field $E_r = -\mathrm{d}\Phi/\mathrm{d}R$. Positive values of E_r indicate an outwards direction of the field (i.e. to the right in the graph coordinates). The derivative was estimated using the numerical method of central differences.

According to [48] the parallel heat flux due to poloidal $\vec{E} \times \vec{B}$ drift can be estimated as

$$q_{\parallel,E\times B} = 5eTnv_{E\times B}, \tag{6.1}$$

where T is the plasma temperature, n is the plasma density and the drift velocity $v_{E\times B}$ is

$$v_{E\times B} \approx \frac{E_r B_\phi}{B_\phi^2}. \tag{6.2}$$

Ratio of the drift component $q_{\parallel,E\times B}$ in comparison to the total observed downstream heat flux $q_\parallel^{\mathrm{div}}$ is plotted in Fig. 6.5 for all profiles from the databases A+B. The drift component often represents a significant fraction 10–50 % of the total observed heat flux, which indicates that the drift may be influencing the heat flux profile and the power decay length as discussed in [13]. Future experiments with reversed field configuration (i.e. $-B_\phi$) could confirm these findings. Additionally, the experimental data do not provide enough information to infer the exact process which forms the narrow downstream profile. More insight into this topic could be offered by particle simulations of the COMPASS SOL plasma during H-mode.

[2]Designation COMPASS-D refers to the COMPASS tokamak, when it was originally operated in the United Kingdom before its transfer to the Czech Republic in 2006.

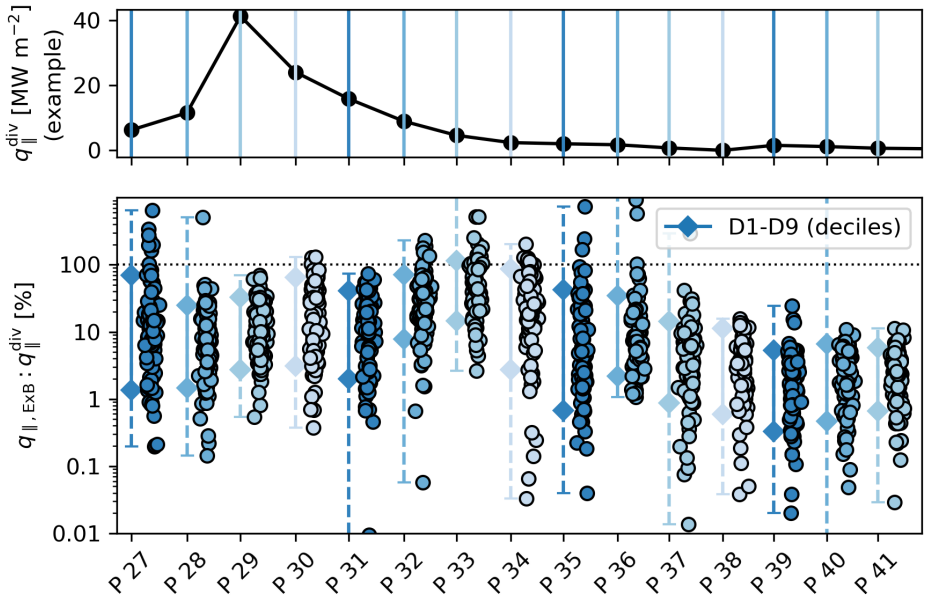

Fig. 6.5: Ratio of the observed downstream parallel heat flux $q_{\parallel}^{\mathrm{div}}$ (database A+B) and the estimated heat flux component due to poloidal $\vec{E}\times\vec{B}$ drift, equation (6.1). In some parts of the profile the drift component often represents a significant fraction of 10–50 %, indicating a possibly strong influence on the profile of $q_{\parallel}$.

6.4 Uncertainty of the power balance

Results of the H-mode power balance calculations were presented in section 5.5. The calculations included all the canonical power balance components, see equation (5.1), with the exception of HFS divertor heat flux, which was not measured. Therefore as expected, both the ohmic discharges in Fig. 5.8 and the discharges with NBI in Fig. 5.9, Fig. 5.10 show a deficiency in measured power losses. However, the magnitude of this deficiency indicates that it probably cannot be attributed solely to the HFS heat flux, because that would result in an improbably high HFS:LFS power ratio.

In an attempt to improve the accuracy, the LFS heat flux was calculated as an integral mean over 10 ELM cycles instead of using only the stationary inter-ELM phase. The contribution of the ELM power was between 20–40 % of the total LFS heat flux, which slightly lowered the HFS:LFS ratio.

The apparent HFS:LFS ratio in ohmic discharges #18250 and #19147, see Fig. 5.8, was between 2.2–2.4. A realistic ratio is typically closer to 1.0–1.5, although that is only a rough estimate and the combined standard deviation of P_{ohm}, P_{rad} and $\mathrm{d}W/\mathrm{d}t$ during the time interval (black errorbars in Fig. 5.8) need to be taken into account as well. Additionally, while the ohmic heating power P_{ohm} measurements are accurate, P_{rad} and P_{div} may be afflicted by various systematic errors.

In the case of P_{rad}, the source of small inaccuracy could be the absolute

calibration of bolometers (using radiation during discharge disruption) and the fact that they do not observe the whole plasma volume (small blind spots). Despite both of these factors, it is not probable that P_{rad} is underestimated by a significant amount, because radiative losses of more than $\sim 50\,\%$ are quite uncommon for a tokamak with carbon divertor target. For example, in the original COMPASS-D tokamak the P_{rad} measured during H-mode was equal to approximately 25 % of total input power [49]. The other term, P_{div}, is mainly affected by the sheath transmission factor γ, see equation (3.2). As stated in section 3.2, value $\gamma = 11$ was used for the divertor probes in the COMPASS tokamak, because it is approximately in agreement with both empirical and theoretical estimations. However, according to the theoretical prediction the factor γ is not perfectly constant, it varies in the radial direction along the divertor target. The value of γ is rising towards the strike point and decreasing down to $\gamma \approx 7$ in the far SOL, which could somewhat affect the resulting value of P_{div}.

The apparent HFS:LFS ratio in discharges with NBI heating, see Fig. 5.9 and Fig. 5.10, was in some cases similar to those of ohmic discharges in Fig. 5.8, however, in other cases it was factor 2–3 larger indicating a significant overestimation of absorbed NBI power. Analyses of discharges #20388 (NBI2), #20518 (NBI1,2) and #18235 (NBI1,2) resulted in ratios of 3.9–4.2, which significantly differ from the ohmic discharges. Ratios similar to the ohmic discharges were observed in discharge #18455 (NBI1), HFS:LFS = 1.7, and discharge #18234 (NBI2), which is not shown in the graphs, HFS:LFS = 2.4. Each of these two discharges featured a different NBI device, thus eliminating a possibility of a systematic fault of one specific NBI device.

The first item on the list of possible candidates for systematic errors are the calculations of the NBI efficiency, see equation (5.2). Despite a skepticism about the uncertainty of the calculations, their systematic error cannot be the cause of the occasional distinct difference in the results, namely the HFS:LFS ratio measured close to 2 vs. close to 4. Instead, these observations could be explained by arbitrary drops in the efficiency of the NBI system, during which one or both devices deliver only minimal heating power. Similar events are known to occur for example due to high neutral density in the beam duct after a pause in the machine operation, which is referred to as the *beam blocking*. In the future, the precision of the power balance analysis in tokamak COMPASS could be increased by filtering the aforementioned anomalous NBI events. Further improvement could be achieved by combining the probe measurements with the IR camera to obtain more precise divertor heat flux measurements, which was currently not possible due to the absence of the data from the camera in most of the discharges.

Conclusion

This thesis was focused on the divertor heat flux and the power balance in ELMy H-mode discharges in the COMPASS tokamak. The heat flux was measured using both the Thomson scattering (TS) diagnostics in the upstream SOL region and the divertor probe array, which consisted of Langmuir probes and Ball-pen probes, in the downstream SOL region. Both diagnostic systems were presented in chapter 3.

A database of 111 SOL profiles during the last third of the ELM cycle was selected from the existing COMPASS data. The selection criteria and the selection process, which was partially automatized, was described in the first half of the chapter 4. The second half was dedicated to the process of measuring the power decay length λ_q from the upstream plasma profiles and downstream heat flux profile mapped to outer midplane. A preliminary analysis of the measurement results, see beginning of the chapter 5, indicated an increased level of statistical variance due to the spatial resolution of the diagnostics, which was not high enough to measure the short decay lengths with high precision.

The λ_q results, shown in the chapter 5, were compared to the published scaling regressions, which were listed in chapter 2. It was not possible to test the scaling trends because of the statistical variance, as mentioned above. Nonetheless, a significant systematic anomaly was observed in the COMPASS data when compared with the models. The measured power decay lengths were shorter than the predicted values by a factor of 2–3 in the case of the upstream data. Similar anomaly was observed in the TCV tokamak [28], which is comparable in size and parameters to the COMPASS tokamak, although the agreement was not perfect as seen in Fig. 6.1. It was argued that the regression models, which were build upon data from large conventional tokamaks (JET, DIII-D, AUG, ...) and spherical tokamaks (NSTX, MAST), possibly do not include the effects of some unknown parameters, which are amplified in smaller machines. Main candidates for the unknown parameters are the 'fixed' parameters (e.g. machine size), since the influence of such parameters is hard to uncover without a thorough analysis of very diverse multi-machine database.

In addition to the previous results, a second anomaly was observed in the COMPASS tokamak — disagreement between upstream and downstream λ_q

measurements. According to a preliminary analysis from appendix C, this anomaly is specific only to the H-mode regime. A hypothesis was proposed that the SOL plasma may be affected by additional transport processes that narrow the heat flux profile as the plasma travels from upstream regions towards the divertor targets. One candidate for such process is the $\vec{E} \times \vec{B}$ drift, which, according to theoretical calculations, often represented a significant component in the divertor heat flux. Directions for future research of this anomaly were proposed, which include experiments with H-mode plasma in reversed toroidal configuration to confirm the influence of drifts and particle simulations to examine how exactly do the drifts influence the width of the heat flux profile.

Finally, the power balance analysis of several H-mode discharges was presented in the last section of chapter 5. The precision of the divertor power measurement was improved by accounting for the energy emitted during the ELM events. The set of discharges selected for analysis included 2 discharges which featured only inductive ohmic heating and 4 discharges which used the auxiliary heating via neutral beam injectors (NBI) in addition to the inductive heating. Due to the absence of data, the HFS divertor power was estimated based on the LFS divertor power. In all cases the results of the analysis showed an imbalance in the measured power input and power losses, where the input was greater than the output, although the difference was often comparable to the measurement error of the diagnostics and uncertainty of the HFS:LFS ratio. However, on some occasions a significant imbalance was observed in the NBI discharges, which was approximately equal to the expected output of one of the NBI devices. Further research would be needed to ascertain the exact nature of this discrepancy.

Bibliography

[1] J. H. E. Proll. "Trapped-particle instabilities in quasi-isodynamic stellarators". PhD thesis. Max-Planck-Institut für Plasmaphysik, 2014.

[2] *COMPASS tokamak*. `http://www.ipp.cas.cz/vedecka_struktura_ufp/tokamak/COMPASS/`. Accessed July 15, 2021.

[3] P. Vondracek et al. "Preliminary design of the COMPASS Upgrade tokamak". In: *Fusion Engineering and Design* 169 (2021), p. 112490.

[4] C. S. Chang et al. "Gyrokinetic projection of the divertor heat-flux width from present tokamaks to ITER". In: *Nuclear Fusion* 57.11 (2017), p. 116023.

[5] T. Eich et al. "Scaling of the tokamak near the scrape-off layer H-mode power width and implications for ITER". In: *Nuclear Fusion* 53.9 (2013), p. 093031.

[6] J. Wesson. *Tokamaks*. Oxford, USA: Oxford University Press, 2011.

[7] P. C. Stangeby. *The Plasma Boundary of Magnetic Fusion Devices*. Bristol, UK: Institute of physics publishing, 2000.

[8] L. Kripner and M. Tomes. *PLEQUE on github*. `https://github.com/kripnerl/pleque/`. Accessed: July 15, 2021.

[9] J. Harrison et al. "Overview of new MAST physics in anticipation of first results from MAST Upgrade". In: *Nuclear Fusion* 59.11 (2019), p. 112011.

[10] S. Coda et al. "Overview of the TCV tokamak program: scientific progress and facility upgrades". In: *Nuclear Fusion* 57.10 (2017), p. 102011.

[11] A. Creely et al. "Overview of the SPARC tokamak". In: *Journal of Plasma Physics* 86.5 (2020).

[12] F. Wagner et al. "Regime of Improved Confinement and High Beta in Neutral-Beam-Heated Divertor Discharges of the ASDEX Tokamak". In: *Phys. Rev. Lett.* 49.19 (1982), pp. 1408–1412.

[13] C. A. N. G. da Silva. "Divertor physics studies on COMPASS-D". PhD thesis. Instituto Superior Técnico of University of Lisbon, 2000.

[14] A. E. Hubbard. "Physics and scaling of the H-mode pedestal". In: *Plasma Physics and Controlled Fusion* 42.5A (2000), A15.

[15] *Pedestal — FusionWiki*. http://fusionwiki.ciemat.es/wiki/Pedestal/. Accessed July 15, 2021.

[16] J. R. Walk Jr. "Pedestal structure and stability in high-performance plasmas on Alcator C-Mod". PhD thesis. Massachusetts Institute of Technology, 2014.

[17] D. G. Whyte et al. "I-mode: An H-mode energy confinement regime with L-mode particle transport in Alcator C-Mod". In: *Nuclear Fusion* 50.10 (2010), p. 105005.

[18] M. Bernert et al. "X-point radiation, its control and an ELM suppressed radiating regime at the ASDEX Upgrade tokamak". In: *Nuclear Fusion* 61.2 (2020), p. 024001.

[19] T. Eich et al. "Inter-ELM power decay length for JET and ASDEX Upgrade: Measurement and comparison with heuristic drift-based model". In: *Physical Review Letters* 107.21 (2011), p. 215001.

[20] N. Bonanomi et al. "I-mode in non-deuterium plasmas in ASDEX Upgrade". In: *Nuclear Fusion* (2021), p. 054001.

[21] T. Happel et al. "Approaching detachment in I-mode—response of core confinement and the edge pedestal in the ASDEX Upgrade tokamak". In: *Nuclear Fusion* 61.3 (2021), p. 036026.

[22] P. C. Stangeby, J. M. Canik, and D. G. Whyte. "The relation between upstream density and temperature widths in the scrape-off layer and the power width in an attached divertor". In: *Nuclear Fusion* 50.12 (2010), p. 125003.

[23] A. Loarte et al. "Multi-machine scaling of the divertor peak heat flux and width for L-mode and H-mode discharges". In: *Journal of Nuclear Materials* 266 (1999), pp. 587–592.

[24] M. A. Makowski et al. "Analysis of a multi-machine database on divertor heat fluxes". In: *Physics of Plasmas* 19.5 (2012), p. 056122.

[25] K. Jirakova et al. "Systematic errors in tokamak magnetic equilibrium reconstruction: a study of EFIT++ at tokamak COMPASS". In: *Journal of Instrumentation* 14.11 (2019), p. C11020.

[26] M. Komm et al. "Power exhaust by core radiation at COMPASS tokamak". In: *Nuclear Fusion* 61.3 (2021), p. 036016.

[27] R. J. Goldston. "Heuristic drift-based model of the power scrape-off width in low-gas-puff H-mode tokamaks". In: *Nuclear Fusion* 52.1 (2012), p. 013009.

[28] R. Maurizio et al. "H-mode scrape-off layer power width in the TCV tokamak". In: *Nuclear Fusion* 61.2 (2021), p. 024003.

[29] D. Brunner et al. "High-resolution heat flux width measurements at reactor-level magnetic fields and observation of a unified width scaling across confinement regimes in the Alcator C-Mod tokamak". In: *Nuclear Fusion* 58.9 (2018), p. 094002.

[30] D. Silvagni et al. “Scrape-off layer (SOL) power width scaling and correlation between SOL and pedestal gradients across L, I and H-mode plasmas at ASDEX Upgrade”. In: *Plasma Physics and Controlled Fusion* 62.4 (2020), p. 045015.

[31] J. Horacek et al. “Scaling of L-mode heat flux for ITER and COMPASS-U divertors, based on five tokamaks”. In: *Nuclear Fusion* 60.6 (2020), p. 066016.

[32] S. L. Prunty. “A primer on the theory of Thomson scattering for high-temperature fusion plasmas”. In: *Physica Scripta* 89.12 (2014), p. 128001.

[33] J. Sheffield et al. *Plasma Scattering of Electromagnetic Radiation*. Burlington, USA: Academic Press, 2011.

[34] P. Bilkova et al. “High resolution Thomson scattering on the COMPASS tokamak—extending edge plasma view and increasing repetition rate”. In: *Journal of Instrumentation* 13.1 (2018), p. C01024.

[35] P. Böhm. “Temporally and spatially resolved evolution of plasma in the COMPASS tokamak”. PhD thesis. Faculty of Nuclear Sciences and Physical Engineering of CTU in Prague, 2011.

[36] M. Sos. *Optimisation of processing raw data from Thomson scattering diagnostic on the COMPASS tokamak*. Faculty of Nuclear Sciences and Physical Engineering of CTU in Prague: Master’s thesis, 2018.

[37] P. Bohm et al. “Edge Thomson scattering diagnostic on COMPASS tokamak: Installation, calibration, operation, improvements”. In: *Review of Scientific Instruments* 85.11 (2014), 11E431.

[38] J. Adamek et al. “Electron temperature and heat load measurements in the COMPASS divertor using the new system of probes”. In: *Nuclear Fusion* 57.11 (2017), p. 116017.

[39] J. Adamek et al. “Fast measurements of the electron temperature and parallel heat flux in ELMy H-mode on the COMPASS tokamak”. In: *Nuclear Fusion* 57.2 (2017), p. 022010.

[40] M. Komm et al. “Particle-in-cell simulations of plasma interaction with shaped and unshaped gaps in TEXTOR”. In: *Plasma Physics and Controlled Fusion* 53.11 (2011), p. 115004.

[41] V. Weinzettl et al. “Progress in diagnostics of the COMPASS tokamak”. In: *Journal of Instrumentation* 12.12 (2017), p. C12015.

[42] P. Vondracek et al. “Divertor infrared thermography on COMPASS”. In: *Fusion Engineering and Design* 146 (2019), pp. 1003–1006.

[43] D. Brida et al. “Role of electric currents for the SOL and divertor target heat fluxes in ASDEX Upgrade”. In: *Plasma Physics and Controlled Fusion* 62.10 (2020), p. 105014.

[44] P. Vondracek. “Plasma Heat Flux to Solid Structures in Tokamaks”. PhD thesis. Faculty of Mathematics and Physics of CU in Prague, 2019.

[45] L. Kripner et al. “Towards the integrated analysis of tokamak plasma equilibria: PLEQUE”. In: *EPS 2019: 46th European Physical Society Conference on Plasma Physics*. Vol. 43C. 2019. ISBN: 979-10-96389-11-7.

[46] K. Mitosinkova et al. “Global energy confinement time of NBI-heated plasma on the COMPASS tokamak”. In: *EPS 2017: 44th European Physical Society Conference on Plasma Physics*. Vol. 41F. 2017.

[47] J. Urban et al. “NBI system for reinstalled COMPASS-D tokamak”. In: *Czechoslovak Journal of Physics* 56.2 (2006), B176–B181.

[48] H. D. Oliveira. “A fast-moving Langmuir probe array for the divertor of the Tokamak à Configuration Variable”. PhD thesis. École polytechnique fédérale de Lausanne, 2021.

[49] S. Fielding et al. “The H-mode in COMPASS-D”. In: *Plasma Physics and Controlled Fusion* 38.8 (1996), p. 1091.

[50] I. Hughes and T. Hase. *Measurements and their uncertainties: a practical guide to modern error analysis*. OUP Oxford, 2010.

Appendix A

List of symbols

Acronyms

Alcator C-Mod	Alto Campo Toro C-Mod (tokamak in Cambridge, MA, USA)
ASDEX-U	Axially Symmetric Divertor Experiment Upgrade (tokamak in Garching, DE)
AUG	*see* ASDEX-U
BPP	ball-pen probe
CL	conduction-limited regime of SOL plasma transport
COMPASS	COMPact ASSembly (tokamak in Prague, CZ)
COMPASS-U	planned upgrade of the COMPASS tokamak
C-Mod	*see* Alcator C-Mod
DIII-D	Doublet III - D (tokamak in San Diego, CA, USA)
EFIT	equilibrium fitting algorithm
ELM	edge-localized mode
HFS	high (magnetic) field side
ITER	International Thermonuclear Experimental Reactor (tokamak in Cadarache, FR)
JET	Joint European Torus (tokamak in Culham, UK)
LCFS	last closed flux surface
LFS	low (magnetic) field side
LP	Langmuir probe
MAST	Mega Ampere Spherical Tokamak (Culham, UK)
MHD	magnetohydrodynamics

NBI	neutral beam injector
NSTX	National Spherical Torus Experiment (tokamak in Princeton, NJ, USA)
OMP	outer midplane
PFC	plasma facing component
SL	sheath-limited (flux-limited) regime of SOL plasma transport
SOL	scrape-off layer
TCV	Tokamak à Configuration Variable (Lausanne, CH)
tokamak	toroidal'naya kamera s magnitnymi katushkami [*in Russian*]
TS	Thomson scattering diagnostic system

Physical constants

e	elementary charge
k	Boltzmann constant
μ_0	vacuum permeability

Plasma coordinates

R	[m]	horizontal distance from major axis
Z	[m]	vertical distance from midplane
ϕ	[rad]	toroidal angle
R, Z, ϕ		common 3d coordinate system
R, Z		common 2d coordinate system in poloidal plane (symmetry in ϕ)
ψ	[Wb]	1d coordinate: poloidal magnetic flux
ψ_n	[–]	1d coordinate: normalized ψ coordinate
R_mp	[m]	1d coordinate: R measured at midplane ($Z = 0$)
$R_\mathrm{mp}^\mathrm{sep}$	[m]	position of separatrix in R_mp
$\bar{R}_\mathrm{mp}$	[m]	1d coordinate: $\bar{R}_\mathrm{mp} \equiv R_\mathrm{mp} - R_\mathrm{sep}$

Plasma geometry

R_0	[m]	major radius of plasma
a	[m]	minor radius of plasma
κ	[–]	plasma elongation
δ_{up}	[–]	upper plasma triangularity
V	[m^3]	confined plasma volume
S_{LCFS}	[m^2]	surface area of LCFS or separatrix

Scrape-off layer

λ_q	[mm]	power width or power decay length or heat flux decay length
λ_{T_e}	[mm]	electron temperature decay length
λ_{n_e}	[mm]	electron density decay length
q	[$\mathrm{W\,m^{-2}}$]	particle heat flux, in the context of this thesis $q \equiv q_\parallel$
$q_\parallel$	[$\mathrm{W\,m^{-2}}$]	particle heat flux parallel to magnetic field lines
$q_\perp$	[$\mathrm{W\,m^{-2}}$]	particle heat flux perpendicular to the material surface
β_{imp}	[rad]	angle between magnetic field lines and material surface, impact angle
P_{SOL}	[W]	power entering the SOL through LCFS/separatrix

Magnetic field and plasma parameters

I_p	[A]	plasma current
j_p	[$\mathrm{A\,m^{-2}}$]	plasma current density, $j_\mathrm{p} \equiv I_\mathrm{p}/\pi a^2 \kappa$
B_θ	[T]	poloidal magnetic field
B_ϕ	[T]	toroidal magnetic field
β	[–]	ratio of plasma pressure to magnetic pressure
q_{95}	[–]	safety factor at $\psi_\mathrm{n} = 0.95$
q_{cyl}	[–]	cylindrical safety factor
$L_\parallel$	[m]	connection length

T_e	[eV]	electron temperature
n_e	[m^{-3}]	electron density
$\bar{n}_\mathrm{e}$	[m^{-3}]	line averaged electron density
f_Gw		Greenwald density fraction, $f_\mathrm{Gw} \equiv (10^{-20}\bar{n}_\mathrm{e})\pi a^2/(10^{-6}I_\mathrm{p})$
p_e	[Pa]	electron pressure
p_{95}	[Pa]	electron pressure at $\psi_\mathrm{n} = 0.95$
$\bar{p}$	[Pa]	mean plasma pressure, $\bar{p} \equiv W_\mathrm{MHD}/V$
W_MHD	[J]	confined plasma energy

Appendix B

Reduced chi-squared statistic

An important tool of the experimental physics, which is frequently used in the context of indirect measurements, is the so called method of curve fitting. Let y_i be a set of observations of an arbitrary physical quantity $y = y(x)$ at points x_i and let $f = f(x; A, B, \dots)$ represent a model of y, where $A, B, \dots$ are parameters. Then the goal of this method is to find the best fit of the model $f(x; A, B, \dots)$ to the observed data points (x_i, y_i) by optimizing the values of the parameters of the model. A well known numerical method that can be used for this purpose is the least squares method.

When working with multiple sets of related observations each representing an individual curve fitting problem, it is advantageous to adopt a metric to measure the quality of the fit results. Often this is referred to as the goodness of the fit testing and a suitable metric for this task is the reduced chi-square statistic χ^2_ν. According to [50, p. 107] the statistic is defined as

$$\chi^2_\nu = \frac{\chi^2}{\nu}, \tag{B.1}$$

where $\nu = m - n$ are the degrees of freedom given by the difference between m, the number of parameters of the model, and n, the number of observations. The χ^2 depends on the observed data and the optimized fit parameters and it is calculated as follows

$$\chi^2 = \sum_{i=1}^{n} \frac{(y_i - f(x_i; A^*, B^*, \dots))^2}{\sigma_i^2}, \tag{B.2}$$

where y_i is the observation at point x_i with an estimated measurement error σ_i. The expression $f(x_i; A^*, B^*, \dots)$ represents the fit model f with the optimized parameters $A^*, B^*, \dots$ evaluated at point of the observation x_i.

To test the goodness of the fit the value of χ^2_ν is compared to value 1. The fit is deemed to be 'good' when $\chi^2_\nu \approx 1$. Large values $\chi^2_\nu \gg 1$ indicate that the model does not capture the data well in respect to the measurement error σ_i, which means that either the model is inaccurate or that the σ_i are underestimated. Small values $\chi^2_\nu \ll 1$ indicate that the errors σ_i are overestimated or that the model has too many parameters (overfitting). An illustration of all the cases and the usage of the statistic is shown in Fig. B.1.

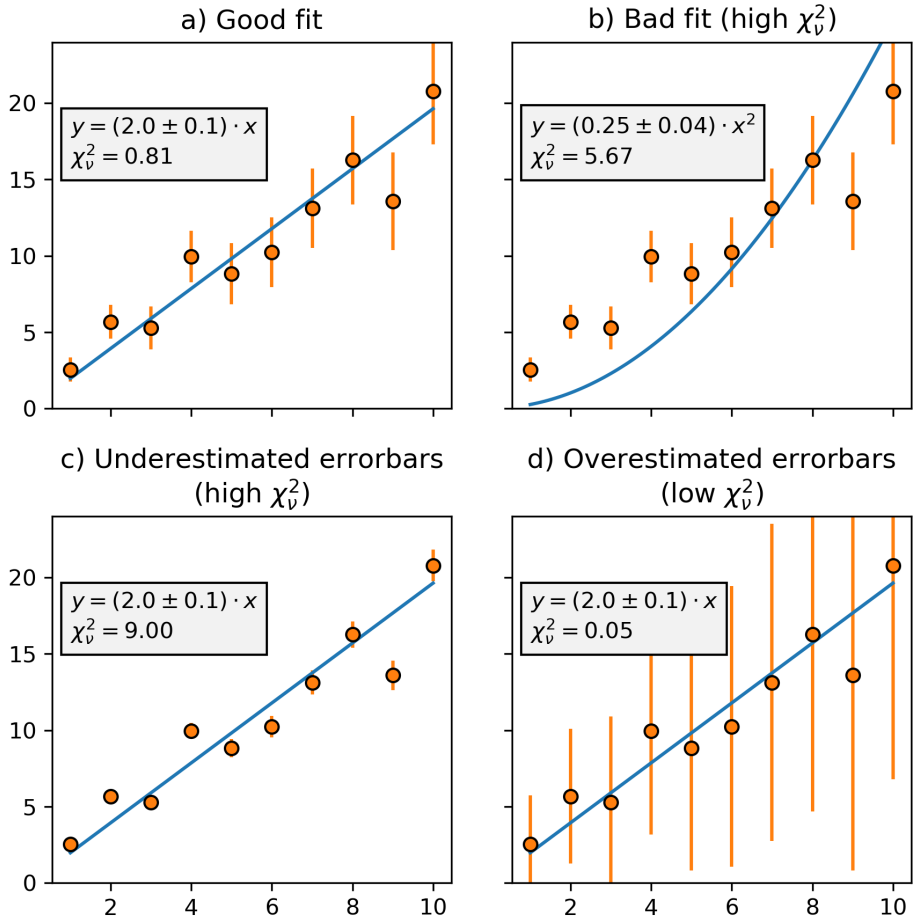

Fig. B.1: Example of testing the goodness of the fit testing using the χ^2_ν statistic. The data set was generated as $y_i = 2 \cdot x_i + \epsilon_i$, where $\epsilon_i \sim N(0, \sigma_i)$ is a random variable with normal distribution (statistical error) and σ_i represents the error estimate. Case *a)* shows a good fit, $\chi^2_\nu \approx 1$. Case *b)* shows a bad fit due to inaccurate model (quadratic function instead of linear), $\chi^2_\nu \gg 1$. Cases *c)* and *d)* use underestimated $0.3\sigma_i$ and overestimated $4\sigma_i$ errorbars, respectively, resulting in values of χ^2_ν far from 1, despite the fact that the fit produces accurate results.

Appendix C

Upstream decay length in L-mode discharges

This thesis was focused on the power decay length λ_q in H-mode discharges in the COMPASS tokamak using both upstream measurements (TS) and downstream measurements (divertor probes). A related research focused on the L-mode discharges was already published in Horacek2020[31], however, it only used data from the downstream regions.

Based on the fact that the results of this thesis shown a notable disagreement between the upstream and the downstream measurements in H-mode, see section 5.3, a similar analysis of L-mode discharges, which could offer more insight into this topic, was proposed. The analysis was conducted on a small subset of the COMPASS database from [31], which was collected from discharges in a similar time period as the dataset B. The upstream decay lengths λ_{T_e} and λ_{n_e} were measured from the TS profiles using the same methods already described in section 4.3 and the λ_q was calculated as described in 5.3. Note that in this case, no correction for stray-light noise was applied to the TS data. It was, however, possible to reduce the noise in general by averaging several TS measurements from a single discharge. The graphs of correlation between the upstream λ_q and the published downstream λ_q in L-mode are shown Fig. C.1.

According to this brief analysis, the upstream data appear correlate well with the downstream data in the L-mode discharges as opposed to the H-mode results in Fig. 5.6. The correlation appears to be slightly better in the case of the flux-limited model.

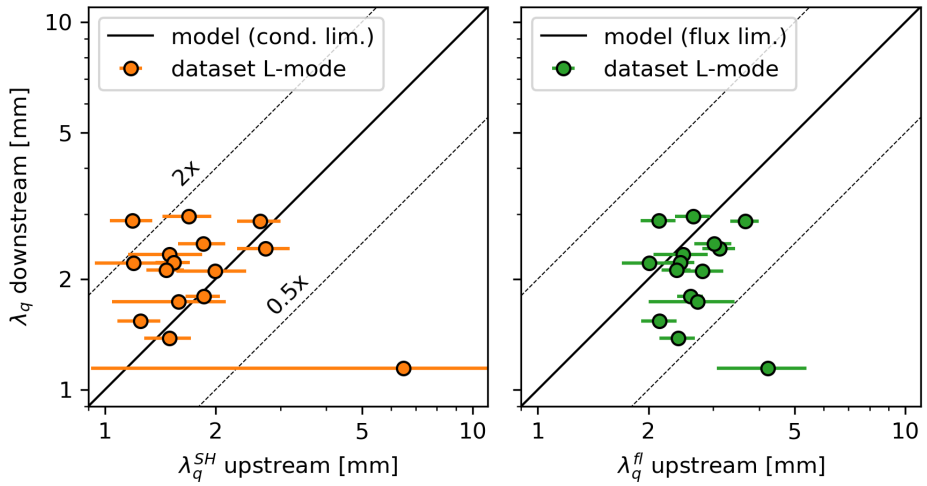

Fig. C.1: Correlation between upstream and downstream measurements in the L-mode discharges from [31]. Upstream is calculated using conduction-limited (2.6) and flux-limited (2.7) models. The H-mode results are shown in Fig. 5.6.